Nanostructure control: Nucleation and diffusion studies for predictable ultra thin film morphologies

by

Matthew Thomas Hershberger

A dissertation submitted to the graduate faculty

in partial fulfillment of the requirements for the degree of

DOCTOR OF PHILOSOPHY

Major: Condensed Matter Physics

Program of Study Committee:
Michael C. Tringides, Major Professor
Alan I. Goldman
Costas M. Soukoulis
Sanjeevi Sivasankar
Wenyu Huang

Iowa State University

Ames, Iowa

2017

Copyright © Matthew Thomas Hershberger, 2017. All rights reserved.

TABLE OF CONTENTS

LIST OF TABLES

LIST OF FIGURES

ACKNOWLEDGEMENTS

Ever since I was little I had an interest in math. Through my upper level high school science classes taught by Dennis Charbonneau and my calculus classes taught by Ray Minnich, I found that my interest in math was actually using math to understand science. I appreciate both of them for their dedication to teaching their students, myself included.

Through my undergraduate career at Bethel College in Kansas my math, physics, and computer science professors constantly challenged me and built a strong foundation of inquiry, focus, and logic. I thank Richard Remple, Christopher Earles, Lisa Thimm, Tracy Tuttle, Don Lemons, and Karl Friesen.

I must thank the National Nanotechnology Infrastructure Network along with the directors Lynn Rathbun and Melanie-Claire Mallison for the internships I had at the University of Colorado and the Forschungszentrum Jülich after my undergraduate junior and senior years. These opportunities opened my eyes to the possibilities in science and let me travel and experience different research cultures.

My graduate career at Iowa State was filled with working with excellent researchers both at Iowa State and at Ames Lab. I thank my advisor Professor Michael C. Tringides for all the mentoring, teaching, and discussions over the myriad of experiments, papers, and presentations. From my initial visit to Iowa State I knew that the research group I wanted to work in was the Tringides Group. In hindsight, I made an excellent choice, and I am grateful for both the research experiences and leadership opportunities I was afforded. I also appreciated Michael's flexibility with scheduling, especially around the holidays with visiting family. Only a handful of people will have as significant of influence on my life as Michael has, and I am grateful for the opportunity to work with him. Ames Lab scientist Dr. Myron Hupalo taught me most of what I know about scanning tunneling microscopy operation. Postdoc Dr. Hichem Hattab was key for me quickly learning how to operate spot profile analyzing low energy electron diffraction.

Professor Patricia Thiel was a frequent collaborator and a great source of encouragement. Professor Craig Ogilvie collaborated on a number of the volunteer projects I worked on with various committees through the Graduate Student Representative/Senator position and the Graduate Learning Community. I thank these people who spent time helping my professional development. I would also like to thank the other graduate students in the Tringides research group during my time at Iowa State–Steven Binz, Daniel McDougall and Shen Chen–for their help in proof reading papers, listening to presentations and discussing various scientific topics. I would like to thank Steven in particular for mentoring me at the start of my research career. Although Dante Quirinale was not in my immediate research group, we went through the condensed matter classes together and frequently bounced our latest crazy research ideas off of each other as well as other graduate school related stresses.

Finally I would like to thank my family for supporting me through my PhD. Both of my parents have supported me through all the trials in my life and encouraged me to always do my best. For my dad who set an example of integrity through his work. For my mom who was asking from the first semester if I would be able to find a job afterwards. For my younger brother Ryan who has been an inspiration for me through all of his successes and adventures.

And last thank you to my fiancée Jenny. Meeting you at Iowa State was the best thing that has ever happened to me. Thank you for not running away when you found out I was a physics PhD student. Thank you for all your patience with me while I was finishing up my dissertation.

I have been blessed abundantly.

This work was supported by the U.S. Department of Energy (DOE), Office of Science, Basic Energy Sciences, Materials Science and Engineering Division at the Ames Laboratory under contract number DE-AC02-07CH11358. The Ames Laboratory is operated for the DOE by Iowa State University. The document number assigned to this thesis/dissertation is IS-T 3204.

ABSTRACT

This thesis covers PhD research on two systems with unique and interesting physics. The first system is lead (Pb) deposited on the silicon (111) surface with the 7x7 reconstruction. Pb and Si are mutually bulk insoluble resulting in this system being an ideal case for studying metal and semiconductor interactions. Initial Pb deposition causes an amorphous wetting layer to form across to surface. Continued deposition results in Pb(111) island growth. Classic literature has classified this system as the Stranski-Krastanov growth mode although the system is not near equilibrium conditions. Our research shows a growth mode distinctly different than classical expectations and begins a discussion of reclassifying diffusion and nucleation for systems far away from the well-studied equilibrium cases.

The second system studied investigates the interactions of the Rare Earth metal Dysprosium (Dy) with a carbon based 2D lattice called graphene. Graphene is a 2D material composed of carbon atoms arranged in hexagons, similar to a honeycomb with carbon atoms at each corner. The graphene we used is grown epitaxially from a substrate of silicon carbide. This creates a multilayered playground to study how metals interact both on the surface of graphene and intercalated in between graphene layers. Many types of atoms have been studied in graphene systems, but the rare earths and in particular Dy have not been well investigated. This thesis contributes to the knowledge base of graphene on SiC structure and metal-graphene interactions.

These systems have been investigated in ultra-high vacuum (UHV) environments with base pressures around 5.0×10^{-11} torr. The Pb/Si(111)-7x7 system was investigated with scanning tunneling microscopy (STM) and the Graphene/SiC system was investigated with both STM and Spot Profile Analyzing Low Energy Electron Diffraction (SPA-LEED).

CHAPTER 1. INTRODUCTION

1.1 Motivation: nucleation and diffusion

Throughout the 20th century the pace of invention and discovery has skyrocketed. Major technologies have been developed and delivered to consumers that have changed the way they travel, communicate, and work. The underlying advances to bring these technologies to market all required enterprising electronics for their time. Current semiconductor manufacturers are set to bring chips with feature sizes of 10 nm to market in 2017 with current research and development pushing towards smaller sizes[1]. For perspective 10 nm is about 30 atoms wide, and a standard computer keyboard is around 500 million atoms long. As Richard Feynmann predicted in his *There's Plenty of Room at the Bottom* lecture, the wires for a miniaturized computer should be on the order of 10 atoms across[2]. The success in miniaturizing has been in large part due to lithography and vapor deposition processes, but we still are not at the bottom. As research pushes the technology smaller and smaller it becomes increasingly paramount that the wires are formed in the exactly correct position and the shorter linear dimensions do not decrease circuit component durability.

In order to complete these tasks, there must be an understanding of how atoms nucleate and diffuse on surfaces. Diffusion is the process of atoms moving around a surface. In the general sense, nucleation is the start of a phase change, but it is commonly used to refer to when atoms stop diffusing around a surface and form a stable cluster. The multi-discipline research field of surface science has been investigating how atoms behave on surfaces for decades, and this understanding is the cornerstone for continued technology development.

1.2 Surface science experiments

In order to study nucleation and diffusion there are a number of knobs that can be used to tune experiments and study the resulting surface morphology, and in particular the nucleated island density and size distribution. The most important of these is the type of substrate used. Numerous pure metal, semiconductor, doped semiconductor, alloy, insulating, and organic substrates have been studied throughout the years. Almost equally important is the crystal plane of the substrate that is studied. Each plane has a unique atom density, a set of preferred adsorption sites depending on the atom adsorbed, and a diffusion barrier allowing for radically different nucleation and diffusion for different crystal planes at similar conditions. In surface science experiments it is common to deposit material on the surface of the substrate to understand basic atomistic processes. The deposited material can be just as varied as the substrate, with each pair studied providing additional understanding. While there are many methods for depositing material, this thesis used molecular beam epitaxy via thermally activated evaporation physical vapor deposition. Typically simple systems of single element depositions on elemental substrates are best to study diffusion and nucleation to reduce complex interactions and confounding in the results. The Pb on Si system follows this case with mutual bulk insolubility[3]. However, the graphene on SiC system is complex with multiple interface layers requiring carefully crafted studies. In addition to types of materials, the amount deposited, the flux rate of deposition, and the temperature of the substrate during deposition all play a role in the resulting surface. Many nucleation and diffusion experiments start with tiny depositions that are less than one monolayer (ML), or the number of atoms required to cover the entire surface with a standardized packing density. Larger depositions can still provide insight into the behavior of the system, but at some point new nucleation tends to be on already deposited material, changing the experiment to homogeneous nucleation. As deposition thickness moves into the 10's of nm range the deposited film can go through a phase change[4], completely changing the scope of the experiment. The flux of adatoms joining the surface and the surface temperature also have a strong role in island nucleation. Temperature determines which energy barriers on the surface can be overcome by diffusion of adatoms. Flux and temperature interact

with each other to determine the island nucleation density. The equations governing these will be discussed further in Section 1.3. The majority of the Tringides group's experiments probe through barrier limited regimes in order to understand the typical energy scales and effects of diffusion. In the first focus system of this thesis, Pb/Si(111), classical nucleation does not hold. The investigation of the second focus, Dy on graphene/SiC, looks at nucleation on top of graphene.

The Tringides' group uses two main surface sensitive instruments to investigate the morphology of crystal surfaces. The first instrument is the Scanning Tunneling Microscope (STM). The STM produces data on the morphology of the surface by rastering a very sharp needle, or STM tip, across the surface to produce a contour map with sub Ångstrom resolution in both the x-y plane of the surface and the z-direction perpendicular to the surface. This is done by placing a voltage on the STM tip, resulting in a current flowing that is used to map the electron orbitals on the surface. The data from the STM provides a real space map of the surface, but in various operational modes can also give information about atomic species, density of states, and bonding. The second instrument is the Spot Profile Analyzing Low Energy Electron Diffraction (SPALEED). Low energy electrons have a short mean free path, so electrons diffracting from the surface create a diffraction pattern based on only the top few atomic layers of the surface. In regular Low Energy Electron Diffraction (LEED) patterns the crystal structure and lattice constants can be studied, but the resolution of the spots is typically a few percent of the reciprocal lattice. Surface defects, such as atomic steps or atom vacancies, have a regular periodic spacing on the order of tens of nm. Due to long length scales in real space becoming short in reciprocal space, surface defect periodicities appear very close to or overlap with a diffraction spot, changing its shape. The SPALEED has a coherence length of 300 nm giving it a resolution of a few tenths of a percent of the Brillouin zone, which is 10 times standard LEED. This allows the shape of individual diffraction spots, and hence long range surface features, to be probed. Further details of the operational theory of the STM, SPALEED, as well as the ultra-high vacuum systems that house the experiments are provided in Chapter 2.

There are several other surface sensitive techniques that are widely used to provide additional information about a system. While none of these techniques were used to gather the data for this thesis, journal articles that use these techniques were referenced often enough that a basic description of them is provided. The three techniques are Angle Resolved Photo Emission Specroscopy (ARPES), X-ray Photoemission Specroscopy (XPS), and Low Energy Electron Microsocpy (LEEM).

Angle Resolved Photoemission Spectroscopy (ARPES) uses x-rays to cause photoemission on the surface. By carefully measuring the angles and energy of the outgoing electrons, the band structure and fermi surface can be reconstructed. This is of particular interest in graphene research due to the linear band structure near the K point in reciprocal space. Additionally, any modifications to the linear band structure due to doping or intercalation can be investigated with ARPES.

X-ray photoemission spectroscopy (XPS) uses x-rays with an energy dispersion around 0.5 eV (depending on the source) to kick bound electrons out of atoms through the photoelectric effect, then passes the emitted electrons through a concentric hemispherical analyzer to increase the energy resolution on the way to an electron detector. The resulting data plots intensity vs. either binding energy or kinetic energy of the photoelectron (where lower binding energy corresponds with higher kinetic energy). Atoms produce well-known peaks at particular binding energies allowing XPS to identify the atoms present on the surface. X-rays have a large penetration depth, but the penetration depth of electrons is very energy dependent with the smallest penetration depth around 5 Ångstroms between 50 eV and 100 eV. By tuning the energies so the photoelectrons have kinetic energies in this range, XPS can be very surface sensitive. In addition to being able to identify which atoms are present at the surface, XPS can investigate chemical shifts of the characteristic atomic peaks, allowing information about the surrounding environment of that type of atom to be studied. Some of these initial state effects include charge density changes due to charge transfer, oxidation states, and covalent bonding.

Low Energy Electron Microscopy (LEEM) uses an electron beam to take images of the surface. There are a multitude of different operating modes–including LEED, bright field, and dark field–that allow both real space and diffraction information to be gathered about the

surface. LEEM has the advantage that it can take images of large areas of the surface ($\sim$10 μm) at a high sample rate (around 30 frames per second) while the sample is heated. Additionally, μ-LEED can be performed on individual areas 2 μm wide to study the periodicities at different parts of the sample.

Current techniques allow the surfaces of materials to be studied extensively. There are many experimental techniques that have been developed to be specifically surface sensitive with opportunities to investigate the surface morphology, surface periodicities, band structures, atomic species, and bonding. By choosing particular combinations of substrates and deposition sources and varying the deposition conditions the nucleation and diffusion on surfaces can be investigated.

1.3 Theory

Throughout the centuries the underlying driving factor in studying the physics of the universe is to mathematically describe the observed behavior with equations. When observations are verified to deviate from the known models it provides an opportunity to describe new physics. This section will cover the classical theories that describe nucleation and diffusion at surfaces.

The phenomenon of nucleation is the first step in a phase change and is a process that occurs at all length scales–from the macroscopic down to individual atoms. In the context of this thesis, atomistic nucleation on surfaces is a phase change from a dilute phase of atoms diffusing across the surface to clusters of atoms forming islands, and has its own set of developed equations that will be discussed in later paragraphs.

In the general description, the phase change is driven by the total change in free energy ΔG. The change in free energy for the formation of a condensation nucleus is governed by the difference in free energy per unit volume for the two phases ΔG_V and a surface free energy γ due to the interface between the two phases. Typically ΔG_V has a temperature dependence with a change in sign from positive to negative when the new phase becomes favorable, but the interface energy cost γ is always positive. The equation for the change in free energy of a new

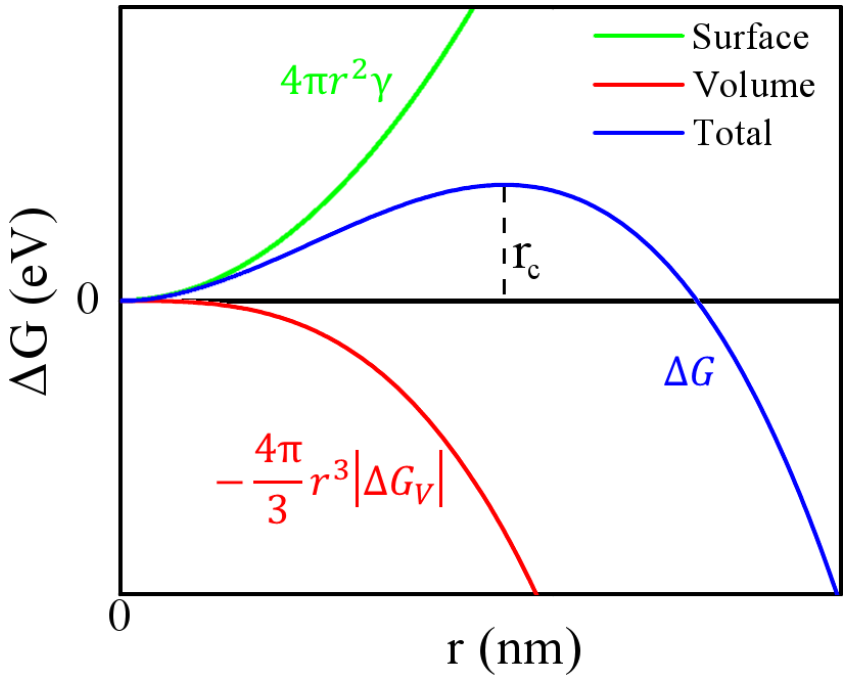

Figure 1.1 Graph of the nucleation equation for change in Gibbs free energy based on the radius of the cluster.

spherical nucleating phase cluster with radius r is diagrammed in Figure 1.1:

$$\Delta G = \frac{4}{3}\pi r^3 \Delta G_V + 4\pi r^2 \gamma \tag{1.1}$$

At temperatures where the new phase is favorable and ΔG_V is negative, there will be a radius where the slope of ΔG is 0 and ΔG has a maximum. This is the critical radius r_C, where clusters with a larger radius tend to be stable and clusters with a smaller radius tend to dissociate. The change in total free energy only determines if the reaction is thermodynamically favored, but does not determine the rate of nucleation. The growth and dissociation of clusters are stochastic processes, so while a cluster with a smaller radius usually dissociates, there is a chance that it will continue to grow to a stable radius. As the temperature changes and ΔG_V for the new phase becomes a larger negative number, the required critical radius size decreases, increasing the statistical chance that the critical radius is reached[5].

For homogeneous nucleation–nucleation where there are no impurities present during the phase change–the spherical cluster model holds and the actual phase change does not complete at the temperature where ΔG_V changes sign. Instead the system must be undercooled below

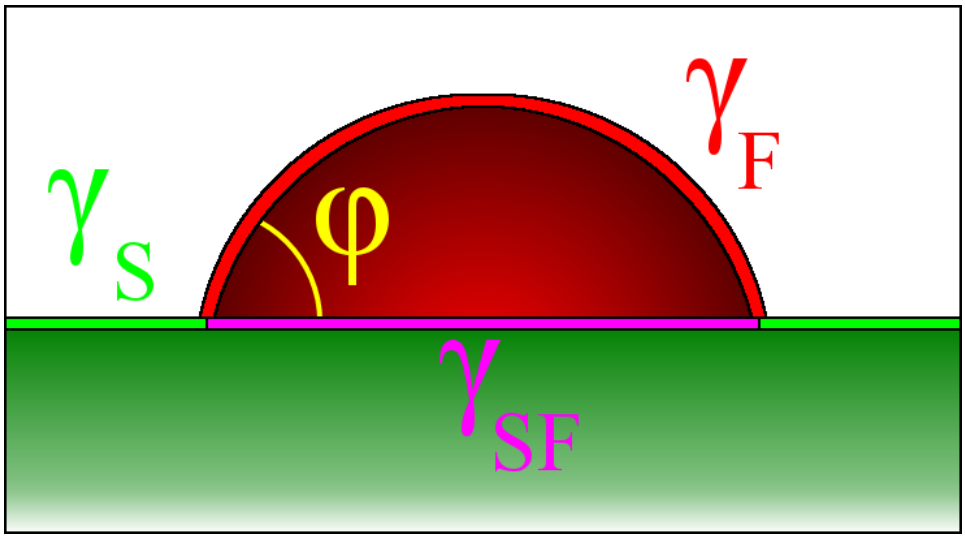

Figure 1.2 The competition between the surface energies γ of the substrate, film, and substrate-film interface determine the angle ϕ that clusters of the film grow. After Figure 14.2 of Oura[6]

the equilibrium temperature until the probability of a stable cluster developing is significant. In a heterogeneous system–foreign particles within the original phase, the wall of the container, or the substrate in a surface deposition experiment–the impurities can provide a surface for the new nucleation of a cluster. This allows the new cluster to have a radius of curvature larger than the critical radius with a greatly reduced surface area. The new cluster makes a contact angle with the impurity based on relative interface energies[5]. The general case of heterogeneous nucleation has specific consequences when applied to thin film growth on a substrate. The geometry of this model is shown in Figure 1.2. There are three possible interfaces–substrate (S), substrate-film (SF), and film (F)–each with their own surface energy γ respectively γ_S, γ_{SF}, and γ_F. An island will have the wetting angle ϕ to fulfill the force equilibrium equation:

$$\gamma_S = \gamma_{SF} + \gamma_F Cos[\phi] \tag{1.2}$$

The resulting surface morphology after a deposition falls into three main classes named after the original scientists that studied the system and are based on the relative surface energies of the interfaces. The Volmer-Weber (VW) growth mode occurs for:

$$\gamma_S < \gamma_{SF} + \gamma_F \tag{1.3}$$

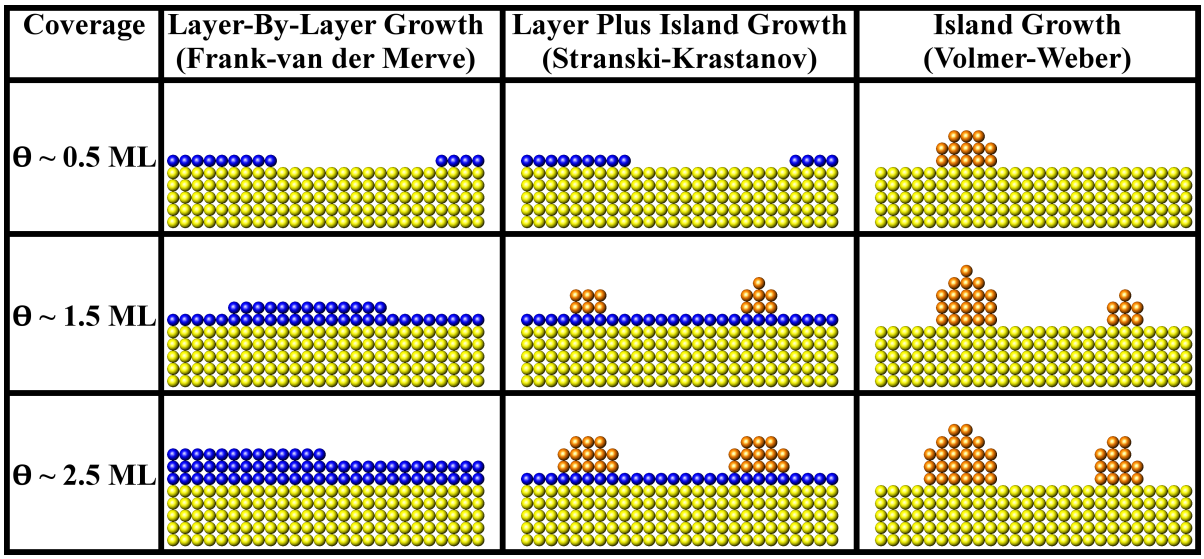

Figure 1.3 Examples of Growth Modes under equilibrium conditions. After Fig. 14.1 of Oura[6]

resulting in a unique angle ϕ for the islands to grow. Layer-by-layer growth occurs for $\phi = 0$ and:

$$\gamma_S \geq \gamma_{SF} + \gamma_F \tag{1.4}$$

There are two forms of layer-by-layer growth. When the growth mode starts by growing layer-by-layer and continues to grow layer-by-layer it is called Frank-van der Merve (FM). In some cases initial growth is layer-by-layer, but strain in the layers alters the values of γ_{SF} and γ_F until island growth is preferred instead of layer-by-layer. This growth mode is called Stranski-Krastanov (SK)[6].

Examples of the growth modes are shown in Figure 1.3. Yellow atoms are the substrate, blue atoms represent atoms growing layer by layer, and orange atoms represent atoms growing as an island. With a deposition around 0.5 ML both FM growth and SK growth are identical in overall appearance. VW growth immediately starts forming islands, with some of the islands already being multiple heights. With continued deposition to around 1.5 ML FM growth has the first layer complete and has started forming a second layer. For an SK growth system where the surface energy at the interfaces changes enough to form islands after 1 layer of growth, the 1.5 ML deposition leads to island formation on top of the first layer. VW growth has continued

island growth at 1.5 ML. Increasing to 2.5 ML shows the continued FM layer-by-layer growth. VW growth has large islands growing across the surface. The SK growth now has well developed islands resting on top of the initial layer, showing clear contrast from the other two growth modes[6].

There is a major caveat for these growth modes to hold for a system: the system must be at a temperature where thermodynamic equilibrium can be reached quicker than the experimental time scale. When a system is cooled some diffusion processes are limited and a different growth mode may be favored to form kinetically, with the thermodynamically equilibrated mode based on the surface energy values not observed during the experimental time scale. This distinction requires a different set of nucleation equations from Equation 1.1 to describe initial island formation and growth. The results of the surface experiments required to understand atomistic diffusion and nucleation have been complied in review articles[7], but a brief overview is presented here.

Deposition experiments typically start with a clean crystalline substrate that has a periodic array of minimum energy sites. Deposition adds atoms or molecules to the surface, and these species will settle into an adsorption site on the surface. Thermal fluctuations can give the species enough energy to overcome the energy barrier between the adsorption sites and hop to an adjacent site. If the energy barriers to all adjacent sites are equal, the species has an equal chance to hop to any adjacent site. This results in random walk diffusion where the direction of each hop between sites is independent of previous hops. For a single species the mean-square displacement after time t follows:

$$< \Delta r^2 >= \nu a^2 t \tag{1.5}$$

where a is the distance between adsorption sites and ν is the successful hopping rate. The successful hopping rate follows a Boltzmann distribution:

$$\nu = \nu_o e^{\frac{-\Delta E_d}{k_B T}} \tag{1.6}$$

where ν_o is the attempt frequency of the species to hop, ΔE_d is the energy barrier to diffusion to the adjacent site, T is temperature, and k_B is the Boltzmann constant[6].

Hopping along adsorption sites on a terrace are usually the lowest energy barrier. For atoms on a square lattice, the atoms on top of the terrace have a coordination number of 1. Real surfaces have common features that have typically have higher energy barriers due to changes in coordination number. Step edges, either originating from the substrate or from newly nucleated islands of the deposited atoms, are a key contributor of energy barriers that affect diffusion. When atoms approach the bottom side of step edge there is usually a larger minimum energy for the adsorption site due to the higher coordination number of 2. This presents a diffusion barrier for the atoms to hop off the step edge back to the lower terrace, hop over the step edge to the upper terrace, and to diffuse along the step edge. When atoms diffuse along a step edge they may encounter a kink site–a place along the step edge where another row has begun forming that has a coordination number of 3. As atoms approach a step edge from the upper terrace there is the Ehrlich-Schwoebel barrier that increases the energy barrier to hop down relative to terrace diffusion due to the reduction in coordination number to go over the step edge. Atoms in the middle of a step edge have a coordination number of 4, atoms in a terrace surface have a coordination number of 5, and atoms in bulk have a coordination number of 6. Each has an increasing associated energy barrier[6]. Figure 1.4(a-h) summarizes some of the common processes for atoms on surfaces.

At high temperatures atoms can easily overcome the energy barriers on the surface and the surface follows one of the classical growth modes discussed earlier in Section 1.3. At lower temperatures particular diffusion barriers are "frozen out" so the probability of an atom overcoming that particular barrier is reduced. When these types of diffusion are inactive there is a strong effect on the resulting morphology. Figure 1.5(a) shows that Gd deposited at room temperature forms islands that are not compact due to the edge diffusion barrier being partially frozen. An example of compact Gd islands after annealing at higher temperature is shown in Figure 1.5(b). Li et al.[8] show a pyramid structure with many exposed layers when the Ehrlich-Schwoebel barrier to hoping down steps is asymmetric in their Figure 2(d).

In addition to the various diffusion processes presented in Figure 1.4, the other major contribution to the resulting surface morphology is nucleation in Figure 1.4(i-k). In the surface case, nucleation is a phase change from a dilute gas of adsorbed atoms on the surface into

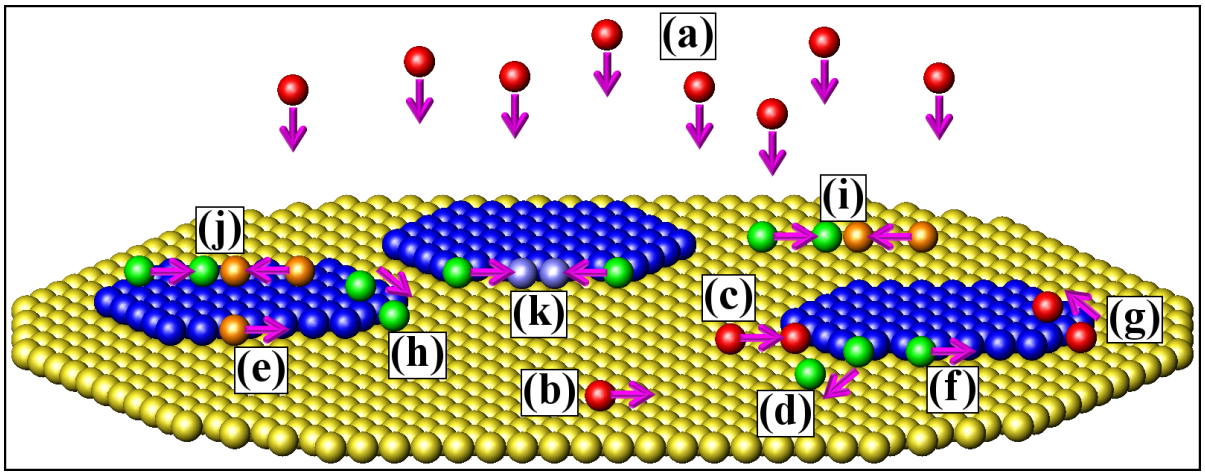

Figure 1.4 Some common diffusion and nucleation processes on a crystal surface: (a) deposition, (b) terrace diffusion, (c) attachment, (d) edge detachment, (e) kink detachment (f) edge diffusion, (g) diffusion up a step, (h) diffusion down a step (Ehrlich Schwoebel barrier), (i) nucleation on terrace, (j) nucleation on top of existing islands, (k) nucleation on a step edge forming kink sites.

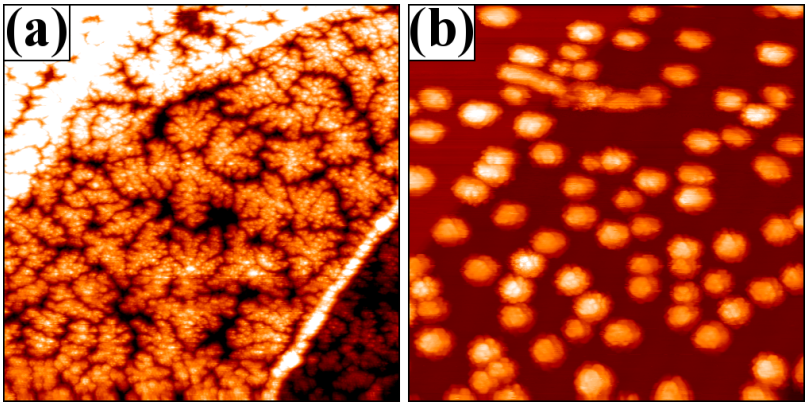

Figure 1.5 Examples of surface morphology changing based on limited diffusion. (a) STM 250 x 250 nm^2 Gd deposited on graphene/SiC(0001) at room temperature,. Limited edge diffusion causes fractal shaped islands to form. (b) STM 250 x 250 nm^2 Gd deposited on graphene/SiC(0001) at room temperature, then annealed. Typical compact shaped islands form.

clusters of atoms that form islands on the surface. Common locations for new clusters to form are in the middle of a terrace, on top of an already nucleated island, and along a step edge forming new kink sites. The nucleation equation presented earlier could be used to describe this phase change, but it is common for just two atoms that encounter each other on a terrace to form a stable cluster due to cohesive energy. For the purposes of atomistic nucleation equations it is convenient to use the quantity called the critical island size, i, which is one less than the number of atoms required to form a stable cluster for that system[6]. For example if two atoms form a stable cluster then $i = 1$, and if three atoms form a stable cluster then $i = 2$.

In addition to critical island size, there are three other variables that are key for the atomistic nucleation equations: the substrate temperature, the flux rate of the deposition, and the various surface diffusion barriers. For the purpose of sub- to few-monolayer depositions the substrate acts as an infinite heat sink, bringing all atoms deposited into thermal equilibrium with it. This temperature determines which diffusion barriers are able to be overcome with which frequencies and has a large effect on the final surface morphology. The flux rate of deposition is important during the transition between the dilute gas phase and the island clusters. This is related to the number of hops an adatom can take before another adatom joins the surface, which determines the probability of an adatom meeting another adatom versus finding an already nucleated island, and in general higher fluxes result in higher island densities. The final major component is the various diffusion barriers on the surface. For general island density calculations the terrace diffusion barrier is used, but Monte Carlo simulations will account for all of the diffusion barriers discussed earlier. The substrate temperature and the flux rate have a slight interplay in the number of hops that occur before the next adatom joins the surface, where similar island nucleation can occur for slightly lowered temperatures and slightly increased flux rates. However, when the temperature drops enough to freeze out particular diffusion mechanisms, increasing the flux rate no longer can compensate for this effect.

With this background, rate equations can be set up for the number density of adatoms n_1, the number of stable islands with number of atoms j larger than the critical island size i denoted n_x, and the number of clusters n_j of size j that are smaller than the critical island size[6].

The coefficient σ_j is the capture number, or how well islands of size j can capture diffusing adatoms. The value D is the diffusion coefficient, which is the successful hop rate Equation 1.6 times a pre-factor based on the substrate lattice. The decay rate coefficient

$$\delta_{j+1} \sim De^{\frac{-\Delta E_j^{j+1}}{k_B T}} \tag{1.7}$$

accounts for the rate of clusters losing an atom where ΔE_j^{j+1} is the energy difference between a $(j+1)$-sized cluster and a j-sized cluster. With these terms defined the rate equations are:

$$\frac{dn_1}{dt} = F - \frac{n_1}{\tau_{ads}} + \left(2\delta_2 n_2 - 2\sigma_1 D n_1^2 + \sum_{j=3}^{i} \delta_j n_j - n_1 \sum_{j=2}^{i} \delta_j D n_j\right) - n_1 \sigma_x D n_x \tag{1.8}$$

$$\frac{dn_x}{dt} = n_1 \sigma_i D n_i \tag{1.9}$$

$$\frac{dn_j}{dt} = n_1 \sigma_{j-1} D n_{j-1} - \delta_j n_j + \delta_{j+1} n_{j+1} - n_1 \sigma_j D n_j \tag{1.10}$$

Equation 1.8 describes the change in the number density of the adatoms, n_1. The flux of the deposition F adds adatoms to the surface, while the second term accounts for surface adatoms that are re-evaporated (which is negligible for low temperatures). The four terms in parenthesis are to account for adatoms that are hopping on or off of clusters. The first two terms are for clusters of size 2, while the summations cover single atoms hopping off or joining clusters of size j up to the critical island size i. The final term accounts for adatoms that join stable islands, with no decay term from stable islands by definition. Equation 1.9 describes the change in the number of stable islands with the only term describing how often adatoms join clusters with the critical island size i. Equation 1.10 covers the change in size of cluster of size j. The first two terms describe how clusters one smaller than j capture adatoms to become size j, and clusters of size j losing one adatom to become size $(j-1)$. The third and fourth terms are analogous for clusters one larger than j[6].

For a particular critical island size, flux, diffusion barrier, and temperature this set of coupled differential equations can be solved resulting in equations that vary in time, or equivalently for constant flux, the total coverage. This results four regimes of the adatom density and island nucleation. In the early transient regime the local adatom density increases until enough atoms collide for the minimum stable island size of $i+1$ atoms. This leads to islands forming very

far apart in terms of lattice constants. Each island has a depletion zone of lowered adatom density due to the local atoms forming the island, and this depletion zone expands radially outward with time. As more islands form the depletion zones begin to overlap leading to capture zones for the islands and signaling the late transient regime. When the entire surface is covered with capture zones the surface switches to the early steady state regime. While the majority of atoms that are deposited in the early steady state regime aggregate to the island whose capture zone they land in, there can still be significant new island formation especially for systems where $i = 1$ and island nucleation is irreversible[7]. The resulting trend is for the island size to scale closely with the size of the capture zone. As islands grow larger they can begin to coalesce signaling the late steady state regime.

As islands begin to have significant spatial extent in the steady state regime, the island density nucleation equation follows the form:

$$N_{isl} \sim K(\Theta) \left(\frac{F}{D}\right)^{\chi} e^{\left(\beta(i+2)^{-1} E_i\right)} \tag{1.11}$$

The flux F, diffusion coefficient D, and critical island size i are the same as discussed earlier. $K(\Theta)$ is the nucleation density. While the calculations are beyond the scope of this thesis, Venables et al.[9] gives the coefficient as a function of coverage for certain circumstances. The value of β is the standard Boltzmann value of $\frac{1}{k_B T}$. The scaling exponent χ is a function of the critical island size and can change based on the regime. Here $\chi = \frac{i}{(i+2)}$. The final term E_i is the binding energy for the optimum cluster geometry of the critical island size i. This term is zero for E_1 and non-zero for larger i. It is analogous to the volume term in the standard nucleation equation Equation 1.1.

This section has reviewed the classical theory behind nucleation and diffusion on surfaces to provide a background for what is understood about surface systems. The theory has been studied for decades and compared to experiments to flush out the details. However, the two main focuses of this thesis are for non-classical systems.

1.4 Focus 1: Pb on Si(111)-7x7 wetting layer to island transition

For decades physics students have encountered the standard particle-in-a-box problem in their quantum mechanics class. The problem is set up so the particle is allowed to be between $x = 0$ and $x = a$, then a differential equation called the Schrödinger Equation (SE) is solved with the appropriate boundary conditions. This is typically left as an exercise to understand wave functions and apply the SE in an exactly solvable setting. However, in 2000 it was observed that Pb deposited on the Si(111)-7x7 reconstructed surface tended to form islands that were 7 layers tall with a much larger frequency than expected from standard growth[10]. The origin of this preferred height is based on the quantum well energy states of the confined electrons in the z-direction compared to the fermi energy[11]. This was the first of many unusual discoveries about Pb on Si(111) over the past two decades.

The elemental silicon crystal grows in the diamond cubic lattice. Each atomic site has four nearest neighbors in a tetragonal arrangement. The surface of the crystal can be cut along any one of a number of planes. Both the Si(100) and Si(111) planes have been extensively studied in surface science experiments. When a surface is cleaved, the atoms in the top plane have a different environment compared to bulk and sometimes rearrange. If the number of atoms in the surface layer is the same as a bulk layer it is termed a conservative reconstruction. Sometimes the number of atoms in the reconstructed layers is not an integer multiple of the bulk layer. This is termed a non-conservative reconstruction. The specific name of the reconstruction uses a notation that refers to how many times larger the new unit cell is compared to the substrate. The Si(100) surface goes through a conservative reconstruction where the top layer of atoms pair up into dimers. The bulk structure is shown in Figure 1.6(a) with the reconstruction in Figure 1.6(b). The Si(111)-7x7 surface is a complicated reconstruction with five exposed layers that took over two decades to decipher[6]. A model is shown in Figure 1.6(c). The full analysis and explanation of this structure can be read in Takayanagi et al.[12]. The specific sample preparation for our Si(111)-7x7 samples is discussed further in Chapter 2.2.

One additional reconstruction for the Si(111) surface is the α–$\sqrt{3}$ x $\sqrt{3}$ Pb/Si(111) phase. This phase requires Pb to first be deposited on top of Si(111), and then heat the system resulting

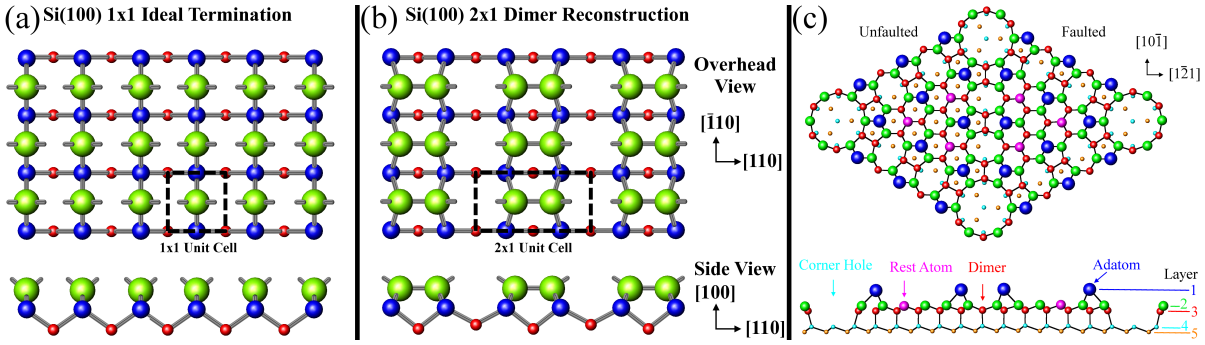

Figure 1.6 Examples of reconstructions of the Si system. (a) Si(100)-1x1 bulk atom placement, after Figure 8.12 of Oura[6], (b) Si(100)-2x1 with reconstruction, after Figure 8.12 of Oura[6], (c) Si(111)-7x7 reconstruction after Figure 8.18 of Oura[6]

in a complicated phase diagram at low temperatures[13]. This sister system to Pb/Si(111)-7x7 was found to have a set of devil's staircase linear phases[14]. Two generating phases of $\sqrt{7}$ x $\sqrt{3}$ at 1.20 ML Pb and $\sqrt{3}$ x $\sqrt{3}$ at 1.33 ML Pb can be combined in linear combinations to realize an infinite number of phases between 1.20 ML and 1.33 ML with a particular phase corresponding to a very specific local coverage. The most surprising feature of these linear phases was the addition of Pb could cause the entire surface to reconfigure with 100% accuracy in a matter of minutes[13]. Experiments depositing C_{60} molecules on the $\sqrt{7}$ x $\sqrt{3}$ surface at 210 K showed a perfect localized reordering could occur in under 100 seconds, the time required to conduct an STM scan[15]. Further investigations of both the $\sqrt{3}$ x $\sqrt{3}$ phase and Pb deposited on the Si(111)-7x7 phase using LEEM showed the wetting layer could transport mass at a linear rate with a non-dispersing diffusion front instead of the expected $x \sim \sqrt{t}$ at temperatures well below the melting point of Pb[16][17]. This non-classical diffusion allowed islands to exchange mass and promoted ring growth on islands that had not yet reached the preferred 7 layer height[18]. Leading theory explanations point to the density of the wetting layer rising above the density of the Pb(111) crystal plane being critical in this mass transport[19]. The higher density was measured in different experiments with a range of techniques including STM, SPALEED, X-ray, and LEEM. This unexpected high density of a Pb wetting layer is possible since x-ray reflectivity measurements found that the liquid Pb close to the Si(111) surface was in a compressed state with a density 30% percent higher than the bulk close-packed solid Pb

density, likely due to charge transfer[20]. At this point both the wetting layer behavior and the island behavior had been studied, but the transition between the two regimes had been untouched. The focus for the 1st part of this thesis is investigating this transition.

1.5 Focus 2: metals and the Gr/SiC system

The Rare Earth metals have a long history of being studied at Iowa State University and Ames Lab. Among the Rare Earth metals the chemical reactivity is similar, while the magnetic properties can greatly vary due to the $4f$ electron orbitals being filled with increasing atomic number. This allows a lever to substitute different magnetic moments into compounds and has resulted in studies of how long range magnetic ordering affects magnetic phases including superconductors[21]. Dy has one of largest effective magneton numbers among all of the elements, making it of particular interest for magnetic systems[22]. Although the magnetic properties of the Dy in the studies discussed here will likely lead to some new and interesting physics, this thesis focuses on the diffusion and nucleation of Dy in forming these structures and particular magnetic investigations are beyond the scope of this thesis.

In continuing the Ames Lab tradition of studying Rare Earth metals, the Tringides group has been investigating the interactions of several Rare Earth metals with the recently isolated carbon structure graphene. Graphene is a 2D sheet of carbon atoms arranged at the corners of a honeycomb lattice. Initially, graphene research was focused on the unique properties of the 2D sheet and its linear band structure[23][24]. Various preparation methods were developed, including mechanical exfoliation[25], epitaxial growth on a silicon carbide substrate[26], and preparation of graphene by chemical vapor deposition on Ni[27] as well as other substrates. The structure and preparation of graphene/SiC for our samples is covered in Chapter 2.2, with a study of the structure of the graphene/buffer/SiC system using diffraction covered in Chapter 6.

Following the initial studies of pure graphene, various metals were deposited and studied on top of graphene with a wide range of results. At room temperature Gd formed fractal-like islands[28] while Dy formed compact blob-like islands with multiple layers exposed[29]. For Dy deposited at 660 K compact islands grew with a face-centered cubic (FCC) structure instead of the bulk hexagonal close-packed (HCP) structure[30]. Fe islands had an island density that

grew linearly with coverage due to long range repulsive effects[31], while Eu islands spread over the surface as 2 layer islands in an almost layer-by-layer growth[28]. Usually metals grew 3D on graphene partially due to the ratio of the adsorption energy to the cohesive energy[28], however it was shown that Dy could grow as an amorphous ∼2 layer thick film when it was kinetically limited[32].

The current stage of research with graphene is attempting to intercalate atomic species either between layers of graphene in the hope to replicate bulk graphitic compounds[33–35], or between the graphene and substrate (for example: Au[36], Cu[37], H[38], F[39], Li[40], Sn[41] among many others). There are open questions about the locations of atoms in the graphene on SiC system due to a carbon rich buffer layer that will be reviewed further in Chapter 6 so future experiments intercalating metals under graphene can be properly interpreted.

1.6 Chapter previews

Chapter 2 provides more information about the theory, operation, and data produced by scanning tunneling microscopy and spot profile analyzing low energy electron diffraction along with equipment and processing associated with ultra-high vacuum systems. This thesis is split into studies of nucleation and diffusion for two main systems: Pb/Si(111)-7x7 and metals on graphene/SiC(0001). Chapters 3 through 5 investigate the previously unstudied transition from wetting layer growth to island growth for Pb/Si(111)-7x7 at temperatures around 200 K. The Pb on Si(111) system is well known for non-classical effects, but the wetting layer to island transition has been surprising. Chapter 3 was published in *Physical Review Letters* in 2014[42] and covers the initial island formation and growth after continued depositions. Chapter 4 compares island size scaling to classical models, takes a look at the changing wetting layer structure, and notes highly uni-directional island growth. Chapter 5 reveals multiple generations of island growth with continued deposition and discusses how the wetting layer could mediate the continued growth. Chapters 6 and 7 study the graphene on SiC(0001) system. Chapter 6 contributes to the understanding of the still debated graphene/SiC structure by investigating how the diffraction pattern changes with annealing, and discussing an unusual electronic feature seen in all electron diffraction studies of graphene on all substrates. Chapter

7 was published in *Journal of Physics: Condensed Matter*[30], and investigates dysprosium deposited on top of graphene/SiC(0001). The results show the crystal structure of the nucleated islands is FCC instead of the expected bulk HCP.

References

[1] R. Courtland, *Intel finds moores laws next step at 10 nanometers* (2016), URL http://spectrum.ieee.org/semiconductors/devices/intel-finds-moores-laws-next-step-at-10-nanometers. 1.1

[2] R. P. Feynman, Journal of Microelectromechanical Systems **1**, 60 (1992), ISSN 1057-7157. 1.1

[3] E. Ganz, F. Xiong, I.-S. Hwang, and J. Golovchenko, Phys. Rev. B **43**, 7316 (1991), URL http://link.aps.org/doi/10.1103/PhysRevB.43.7316. 1.2

[4] V. Kaul, B. Bist, and O. Srivastava, Thin Solid Films **30**, 65 (1975), ISSN 0040-6090, URL http://www.sciencedirect.com/science/article/pii/0040609075903053. 1.2

[5] D. R. Askeland and P. P. P., *The science and engineering of materials* (Brooks/Cole-Thomson Learning, 2003), 4th ed. 1.3

[6] K. Oura, *Surf. Sci.: an introduction*, Advanced texts in physics (Springer, 2003), ISBN 9783540005452, URL http://books.google.com/books?id=HBFtQgAACAAJ. 1.2, 1.3, 1.3, 1.3, 1.3, 1.3, 1.3, 1.4, 1.6

[7] J. Evans, P. Thiel, and M. Bartelt, Surface Science Reports **61**, 1 (2006), ISSN 0167-5729, URL http://www.sciencedirect.com/science/article/pii/S0167572906000021. 1.3, 1.3

[8] M. Li, P.-W. Chung, E. Cox, C. J. Jenks, P. A. Thiel, and J. W. Evans, Phys. Rev. B **77**, 033402 (2008), URL http://link.aps.org/doi/10.1103/PhysRevB.77.033402. 1.3

[9] J. A. Venables, G. D. T. Spiller, and M. Hanbucken, Reports on Progress in Physics **47**, 399 (1984), URL http://stacks.iop.org/0034-4885/47/i=4/a=002. 1.3

[10] K. Budde, E. Abram, V. Yeh, and M. C. Tringides, Phys. Rev. B **61**, R10602 (2000), URL http://link.aps.org/doi/10.1103/PhysRevB.61.R10602. 1.4

[11] C. M. Wei and M. Y. Chou, Phys. Rev. B **66**, 233408 (2002), URL http://link.aps.org/doi/10.1103/PhysRevB.66.233408. 1.4

[12] K. Takayanagi, Y. Tanishiro, S. Takahashi, and M. Takahashi, Surface Science **164**, 367 (1985), ISSN 0039-6028, URL http://www.sciencedirect.com/science/article/pii/0039602885907538. 1.4

[13] S. Stepanovsky, M. Yakes, V. Yeh, M. Hupalo, and M. Tringides, Surface Science **600**, 1417 (2006), ISSN 0039-6028, URL http://www.sciencedirect.com/science/article/pii/S003960280501383X. 1.4

[14] M. Hupalo, J. Schmalian, and M. C. Tringides, Phys. Rev. Lett. **90**, 216106 (2003), URL http://link.aps.org/doi/10.1103/PhysRevLett.90.216106. 1.4

[15] A. V. Matetskiy, L. V. Bondarenko, D. V. Gruznev, A. V. Zotov, A. A. Saranin, and M. C. Tringides, Journal of Physics: Condensed Matter **25**, 395006 (2013), URL http://stacks.iop.org/0953-8984/25/i=39/a=395006. 1.4

[16] K. L. Man, M. C. Tringides, M. M. T. Loy, and M. S. Altman, Phys. Rev. Lett. **101**, 226102 (2008), URL http://link.aps.org/doi/10.1103/PhysRevLett.101.226102. 1.4

[17] K. L. Man, M. C. Tringides, M. M. T. Loy, and M. S. Altman, Phys. Rev. Lett. **110**, 036104 (2013), URL http://link.aps.org/doi/10.1103/PhysRevLett.110.036104. 1.4

[18] M. Hupalo and M. C. Tringides, Phys. Rev. B **75**, 235443 (2007), URL http://link.aps.org/doi/10.1103/PhysRevB.75.235443. 1.4

[19] L. Huang, C. Z. Wang, M. Z. Li, and K. M. Ho, Phys. Rev. Lett. **108**, 026101 (2012), URL http://link.aps.org/doi/10.1103/PhysRevLett.108.026101. 1.4

[20] H. Reichert, M. Denk, J. Okasinski, V. Honkimäki, and H. Dosch, Phys. Rev. Lett. **98**, 116101 (2007), URL http://link.aps.org/doi/10.1103/PhysRevLett.98.116101. 1.4

[21] Z.-A. Ren, G.-C. Che, X.-L. Dong, J. Yang, W. Lu, W. Yi, X.-L. Shen, Z.-C. Li, L.-L. Sun, F. Zhou, et al., EPL (Europhysics Letters) **83**, 17002 (2008), URL http://stacks.iop.org/0295-5075/83/i=1/a=17002. 1.5

[22] N. W. Ashcroft and N. D. Mermin, *Solid State Physics* (Sanders College Publishing, 1976), ISBN 9780030839931. 1.5

[23] K. S. Novoselov, A. K. Geim, S. Morozov, D. Jiang, M. Katsnelson, I. Grigorieva, S. Dubonos, and A. Firsov, Nature **438**, 197 (2005), URL http://www.nature.com/nature/journal/v438/n7065/abs/nature04233.html. 1.5

[24] T. Ohta, A. Bostwick, T. Seyller, K. Horn, and E. Rotenberg, Science **313**, 951 (2006), ISSN 0036-8075, URL http://science.sciencemag.org/content/313/5789/951. 1.5

[25] K. S. Novoselov, A. K. Geim, S. V. Morozov, D. Jiang, Y. Zhang, S. V. Dubonos, I. V. Grigorieva, and A. A. Firsov, Science **306**, 666 (2004), ISSN 0036-8075, URL http://science.sciencemag.org/content/306/5696/666. 1.5

[26] C. Berger, Z. Song, T. Li, X. Li, A. Y. Ogbazghi, R. Feng, Z. Dai, A. N. Marchenkov, E. H. Conrad, P. N. First, et al., The Journal of Physical Chemistry B **108**, 19912 (2004), URL http://dx.doi.org/10.1021/jp040650f. 1.5

[27] K. S. Kim, Y. Zhao, H. Jang, S. Y. Lee, J. M. Kim, K. S. Kim, J.-H. Ahn, P. Kim, J.-Y. Choi, and B. H. Hong, Nature **457**, 706 (2009), URL http://www.nature.com/nature/journal/v457/n7230/abs/nature07719.html. 1.5

[28] X. Liu, C.-Z. Wang, M. Hupalo, H.-Q. Lin, K.-M. Ho, and M. C. Tringides, Crystals **3**, 79 (2013), URL http://www.mdpi.com/2073-4352/3/1/79/htm. 1.5

[29] M. Hupalo, X. Liu, C.-Z. Wang, W.-C. Lu, Y.-X. Yao, K.-M. Ho, and M. C. Tringides, Advanced Materials **23**, 2082 (2011), URL http://onlinelibrary.wiley.com/doi/10.1002/adma.201100412/full. 1.5

[30] M. T. Hershberger, M. Hupalo, P. A. Thiel, and M. C. Tringides, Journal of Physics: Condensed Matter **25**, 225005 (2013), URL http://stacks.iop.org/0953-8984/25/i=22/a=225005. 1.5, 1.6

[31] S. M. Binz, M. Hupalo, X. Liu, C. Z. Wang, W.-C. Lu, P. A. Thiel, K. M. Ho, E. H. Conrad, and M. C. Tringides, Phys. Rev. Lett. **109**, 026103 (2012), URL http://link.aps.org/doi/10.1103/PhysRevLett.109.026103. 1.5

[32] D. McDougall, H. Hattab, M. Hershberger, M. Hupalo, M. H. von Hoegen, P. Thiel, and M. Tringides, Carbon **108**, 283 (2016), ISSN 0008-6223, URL http://www.sciencedirect.com/science/article/pii/S0008622316305383. 1.5

[33] K. Kanetani, K. Sugawara, T. Sato, R. Shimizu, K. Iwaya, T. Hitosugi, and T. Takahashi, Proceedings of the National Academy of Sciences **109**, 19610 (2012), URL http://www.pnas.org/content/109/48/19610.short. 1.5

[34] J. Kleeman, K. Sugawara, T. Sato, and T. Takahashi, Phys. Rev. B **87**, 195401 (2013), URL http://link.aps.org/doi/10.1103/PhysRevB.87.195401.

[35] S. Ichinokura, K. Sugawara, A. Takayama, T. Takahashi, and S. Hasegawa, ACS Nano **10**, 2761 (2016), URL http://dx.doi.org/10.1021/acsnano.5b07848. 1.5

[36] I. Gierz, T. Suzuki, R. T. Weitz, D. S. Lee, B. Krauss, C. Riedl, U. Starke, H. Höchst, J. H. Smet, C. R. Ast, et al., Phys. Rev. B **81**, 235408 (2010), URL http://link.aps.org/doi/10.1103/PhysRevB.81.235408. 1.5

[37] K. Yagyu, T. Tajiri, A. Kohno, K. Takahashi, H. Tochihara, H. Tomokage, and T. Suzuki, Applied Physics Letters **104**, 053115 (2014), URL http://dx.doi.org/10.1063/1.4864155. 1.5

[38] C. Riedl, C. Coletti, T. Iwasaki, A. A. Zakharov, and U. Starke, Phys. Rev. Lett. **103**, 246804 (2009), URL http://link.aps.org/doi/10.1103/PhysRevLett.103.246804. 1.5

[39] A. L. Walter, K.-J. Jeon, A. Bostwick, F. Speck, M. Ostler, T. Seyller, L. Moreschini, Y. S. Kim, Y. J. Chang, K. Horn, et al., Applied Physics Letters **98**, 184102 (2011), URL http://dx.doi.org/10.1063/1.3586256. 1.5

[40] C. Virojanadara, S. Watcharinyanon, A. A. Zakharov, and L. I. Johansson, Phys. Rev. B **82**, 205402 (2010), URL http://link.aps.org/doi/10.1103/PhysRevB.82.205402. 1.5

[41] H. Kim, O. Dugerjav, A. Lkhagvasuren, and J. M. Seo, Journal of Physics D: Applied Physics **49**, 135307 (2016), URL http://stacks.iop.org/0022-3727/49/i=13/a=135307. 1.5

[42] M. T. Hershberger, M. Hupalo, P. A. Thiel, C. Z. Wang, K. M. Ho, and M. C. Tringides, Phys. Rev. Lett. **113**, 236101 (2014), URL http://link.aps.org/doi/10.1103/PhysRevLett.113.236101. 1.6

CHAPTER 2. EQUIPMENT AND TECHNIQUES

2.1 Introduction

The main theme of this thesis is studying the behavior of atoms at surfaces. In order to have the sensitivity and precision to study diffusion and nucleation, delicate instruments must be used in a controlled environment. The best way to control the sample environment is to house the experiment in ultra-high vacuum, below 10^{-9} torr with the target pressure around 5 x 10^{-11} torr. This isolates the sample surface from being flooded by gas atoms and dust particles naturally in the air that are not part of the designed experiment.

In order to study the surfaces, the Tringides group uses two main pieces of equipment: Scanning Tunneling Microscopy (STM) and Spot Profile Analyzing Low Energy Electron Diffraction (SPALEED). The STM uses a needle to raster across the surface creating a 3D contour plot of the surface. The SPALEED uses electrons as waves to form a diffraction image of the surface. The operation of both of these instruments requires an ultra-high vacuum. While scanning tunneling microscopy has been operated at atmospheric conditions to study the conductivity of DNA molecules[1], this lowers the reliability of the needle tip, which is critical to having high resolution for surface science experiments. The SPALEED uses a beam of electrons to reflect off the surface, which requires ultra-high vacuum to decrease the number of gas atoms present that could absorb or scatter the electrons before reaching the sample or detector. The details of these techniques will be discussed in the following sections.

2.2 Ultra-high vacuum processes

Isolating experiments in ultra-high vacuum chambers is a common practice across many areas of physics research. In order to study the physical processes with high sensitivity the

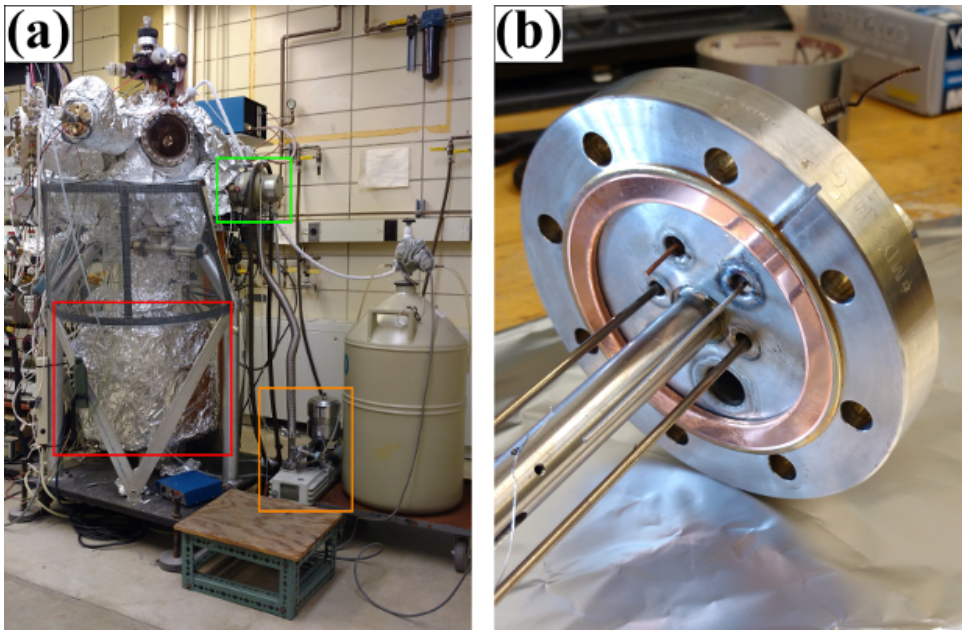

Figure 2.1 (a) SPALEED ultra-high vacuum chamber covered in aluminum foil. Pumps are highlighted by colored boxes and the liquid nitrogen dewar is on the right. (b) CF flange connection with copper gasket in place. Location of the knife edge can be seen on the copper gasket where the color changes. The color change is due to exposure to atmosphere during system baking.

environment must be controlled as much as possible. The best conditions to control the environment are ultra-high vacuum chambers where most of the air can be removed. For example, at standard atmospheric pressure (1 atm = 760 torr) it takes about 1 nanosecond for the surface to be hit by enough gas molecules to cover the surface. Even if only a fraction of these gas molecules stick to the surface or react with the surface, the sample's surface composition is completely changed in less than a second. At our target pressure of 5 x 10^{-11} torr it would take about five and a half hours for the surface to be hit by enough gas molecules to cover it. In addition to environment control, many pieces of experimental equipment use electric fields, magnetic fields, needles, electrons, or photons to probe the surface and require ultra-high vacuum to operate with the required sensitivity.

Ultra-high vacuum chambers are made out of stainless steel with CF flanges to connect modular parts. Figure 2.1(a,b) show a SPALEED ultra-high vacuum chamber and CF flange respectively. Chamber wall thicknesses are between 1/8 and 1/4 of an inch. CF flanges use a

metal knife edge on the flange to cut into a copper gasket to create a tight seal with flange sizes ranging from 1 inch to 16.5 inches. The flanges are held together with 6 to 20 steel nuts and bolts depending on the size of the flange. The tightening of the bolts must be carried out carefully and uniformly to ensure a uniform onset of pressure across the copper gasket and prevent any leaks. Common modular parts include windows, electronic feedthroughs, manipulator attachments, transfer lines, and specialized equipment. The specialized equipment on our SPALEED system includes the SPALEED, Auger Electron Spectroscopy, deposition sources, ion gauge, ion pump, turbo pump, and mass spectrometer.

Once the system flanges have been appropriately mounted and sealed, a series of pumps and preparation steps are used to achieve ultra-high vacuum. First a roughing (mechanical) pump (Figure 2.1(a) orange box) is used to achieve to a pressure of $\sim 10^{-3}$ torr. The next step uses a turbomolecular (turbo) pump (Figure 2.1(a) green box). Inside the turbo pump are multiple sets of rotors that can rotate at over 10,000 rotations per minute (rpm) and strike gas molecules, giving them a net momentum towards the backside of the turbo pump. The turbo pump starts at an initial low rpm setting and as the vacuum improves it speeds up with full speed being reached around 10^{-6} torr. The backside of the turbo pump must be connected to a roughing pump to remove the pumped gas molecules. With the turbo pump a pressure of 10^{-8} torr can be reached, but it is not good at removing light gases such as hydrogen and helium.

There is another issue with passing the 10^{-8} torr mark: when a metal chamber surface is exposed to atmosphere, gas molecules absorb into the metal. When the inside of the chamber is pumped down to 10^{-8} torr these absorbed gas molecules diffuse out of the metal, providing a constant source of gas molecules that can last for weeks and preventing the chamber from being pumped down. The remedy is to "bake" the system by heating in order to drive the absorbed gas out of the chamber walls quicker. Temperatures are slowly increased to prevent the pressure from rising too quickly and non-uniform expansion in the chamber, flanges, and modular attachments. Various parts have different maximum temperatures with specialized equipment like the SPALEED having a max temperature of 150°C, while deposition sources can be heated to over 200°C.

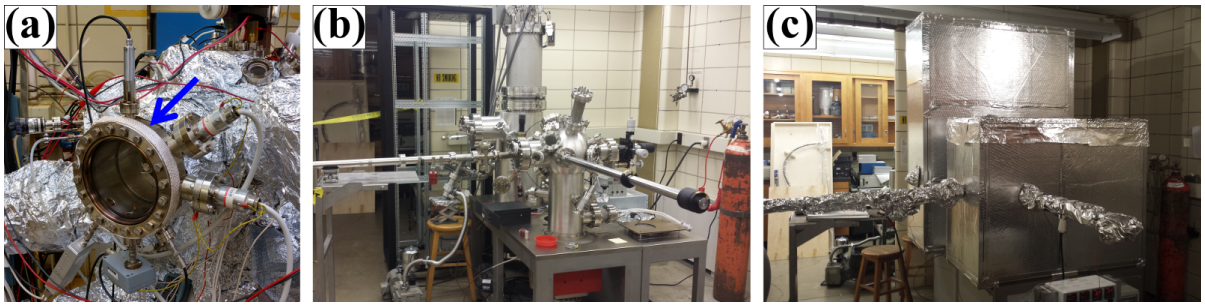

Figure 2.2 (a) The blue arrow points to a white fiberglass tape wrapped around the SPALEED flange. The rest of the chamber is covered in fiberglass tapes, which are then covered in aluminum foil. (b) STM ultra-high vacuum chamber midway through construction without the baking box. (c) Same STM chamber with the baking boxes.

There are two main methods of baking a system. The first is having fiberglass tapes wrapped around the chamber and flanges to heat the system (Figure 2.2(a) blue arrow). In this method all parts are covered with aluminum foil to ensure even heating and to create a small pocket of air as insulation to keep the flange hot. This has the advantage that particular flanges can be set to different temperatures depending on their maximum temperature settings. The second method is to have thermally insulated panels completely surround the entire chamber, and heat the entire chamber to the same temperature. Figure 2.2(b) and Figure 2.2(c) show an STM chamber before and during baking respectively. This method is simpler in execution, but requires that the temperature be kept below the smallest maximum temperature for a flange. The second method also requires slightly longer baking times since the overall temperatures are slightly lower. Throughout the baking process the turbo pump is running, removing the desorbed gases from the system. Once the baking process is finished the turbo pump is typically shut down and the turbo pump flange is sealed behind a gate valve.

Either during the bakeout or after the bakeout is completed the next level of pumping–ion pumping (Figure 2.1(a) red box)–is activated. An ion pump has two metal panels with five to seven thousand volts between them. This creates an electric field which can ionize gas particles that wander between the panels. Once ionized, the particles are accelerated and implanted in the cathode, preventing them from free movement around the chamber. With an ion pump

the pressure can reach the low 10^{-10} torr or high 10^{-11} torr range. Ion pumps do not have any moving parts or oil, which makes them good for pumping during a sensitive experiment. The down side is the ion pump does not actually remove the gas from the chamber and over time imbedded gas molecules can diffuse out of the cathode. This is particularly common with hydrogen, which requires the final pumping step.

The final pumping step is titanium sublimation. In this step a ∼45 amp current is run through titanium rods inside a section of the vacuum chamber. This covers the chamber walls with titanium, which is a very good getter for gas molecules and reacts to form a chemical solid, trapping the gas molecules. This is particularly important to remove hydrogen from the system, since the turbo pump is poor at removing light elements and hydrogen trapped by the ion pump can diffuse out of the cathode and back into the chamber. In addition to the hydrogen in the chamber when the chamber is sealed, hydrogen gas is light enough to be able to diffuse through the steel chamber walls. Over the course of months this can raise the pressure in the vacuum system to above 10^{-10}, requiring another round of titanium sublimation pumping.

While these pumping steps can get the base pressure of the system to 10^{-11} torr, there are many ultra-high vacuum procedures that require specific parts of the system to be heated above 200°C. These elevated temperatures can cause an extra release of gas atoms, raising the background pressure to 10^{-9}. To avoid these high pressures during experiments, the deposition sources, electron filaments, samples, and annealing stations are outgassed at their operating temperatures so the base pressure in the system during experiments will not rise above 2 x 10^{-10}.

Even when assembly and pumping procedures are carefully followed it is still possible to develop a leak in the vacuum chamber. Figure 2.3(a) shows an example mass spectrum with peaks labeled during a leak while Figure 2.3(b) shows a mass spectrometer ionizer assembly containing the filament and qualrupoles on the right middle. The most common source for leaks after opening and resealing a chamber are copper CF gaskets incorrectly aligned which can cause leaks in the 10^{-3} torr to 10^{-10} torr range. Leaks in the 10^{-3} to 10^{-7} torr range are noticed quickly due to the turbomolecular pump not being able to ramp up to full speed with the most likely locations of the leaks at any flanges that were exchanged. Other possible leak

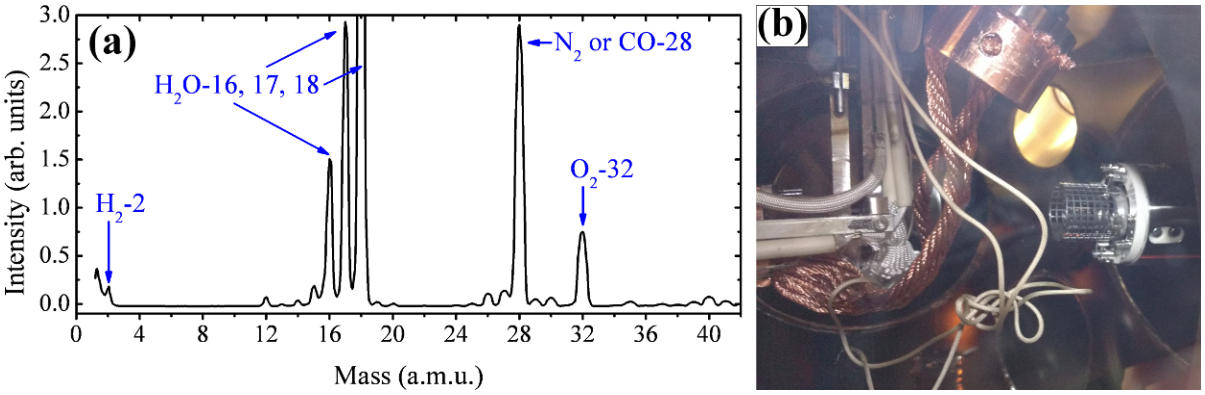

Figure 2.3 (a) Mass Spectrum using a commercial quadrupole mass analyzer with common peaks during a leak labeled. (b) Inside view of the SPALEED chamber. On the right middle is the mass spectrometer ionizer assembly. The copper cap at the top middle is the end of the liquid nitrogen cryostat and the copper braids transfer heat from the sample to the cryostat.

locations are electric feedthroughs, water lines, and manipulator joints. Some leaks are small enough that the leak might not be noticed until after the bakeout. After it has been determined there is a leak, the next step is locating the leak. One method is spraying acetone or methanol over locations of possible leaks while watching the vacuum gauge. As these solvents cover a leak the ion gauge reading can fluctuate. Another method is using helium to detect the leak. There are commercial mass analyzer systems specifically designed to track the helium peak, but any mass spectrometer connected to the vacuum system can be used. In both cases the mass analyzer is turned on and helium from a gas cylinder is carefully sprayed over the system, usually with a regulator and needle to limit the flow rate. The mass analyzer will have a spike in the helium peak when the gas spray is near the leak. One concern is helium over spraying, giving a false positive while the spray needle is still far away from the actual leak. Over spraying can be reduced by using plastic bags to limit the regions of the chamber that are exposed to helium. After the leak is located, appropriate steps can be used to fix the leak.

After the pumping and outgassing procedures have been completed it is time to prepare the samples for experiments. This is done by flashing the sample, which means quickly raising it to a high temperature to remove layers from or reform the surface. The two main samples worked with were Si(111) and graphene grown epitaxially on a bulk SiC(0001) crystal. The

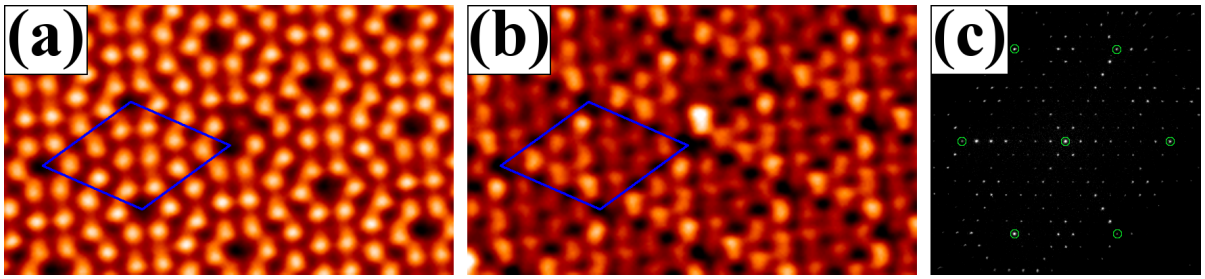

Figure 2.4 Si(111)-7x7 images (a) Filled states STM image with one 7x7 unit cell in blue. (b) Empty states STM image with one 7x7 unit cell in blue. Note the bright spot in the center of the empty states image shows up as a dark spot in the filled states image. (c) SPALEED 2D diffraction pattern with the specular and Si{10} spots circled in green.

Si(111) samples have a capping SiO_2 layer to prevent atmospheric gases from reacting with and damaging the surface, in particular CO_2 and hydrocarbons. Exposure of a pure Si crystal to carbon compounds can contaminate the surface by forming patches of SiC, which are not able to be removed through flashing the sample due to SiC having a higher evaporation temperature than silicon's melting temperature. A fresh Si(111) sample has the SiO_2 layer removed by multiple rounds of flashing to around 1250°C. In each flash the sample is heated quickly to the maximum temperature and held there for around 15 seconds. It is then immediately dropped to 900°C and allowed to cool at a rate of 2°C/s to 750°C. From 750°C to 700°C the sample is cooled at 1°C/s as the temperature moves through the 7x7 phase change. From 700°C on the sample is cooled at 2°C/s. After flashing, the 7x7 pattern is checked with the STM or SPALEED to ensure the 7x7 reconstruction was formed properly and if not the flashing procedure is repeated. Figure 2.4(a-c) shows STM scans of filled and empty states and a SPALEED diffraction pattern for the Si(111)-7x7 surface.

The SiC samples have the Si face epitaxial ready. The graphene overlayer–which is the main focus of the experiments–must be formed by flashing the sample. The SiC crystal has a rich phase diagram with the surface moving through several phases when formed in ultra-high vacuum[2,3]. The details of this phase diagram are still being debated in the literature[4,5], with much of the debate surrounding electronic properties and the moiré pattern–a long range pattern forming as the result of the mismatch of two shorter lattices with different lengths

and/or rotations. Initially the SiC crystal starts in a 1x1 phase. Next, a 3x3 phase forms around 850°C. This transitions to a $\sqrt{3}$ x $\sqrt{3}$-R30° phase at 950°C. Around 1050°C Si atoms begin desorbing, leaving behind a carbon rich layer directly above the SiC substrate called the buffer layer with a pattern termed $6\sqrt{3}$ x $6\sqrt{3}$-R30° in the literature. This buffer layer has a very similar arrangement of carbon atoms to graphene and is sometimes termed 0^{th} layer graphene, but around 1/4 of the carbon atoms are covalently bonded to the SiC surface, disrupting the typical graphene band structure and electrical properties[4]. Flashing to 1150°C will cause enough Si to desorb that a second carbon rich layer can form next to the SiC substrate which creates a new buffer layer and decouples the original buffer layer from the substrate, forming the 1^{st} true layer of graphene. This 1^{st} layer graphene has electrical properties very different than the buffer layer and in many experiments is the desired layer to study due to the linear band structure near the K point in reciprocal space. The overall dominate repeating cell and moiré pattern observed in STM and LEED for the buffer+1^{st} layer graphene system is SiC(0001)-6x6-R0°. Further elevation of the temperatures can create additional layers of graphene[6]. Long flashes at these elevated temperatures can also begin formation of the next layer of graphene. This creates a situation where the initial forming temperature and flash time are critical in determining the initial surface, and repeated flashing to remove deposited material can actually change the number of layers of graphene present. Two polymorphs of SiC were used for the graphene experiments. All STM experiments used 6H-SiC(0001) and all SPALEED experiments used 4H-SiC(0001). The main difference between these two polymorphs is the number of stacked layers in the unit cell–four layers and six layers for 4H and 6H respectively[7]–with the number of layers of SiC having a minimal impact on the graphene formed. Figure 2.5(a) shows an STM image of the graphene surface. The 6x6 moiré pattern appears as bright and dark patches. Figure 2.5(b) is a schematic overhead model of one layer of graphene. Figure 2.5(c) is a side view of graphene grown on 4H-SiC(0001). The buffer layer is closest to the SiC surface which has some bonding to the buffer layer and some dangling bonds (schematic). The 1^{st} true graphene layer is at the top of the image.

Once the sample has been prepared and the initial surface has been properly characterized, the next step in ultra-high vacuum experiments is to deposit the material of interest. There

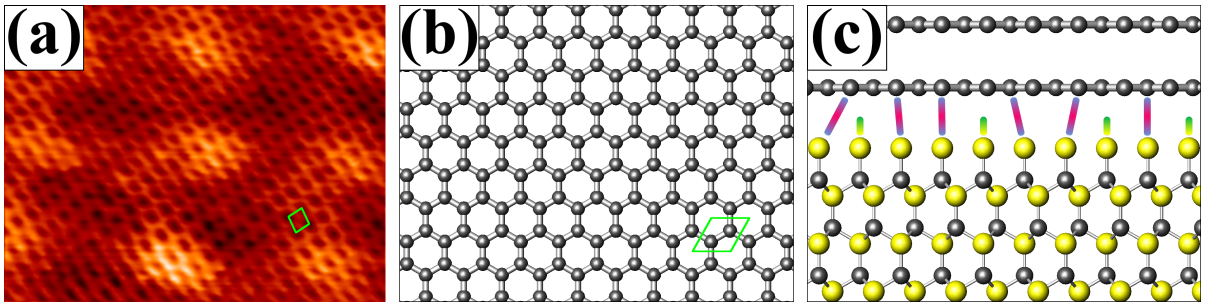

Figure 2.5 (a) 6.4 x 5.0 nm^2 STM image of graphene with one graphene unit cell shown in green. (b) Overhead model of graphene structure with one unit cell shown in green. The basis has two atoms. (c) Side view schematic model of the graphene on SiC(0001) Si terminated system. Carbon atoms are grey, Si atoms are yellow. The carbon layer closest to the SiC surface is the buffer layer and has schematic bonds (not to scale or location) between some buffer layer atoms and surface Si atoms. Other Si atoms have dangling bonds. The 2^{nd} carbon layer is the 1^{st} true layer of graphene.

are many methods for deposition, but the research in this thesis used molecular beam epitaxy via thermally activated evaporation physical vapor deposition. Physical vapor deposition uses a physical process, such as heating or ion sputtering, to free atoms from the surface and form a vapor that is then directed at a surface to form a film. This is in contrast to chemical vapor deposition which passes chemical precursors over a surface that react to deposit the desired film. Our deposition sources heat a crucible containing the deposition material until the material is hot enough to evaporate. The evaporated atoms travel in a straight line in the vacuum since there are few gas atoms to impede their path. A shutter is placed between the evaporator and sample to allow the source to heat up and the flux to stabilize before deposition. The flux rates used are low enough to allow epitaxial growth; there is enough time between incoming atoms for the deposited material to diffuse around and form crystal lattices with minimal strain. Examples of samples are shown in Figure 2.6(a,b) and an evaporator for deposition is shown in Figure 2.6(c).

After a material has been deposited on the surface, a critical step of the analysis is to determine how much was deposited. The method for determining the amount deposited varies greatly between STM and SPALEED. For the STM the method is fairly straight forward. An

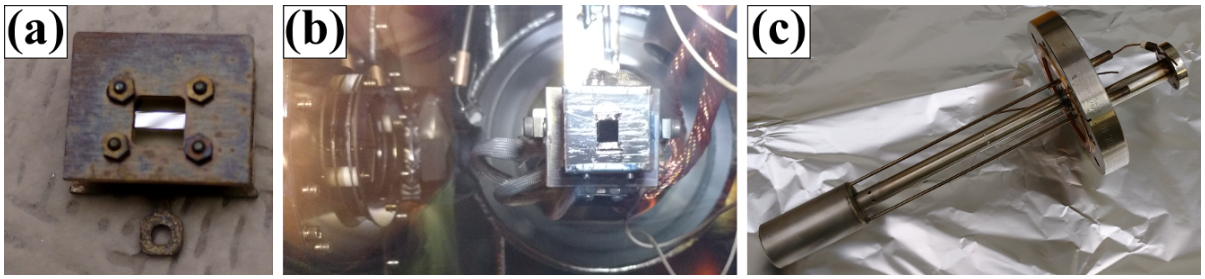

Figure 2.6 (a) Sample holder for STM with SiC sample. Si(111) samples also use the same sample holder and are similar size. (b) SPALEED sample holder *in-situ* seen as a bright metallic square on the right half of the image. 4H-SiC(0001) sample is a dark square at the center of the sample holder. The series of metal rings with white spacers on the left half of the image is the SPALEED entrance lens, and in normal SPALEED operation the sample would be rotated to face the entrance lens. (c) Evaporator for depositing metal. A crucible containing the metal fits in the lower left end. Two thin tubes to transport cooling water run from the flange to the crucible. Electric feedthroughs on the flange allow wires to carry a current to the crucible, which uses resistive heating to heat the source material.

STM scan can directly view the height and portion of the surface covered, then integrate to determine the total volume on the surface and use known crystal structures for the material to determine the number of monolayers deposited. There are always error bars on the calculated flux rate due to tip convolution effects with a particular concern for the perimeters of islands, but calibrating from a series of depositions where the surface coverage–hence the relative island volume to island perimeter ratio–increases can account for tip convolution.

Diffraction can also be used to calibrate the flux during deposition since it is a real time method, however benchmarks for surface growth modes or growth transitions need to be determined. In the Pb/Si(111)-7x7 system, it has been determined that crystalline Pb(111) island formation occurs at 1.22 ML of deposited Pb at 200 K[8,9]. For Dy deposited on graphene at 100 K, the Dy grows as an amorphous ∼2 layer thick film across the graphene. The attenuation of the intensity of the graphene spots and characteristic buffer layer 6x6 spots can be observed to determine when the surface is covered by the 2 layers film of Dy. Without prior knowledge that the Dy is growing as a ∼2 layer thick amorphous film, instead of a 1 layer or 3 layer film, calibration using diffraction would require systems with ordered Dy phases. Using diffraction

oscillations from Reflection High Energy Electron Diffraction during deposition studies is the routine method to determine the deposited amount and film thickness.

Although the experiment is contained within the ultra-high vacuum chamber and once sealed there are few chemical safety hazards, there are other hazards specific to high vacuum chambers. Both the ion gauge to determine the pressure and the ion pump to pump the vacuum system require high voltages in the 3 kilovolt to 8 kilovolt range to perform their functions. While the feedthroughs are shielded and the cables are well insulated, extreme caution must be taken to not disrupt these due to their lethal voltages. In general, when working with electrical systems no connection cables should be moved or unplugged unless the control box is off, the main power cable is unplugged, and the control box has had time for any capacitors to discharge. The other major safety concern is chamber implosion and is fairly unique to ultra-high vacuum systems. If a window or other delicate part develops a mechanical weakness, such as a crack, the difference in pressure between outside the chamber and inside the chamber could cause a full structural failure and allow air to rush into the chamber. This would not play out like a scene from the movies in outer space where the air from the entire room is rushing towards the vacuum of outer space–those scenes are not a realistic example of air flow. The volume of vacuum in the chamber is small enough that it would have a negligible effect on the room's pressure. Instead the sudden rush of air into the chamber could potentially blow out all of the other windows on the chamber, showering the entire room with glass fragments. Even with these concerns a vacuum chamber is considerably safer than a high pressure chamber. At most, a vacuum chamber has a difference of 1 atmosphere between the inside and outside of the system which puts an upper limit on the difference of force per unit area, while high pressure systems do not have an upper bound on the difference in force per unit area. Awareness and training of possible concerns involving ultra-high vacuum chambers allows experiments to run smoothly. The following sections will cover the particulars of the main experimental equipment: Scanning Tunneling Microscopy and Spot Profile Analyzing Low Energy Electron Diffraction.

2.3 Scanning tunneling microscopy

The first investigations into the microscopic world used a lens and visible light to bring the images into focus. For many years microscope magnification was improved by using better lenses. However, a wavelength of light has a minimum resolution similar to its wavelength which prevented further improvement in using visible light in magnification. Since the minimum wavelength of optical light is around 400 nm, optical microscopes cannot approach viewing atoms on the order of ∼0.3 nm. Over the decades techniques have been developed to achieve magnification to the level of individual atoms through other means. In 1951 the field ion microscope used a sharp metal tip placed under high voltage to create ionized gas atoms that were captured by a detector and formed an image of the atoms on the metal tip[10]. The 1980's brought two important pieces of equipment: atomic force microscopy (AFM) and scanning tunneling microscopy (STM). Both of these techniques are scanning probe techniques that use a very sharp needle, or scanning probe tip, to raster across a surface and record the surface profile. This achieves both extremely high magnification and gives height and additional information about the surface. The tips raster in the x-y plane by being mounted on a tube of a piezoelectric material–a crystal that expands and contracts based on the voltage that is put across it. The piezoelectric material allows the location of the tip to be controlled at the sub-nanometer level resulting in atomic resolution. The STM uses a current running through the tip to determine tip-sample separation and adjust the height of the tip as necessary, while AFM uses the force between the sample and a tip on a cantilever with a known spring constant to record the deflection of the tip. Using a current limits the STM to working with conducting samples, but the AFM can be used on insulating samples. In general, the STM has better atomic resolution and the AFM is used for scans in the micrometer range. The topics of this thesis are all on conducting surfaces with a focus on the atomic processes, and hence STM is best suited for this research.

The basic principle of the STM is a conducting STM tip approaches a conducting surface, but does not touch the surface. A voltage is placed between the tip and the sample. According to classical mechanics there should not be a current flowing since the tip and the sample are not

touching and there are no other atoms around to form an electrical contact since the experiment is in an ultra-high vacuum chamber. There is a potential barrier for the electrons to hop between the tip and surface that classically they cannot overcome. However, in quantum mechanics a particle has a non-zero probability to tunnel across a barrier and appear on the other side. This probability is based on the height of the barrier Φ and the tip-sample separation distance z.

The current for the STM has been modeled by the tunneling current between two electrodes separated by an insulating barrier, and can be calculated with Fermi's golden rule[11]:

$$I_t \propto \int_{-\infty}^{\infty} |M(E)|^2 g_T(E - eU) g_S(E) |f(E - eU) - f(E)| dE \tag{2.1}$$

where f is the Fermi function, U is the bias voltage applied to the STM tip, M is the tunneling matrix element containing the barrier height; barrier width; and orbital character of the tunneling electrons, and $g_{T,S}$ is the density of states for the tip and the sample respectively. The result of the integration is the current is very sensitive to changes in the tip-sample separation due to an exponential based on the z distance, which contributes to the remarkable resolution of the STM in the direction perpendicular to the surface.

Although the tip behaves like it is making a 3D contour plot of the surface, the actual result is the tip is making an image of electron orbitals of the atoms on the surface. This difference is usually negligible for scans larger than tens of nanometers, but atomic resolution images can show the differences in the local density of states of the surface. In particular, orbitals for electrons from atoms below the first layer can sometimes be probed. For a particular measurement, the electron orbitals around atoms can either have electrons present corresponding to filled states, or not have any electrons corresponding to empty states. Putting the tip at a positive voltage relative to the grounded sample causes a current to flow from the tip to the sample, and electrons to flow from the sample to the tip, which probes the filled states on the sample. Likewise, putting the tip at a negative voltage probes the empty states on the sample. Examples of the differences between filled and empty states are shown in Figure 2.4(a,b). Adjusting the magnitude of the voltage also affects the states probed, with tiny voltages probing the electron states just above and below the fermi surface, and increasing the voltage probes

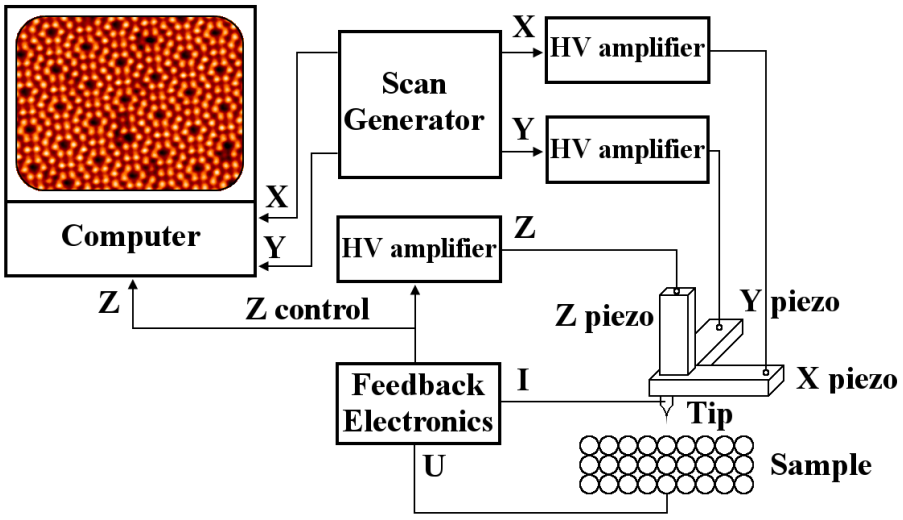

Figure 2.7 Simple schematic of the wiring of an STM. A computer controls the scan generator for the x and y directions, and the z direction is on a feedback loop based on the operating mode and tunneling current from the tip. After Figure 7.15 of Oura[13].

an integration of the states from that energy to the fermi level (where the energy is the voltage times the charge of the electron and in units of electron volts has the same magnitude as the voltage). The Tersoff-Hamann model is a first order 3D estimate that shows for low voltages and flat density of states of the tip (s-orbital like density of states) the energy dependent part of the current is a function of the density of states of the sample alone[12].

Figure 2.7 shows a simple schematic of the electric wiring for the STM. The computer has a control interface to allow a user to choose the scan location, scan parameters, and scan mode, and then generates the appropriate signals for the scan. The tunneling current and z-piezo voltage are collected by the computer which continuously processes the incoming data, correlating the tunneling current with the appropriate x-y coordinates and displaying it as a raw STM image that roughly conforms to a 3D contour plot of the surface.

The choice of scan mode changes how the feedback electronics behave. In constant current mode, the tunneling current is directed into feedback electronics that control the voltage across the z-axis piezo tube and changes the height of the tip in response to the current, keeping the tip constantly about 0.5 nm above the surface. The majority of scans are run in constant current mode. In constant height mode, the feedback electronics are disabled and the voltage

and height are set, while the current is recorded as the tip rasters across the surface. Constant height mode requires the selected scan area to have few, if any, steps across the surface due to the risk of crashing the tip into the sample.

A third scanning mode is called Scanning Tunneling Spectroscopy. There are multiple types of spectroscopy that can be done, including I(V) and I(Z), but the most common is I(V). In this mode the tip moves to a particular location on a grid, then the z-axis piezo is disabled. The tip has a spectrum of voltages placed on it with the response current recorded. After the voltage sweep is completed the z-axis piezo is re-engaged and the tip moves to the next location on the grid. After the data has been collected, images showing the surface's $\frac{dI}{dV}$ at a particular V can be constructed. For a particular location the calculation of $\frac{\left(\frac{dI}{dV}\right)}{\left(\frac{I}{V}\right)}$ is proportional to the local density of states. Scanning tunneling spectroscopy can be used to learn about the bonding on the surface and identify the species of atoms at particular locations[13].

Several steps are taken to reduce noise and vibrations so the tip can be positioned correctly. The piezo tubes have a high voltage amplifier near the system so the electronic noise is reduced and the electronics can be controlled with lower voltages from the computer. In order for the piezo tubes to achieve their sub-nanometer tip positioning, there are multiple layers of vibration isolation. First, the entire vacuum chamber is put on an optical table floating on air pistons. Sometimes heavy metal plates are added to the table to increase the mass and decrease the frequency of any oscillations. Next, inside the vacuum chamber the STM equipment is hung from long, soft springs to further reduce oscillations. Finally, the STM equipment has copper plates housed next to–but not touching–magnets attached to the wall to induce eddy-current breaking.

After scans have been taken there are several processing steps before being able to extract useful information from the STM images. The first step is to flatten the image. Both commercial and in-lab programs have been developed to assist in image flattening. Typical strategies involve identifying areas that should be the same height, such as substrate terraces. Next, the z-calibration should be checked on a step with a known height. Typically height calibration can be completed once and will not change unless maintenance or repair is done on the piezo stack. While the x-y piezos are very accurate in their positioning, sometimes there is a drift in location

during a scan. Repeated scans of the same area might need to be calibrated to each other to allow direct comparison. Smaller scan regions showing atomic resolution can be calibrated according to a known lattice. Following these adjustments, the particular measurements or studies of the surface system can be completed.

The Scanning Tunneling Microscopy is an amazing instrument for studying surfaces. It gives real space information about the locations of electron orbitals on the surface and can range from micrometer scans to atomic resolution. Changing to particular modes allows the study of the density of states and bonding of surface atoms. While it is limited to conducting samples and can only investigate the surface of samples, it does an unparalleled job in terms of resolution among scanning probe techniques.

2.4 Spot profile analyzing low energy electron diffraction

2.4.1 Electron diffraction

Diffraction is a general term to describe the spreading out of waves when they encounter an object or pass through a narrow slit. If the linear dimensions of the material the wave is interacting with are similar to the wavelength of the wave, the interference between wave forms produces a pattern. Diffraction is widely used to study condensed matter systems due to the crystalline, repeating structure causing interference between waves and allowing sharp diffraction spots to form. Atomic distances are on the order of a few Ångstroms so typically x-rays, free neutrons, and free electrons are used as the diffraction waves. Of these media, electrons are the most strongly scattered by matter, scattering off of anything with a charge: the nucleus and the electron cloud. Electrons with energies of 20 eV to 200 eV have a mean free path of only a few atomic layers which makes electron diffraction patterns surface sensitive. This is also the range of energies where the wavelength of electrons is similar to the atomic lattice distance. Following from the de Broglie equation for wavelength [13]–

$$\lambda = \frac{h}{p} \approx \frac{h}{\sqrt{2m_e E}} = \sqrt{\frac{150.4}{E}} \text{ Ångstroms} \tag{2.2}$$

where h is Planck's constant, p is momentum, m_e is the mass of the electron, and E is the energy of the electron in eV–the electrons with energies of 20 eV to 200 eV have wavelengths

from 2.74 Ångstroms to 0.87 Ångstroms. The most common form of electron diffraction is called Low Energy Electron Diffraction (LEED). In this experimental setup an electron gun produces free electrons that are accelerated towards a sample. The electrons diffract off the surface and strike a phosphor screen causing the screen to glow, which is then photographed to capture the diffraction pattern. The wave pattern of the electrons interact destructively for most directions, but when the conditions for Bragg's law are met they have constructive interference creating bright spots in the diffraction pattern. In Bragg's law

$$\lambda_e \mathrm{m} = 2d\sin(\theta) \tag{2.3}$$

where λ_e is the wavelength of the electron, m is an integer, d is the lattice spacing on the surface, and 90°minus θ is the angle from normal incidence. The overall result is any periodicity of atoms on the surface results in a spot in the diffraction pattern. In LEED the typical transfer width–the length that an instrument behaves as an interference detector[14]–is ∼100 Ångstroms resulting in the instrumental contribution to the spot width being around 1 to 3%BZ for most systems[13] requiring the features under study to be closer than 10 nm. An example of a 2D pattern from the SPALEED is shown in Figure 2.8. In addition to the expected graphene spots and SiC spots, a host of other moiré spots appear from the co-incidence of the two main lattices.

In addition to Bragg's law there is another formulation called the von Laue approach which does not focus on any particular part of a crystal. Instead it says that the crystal has atoms at all sites $\mathbf{R}$ of the Bravais lattice, and each of these can re-radiate the incident waves in all directions. In order for a sharp diffraction peak to form, the rays from all sites must interfere constructively. The derivation follows Ashcroft Chapter 6, which is the general formulation for bulk diffraction using x-rays[15]. To start in Figure 2.9(a), there is an incident plane wave $\mathbf{k_i}$ with wavelength λ in direction $\hat{\mathbf{n}}_\mathbf{i}$ and final scattered plane wave $\mathbf{k_f}$ with the same wavelength λ and new direction $\hat{\mathbf{n}}_\mathbf{f}$, i.e. elastically scattered.

$$\mathbf{k_i} = \frac{2\pi\hat{\mathbf{n}}_\mathbf{i}}{\lambda} \tag{2.4}$$

$$\mathbf{k_f} = \frac{2\pi\hat{\mathbf{n}}_\mathbf{f}}{\lambda} \tag{2.5}$$

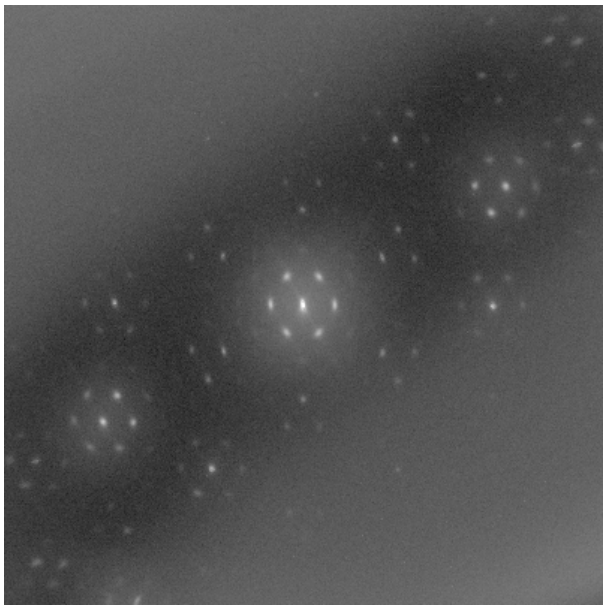

Figure 2.8 Example of a SPALEED 2D pattern with the specular in the center and extra moiré spots visible all across the scan. Only part of the BZ is accessible and the outside bright areas originate from scattering off the sample holder.

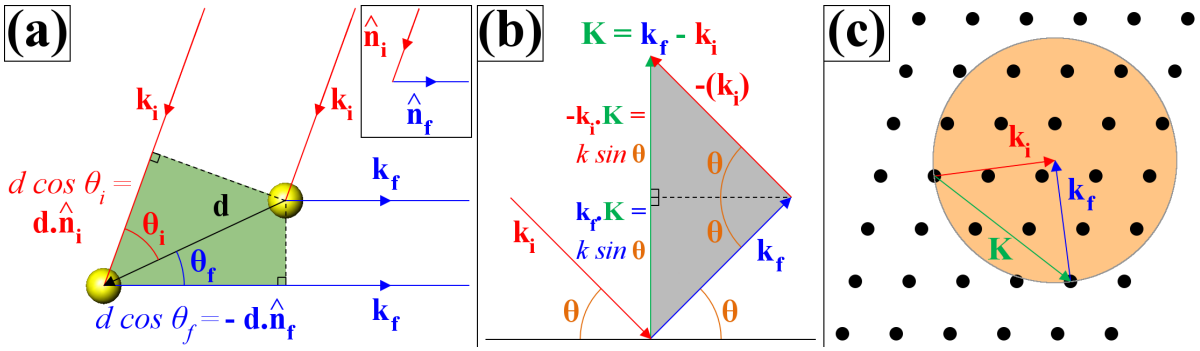

Figure 2.9 (a) Diagram of the difference in path length for two scattered rays from two points separated by d (after Figure 6.4 of Ashcroft[15]). (b) Diagram of the reciprocal lattice vector $\mathbf{K} = \mathbf{k_f} - \mathbf{k_i}$ (after Figure 6.6 of Ashcroft[15]) where $\mathbf{k_f}$ is specular scattering. (c) Simple Ewald sphere construction (after Figure 6.7 of Ashcroft[15]) for a bulk crystal and x-ray scattering.

For two particular scattered wave vectors separated by distance d, the path difference must be an integer number of wavelengths:

$$\mathbf{d} \bullet (\mathbf{k_i} - \mathbf{k_f}) = 2\pi \mathrm{m} \tag{2.6}$$

Equation 2.6 can be generalized to all scatterers in the Bravais lattice separated by a Bravais lattice vector $\mathbf{R}$:

$$\mathbf{R} \bullet (\mathbf{k_i} - \mathbf{k_f}) = 2\pi \mathrm{m} \tag{2.7}$$

Or equivalently:

$$e^{i\left(\mathbf{k_f} - \mathbf{k_i}\right) \bullet \mathbf{R}} = 1 \tag{2.8}$$

Comparing Equation 2.8 to the definition of a reciprocal lattice:

$$e^{i\mathbf{K} \bullet \mathbf{R}} = 1 \tag{2.9}$$

by the von Laue condition constructive interference occurs when the change in wave vector of the scattered rays is a vector of the reciprocal lattice $\mathbf{K}$=($\mathbf{k_f}$ - $\mathbf{k_i}$), where $\mathbf{k_f}$ and $\mathbf{k_i}$ have equal lengths due to elastic scattering[15]. With this, the simple geometry picture in Figure 2.9(b) shows

$$|\mathbf{K}| = 2|\mathbf{k}| \sin(\theta) \tag{2.10}$$

By converting back to real space, the von Laue condition is completely equivalent to Bragg's law. A useful picture called the Ewald construction helps visualize when spots are produced shown in Figure 2.9(c). In the Ewald construction the reciprocal lattice points are drawn. The incident wave vector $\mathbf{k_i}$ is drawn from the origin, and the final wave vector $\mathbf{k_f}$ is drawn to a reciprocal lattice point, with the difference $\mathbf{K}$ shown as well. Then, a sphere is drawn around the point of $\mathbf{k_i}$ with radius k because energy is conserved in elastic scattering. Whenever a reciprocal lattice point intercepts the surface of the sphere, a spot will be produced by Bragg reflection. The radius of the sphere and the initial angle of $\mathbf{k_i}$ can be varied to move the Ewald sphere through the reciprocal lattice points. This construction can help predict the angles of the peaks in a diffraction pattern.

When working with low energy electrons, the diffraction is coming from the surface and mimics a 2D surface. By setting the real space lattice perpendicular to the surface, c, to infinity, c^* goes to zero and the Ewald sphere becomes a circle with the reciprocal lattice points in the c^* direction becoming rods. These rods can then be probed by varying the energy[13]. The intensity of the rods as energy is varied is based on the structure factor[15]:

$$S_{\mathbf{K}} = \sum_{j=1}^{n} f_j(\mathbf{K}) e^{i\mathbf{K}\bullet\mathbf{d}_j} \tag{2.11}$$

where $\mathbf{K}$ is the reciprocal lattice vector, $f_j(\mathbf{K})$ is the atomic form factor based on the electronic charge distribution of atom j, and d_j is the position of the j^{th} atom in the basis. The $\mathbf{K}$ dependence of the form factors can allow the variation of the Bragg peak intensities to be matched to the correct crystal structure[15].

2.4.2 SPALEED

The Spot Profile Analyzing Low Energy Electron Diffraction (SPALEED) is similar to regular LEED in the overall diffraction mechanism, but the equipment setup greatly differs. Figure 2.10(a) shows a typical commercial SPALEED system with regular LEED capabilities. In regular LEED the electrons are created by an electron gun, go straight to the sample, and diffract back to the phosphor screen and grid producing the diffraction pattern. In SPALEED only a tiny portion of the diffraction pattern is probed at any one time. The electron beam shoots electrons towards the sample, but the electrons take a curved path due to potentials on the octopole plates. A few centimeters before the sample the electrons are focused by the entrance lens. The entrance lens can be viewed on the left half of Figure 2.6(b). The focal point of the entrance lens is not the sample. Instead, some of the diffracted electrons follow almost the same path as the initial beam and are focused on a channeltron a few centimeters from the electron gun. A channeltron is a very sensitive electron multiplier and detector that has a range of 10^6 counts/s. This provides the intensity for one point in reciprocal space. Figure 2.10(b) shows the SPALEED control unit adjusts the angle $\alpha + \Delta/2$ that the electrons hit the sample by changing the potentials on the octopole plates. The angle difference Δ between the initial and final electron beams is fixed due to the geometry of the electron gun and channeltron and

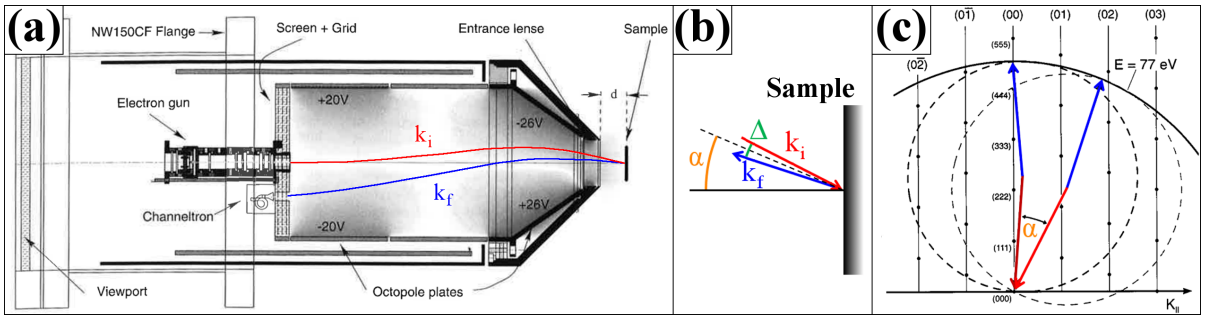

Figure 2.10 (a) Schematic of a commercial SPALEED system with the paths of electron $\mathbf{k_i}$ and $\mathbf{k_f}$ highlighted (after Figure 3.1 of Horn-von Hoegan[16]), (b) Geometry of electrons hitting the sample[16], (c) Ewald sphere for SPALEED. Here $\mathbf{k_i}$ and $\mathbf{k_f}$ have a fixed angle between them and diffraction spots are probed by changing α (after Figure 3.2 of Horn-von Hoegan[16])

is typically around 5°. A computer is used to raster through all of the possible angles α and azimuth ϕ so the full 2D diffraction pattern can be recorded by the channeltron one point at a time. The changing α moves the vector $\mathbf{K} = \mathbf{k_i}$ - $\mathbf{k_f}$ along the Ewald sphere as shown in Figure 2.10(c). Note that due to the fixed angle between $\mathbf{k_i}$ and $\mathbf{k_f}$ the Ewald sphere for the SPALEED is twice the size of the regular LEED and only one location $\mathbf{K}$ in reciprocal space is measured at a time by the channeltron. For a fixed azimuth ϕ, changing the angle α moves the point in reciprocal space being probed by the channeltron through a range of possible wavevectors $\mathbf{k}$ parallel to the surface for that ϕ, recording any lattice rods it moves through.

The particular octopole voltages required for a scan are generated by the computer, but there are a wide variety of user controls that can affect the image. The main influence on the data collected is the energy of the electron beam. The energy determines the wavelength of the electrons, which can change which layer is being probed and affects the intensity of the spots. The positioning controls and lens are all used to bring the diffraction pattern into focus and center the region of the diffraction pattern being studied each time the energy is changed. The first set of controls are the physical position of the sample. These are typically controlled by a manipulator flange that holds the sample. The x-axis is along the beam direction and determines how close the sample is to the entrance lens. The y-axis is at a right angle to the x-axis and parallel to the floor. The z-axis controls the vertical height of the sample. The y-

and z-axes are primarily used for centering the specular reflection on the channeltron, while the x-axis does affect the focus. A second set of physical position controls are the tilt pins on the manipulator. There are three screws arranged in a triangle that allow the z-axis to be adjusted so it is perpendicular to the electron beam. The final set of physical position controls are the rotations around the y-axis and z-axis. These are also primarily used for centering the specular on the channeltron. The next set of controls are the deflection voltages. Typically to raster through k-space the computer changes the deflection voltages to adjust the α and ϕ that the electron beam is hitting the sample, but there are knobs for manual adjustment of the initial deflection voltages. These are also used to help center the specular on the channeltron, but the majority of the centering should be done with the physical controls. Next are the lens settings. The entrance lens, E_L, is an electric field lens near the sample that has the electrons that hit the channeltron pass through it twice. The L_{13}, L_2, and Wehnelt lenses are part of the electron gun and help focus and form the initial electron beam. The remaining controls are in the SPALEED computer program. The largest factor in the quality of the scan is the total gate time, or exposure time, for each location in reciprocal space. Typically a relatively short gate time is chosen, but multiple scans are taken back-to-back and added to the previous scans, building up a large gate time. Another option is taking a 1D or 2D scan. In regular LEED every pattern is a 2D pattern, but in SPALEED in addition to taking a 2D profile by rastering across the entire reciprocal space, a single line profile can be scanned at high resolution and large gate time. The final main option is controlling the length of the scan. The actual length of the scan is in volts from the deflection voltage, but there is a calibration called sensitivity that converts the length into percent Brillouin zone (%BZ). One Brillouin zone is the length of one reciprocal space lattice, and the substrate lattice is typically used as reference. The spot locations and scan sizes are then referred to in terms of the $\%BZ_{substrate}$.

The main advantage the SPALEED has over regular LEED is the resolution to investigate individual spot shapes because of the narrow spread in energy and angular divergence of the electron gun resulting in a small spread in wavevector leading to a small transfer width and large coherence length[16].

Both techniques can determine the location of a spot which is related to the overall lattice on the surface, but the shape of the spot is affected by surface imperfections which cause deviations from the ideal 2D periodicity[13]. As the energy changes the wavelength of the electrons change resulting in a phase difference S for scattering for adjacent terraces or islands with a height difference of an integer number of atomic steps d. The equation for phase is:

$$S = \frac{2d\cos(\nu)}{\lambda_e} \tag{2.12}$$

where d is the step height, ν is the angle between the incoming plane wave and the surface normal (in Figure 2.10(b) this $\nu = \alpha + \delta/2$), and λ_e is the wavelength of the electron. The angle ν is typically small in SPALEED allowing $\cos(\nu)$ to be approximated as 1, and λ_e follows from Equation 2.2. The in-phase condition where S is an integer has electrons interfere constructively for these different heights and results in a sharp specular spot. The out-of-phase condition at half integers has destructive interference that is sensitive to surface roughness. This manifests as part of the specular spot being redistributed into diffusely scattered electrons within a few %BZ of the specular[16]. In between these two phase conditions are a continuous spectrum of superpositions of the two extremes.

Examples of features that can change the diffraction pattern spot profile include a rough surface morphology, adsorbate islands, differences in form factor, and vicinal surfaces[16]. In order to study these changes high resolution is needed. A completely ideal system and experimental setup would have a delta function for all lattice rods, but due to the electron beam having a non-zero energy spectrum width, a non-zero angular spread, and a non-infinite surface to scatter off of there are experimental contributions to the spot width. Regular LEED has a resolution of around 1%BZ to 3%BZ, but SPALEED can have a transfer width of ~3000 Ångstroms resulting in the instrumental contribution to the FWHM of the specular of $0.34\%\mathrm{BZ}_{\mathrm{Si(111)}}$ for a Si(111) surface. Some examples of modified spots due to surface structures are shown in Figure 2.11. The first column is a side view of the surface arrangement, the second column is the representation in reciprocal space with $k_{||}$ on the x-axis and energy/phase on the y-axis, and the third column is the in-phase and out-of-phase conditions for the specular. The first pattern in Figure 2.11(a) is a regularly spaced step array on the substrate. This produces a single sharp

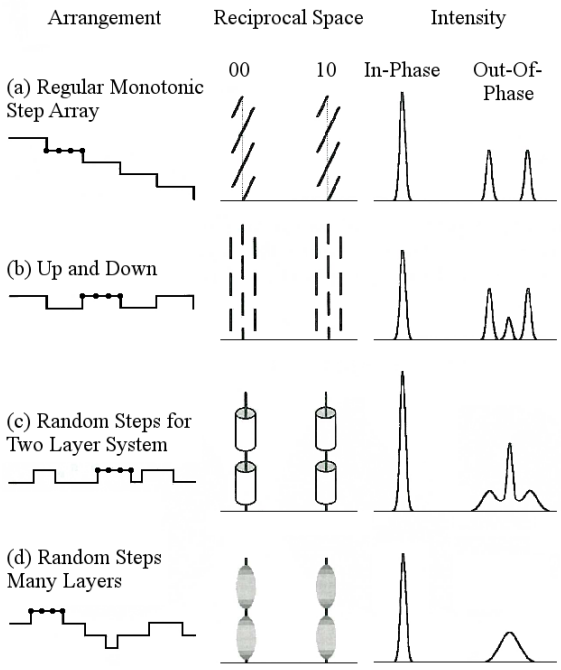

Figure 2.11 Examples of the diffraction patterns produced by surface defects. (after Figure 4.9 of Oura[13] and Figures 3 and 4 of Henzler[17])

peak at the in-phase condition, but a split spot at the out-of-phase condition. As the energy and phase change, a single spot increases in intensity and slides along k-space, passing through the (00) location at the in-phase condition, then fading away. The angle in k-space of this spot movement is related to the normal direction of the step train. Figure 2.11(b) is a regular array of up and down steps. The in-phase condition is again a single sharp spike while the out-of-phase condition has two sharp side peaks with the location related to the repeating distance. Figure 2.11(c) has two layers, but the islands are randomly spaced. If the spacing is smaller than the transfer width a Henzler ring forms around the specular in the out-of-phase condition with the radius equal to the average spacing of the islands and the width of the Henzler ring related to the average island size. For longer spacing the features cannot be resolved. The in-phase condition has a sharp specular. Figure 2.11(d) shows a system with many exposed layers. In the out-of-phase condition there is not a preferred lateral spacing so the wings from (b) and (c) are broader and overlap with the specular. The in-phase condition is again a sharp specular[13].

Low Energy Electron Diffraction has been one of the staples for surface science for decades. The energy range for a short mean free path for electrons coupled with the electron wavelength at those energies being on the same order as the interatomic spacing make it ideal for sensing periodic orderings on the surface. The SPALEED builds on the ability of regular LEED by having the resolution to investigate the shapes of the spots to collect information about the surface morphology. With the electron beam spot size on the order of 0.1 mm the surface morphology can be investigated over thousands of atomic lattices and collect much higher statistical information, especially in inhomogeneous (i.e. 2-phase systems or systems with many structures coexisting) with $\sim 10^6$ separate regions averaged.

2.5 Summary

The experimental equipment used in this thesis all complement each other to enable the study of the behavior of atoms on surfaces. The ultra high vacuum chamber allows a clean, controlled environment for sample preparation and analysis. The STM creates real space images of the surface with atomic accuracy, but is limited in taking large amounts of statistics by scan time. The SPALEED can collect information about the average behavior of large portions of the surface with single diffraction pattern, but has trouble isolating the behavior at the local level, and needs help from the STM and theory to interpret the diffraction patterns. Throughout the remainder of this thesis are examples of the research applications of these two wonderful pieces of equipment.

References

[1] Xu, Zhang, Li, and Tao, Nano Letters **4**, 1105 (2004), URL http://dx.doi.org/10.1021/nl0494295. 2.1

[2] P. Mårtensson, F. Owman, and L. Johansson, physica status solidi (b) **202**, 501 (1997), ISSN 1521-3951, URL http://dx.doi.org/10.1002/1521-3951(199707)202:1<501::AID-PSSB501>3.0.CO;2-H. 2.2

[3] L. Li and I. Tsong, Surface Science **351**, 141 (1996), ISSN 0039-6028, URL http://www.sciencedirect.com/science/article/pii/0039602895013555. 2.2

[4] M. S. Nevius, M. Conrad, F. Wang, A. Celis, M. N. Nair, A. Taleb-Ibrahimi, A. Tejeda, and E. H. Conrad, Phys. Rev. Lett. **115**, 136802 (2015), URL http://link.aps.org/doi/10.1103/PhysRevLett.115.136802. 2.2

[5] M. Conrad, F. Wang, M. Nevius, K. Jinkins, A. Celis, M. Narayanan Nair, A. Taleb-Ibrahimi, A. Tejeda, Y. Garreau, A. Vlad, et al., Nano Letters **17**, 341 (2017), URL http://dx.doi.org/10.1021/acs.nanolett.6b04196. 2.2

[6] C. Riedl, C. Coletti, and U. Starke, Journal of Physics D: Applied Physics **43**, 374009 (2010), URL http://stacks.iop.org/0022-3727/43/i=37/a=374009. 2.2

[7] T. Kimoto, A. Itoh, H. Matsunami, and T. Okano, Journal of Applied Physics **81**, 3494 (1997), URL http://dx.doi.org/10.1063/1.365048. 2.2

[8] R. Feng, E. Conrad, C. Kim, P. Miceli, and M. Tringides, Physica B: Condensed Matter **357**, 175 (2005), ISSN 0921-4526, proceedings of the 8th International Conference on Surface X-ray and Neutron Scattering, URL http://www.sciencedirect.com/science/article/pii/S092145260401172X. 2.2

[9] R. Feng, E. H. Conrad, M. C. Tringides, C. Kim, and P. F. Miceli, Applied Physics Letters **85**, 3866 (2004), URL http://dx.doi.org/10.1063/1.1812593. 2.2

[10] E. W. Müller, Zeitschrift für Physik **131**, 136 (1951), URL http://link.springer.com/article/10.1007/BF01329651. 2.3

[11] M. Bode, Reports on Progress in Physics **66**, 523 (2003), URL http://stacks.iop.org/0034-4885/66/i=4/a=203. 2.3

[12] E. Meyer, H. J. Hug, and R. Bennewitz, *Scanning probe microscopy: the lab on a tip* (Springer Science & Business Media, 2013), ISBN 9783540431800, URL http://books.google.com/books?id=v2oy14gjzwUC. 2.3

[13] K. Oura, *Surf. Sci.: an introduction*, Advanced texts in physics (Springer, 2003), ISBN 9783540005452, URL http://books.google.com/books?id=HBFtQgAACAAJ. 2.7, 2.3, 2.4.1, 2.4.1, 2.4.1, 2.4.2, 2.11, 2.4.2

[14] G. Comsa, Surface Science **81**, 57 (1979), ISSN 0039-6028, URL http://www.sciencedirect.com/science/article/pii/0039602879905053. 2.4.1

[15] N. W. Ashcroft and N. D. Mermin, *Solid State Physics* (Sanders College Publishing, 1976), ISBN 9780030839931. 2.4.1, 2.9, 2.4.1, 2.4.1, 2.4.1

[16] M. Horn-von Hoegen, Zeitschrift für Kristallographie **214**, 591 (1999). 2.10, 2.4.2, 2.4.2, 2.4.2

[17] M. Henzler, Applications of Surface Science **1112**, 450 (1982), ISSN 0378-5963, URL http://www.sciencedirect.com/science/article/pii/0378596382900927. 2.11

CHAPTER 3. NONCLASSICAL "EXPLOSIVE" NUCLEATION IN PBSI(111) AT LOW TEMPERATURES

M. T. Hershberger, M. Hupalo, P. A. Thiel, C. Z. Wang, K. M. Ho, and M. C. Tringides

A paper published in *Physical Review Letters* **113**, 236101 (2014)

Copyright 2014 by the American Physical Society.

3.1 Abstract

Classically, the onset of nucleation is defined in terms of a critical cluster of the condensed phase, which forms from the gradual aggregation of randomly diffusing adatoms. Experiments in Pb/Si(111) at low temperature have discovered a dramatically different type of nucleation, with perfect crystalline islands emerging "explosively" out of the compressed wetting layer after a critical coverage $\Theta_c = 1.22$ ML is reached. The unexpectedly high island growth rates, the directional correlations in the growth of neighboring islands and the persistence in time of where mass is added in individual islands, suggest that nucleation is a result of the highly coherent motion of the wetting layer, over mesoscopic distances.

3.2 Introduction

Nucleation is a fundamental process in nature that relates to a wide range of physical phenomena of both basic and technological importance in physical and biological sciences and engineering[1–6]. Many practical applications depend on the nucleation and growth of novel phases with unusual structural and electronic properties, relevant for catalysis and energy conversion. Nucleation involves the fine interplay between equilibrium and non-equilibrium physics, so it also relates to fundamental questions in statistical mechanics[7–12]. Although a

complete understanding of nucleation has not yet been attained, the widely used paradigm is based on the model of classical nucleation. The main concept of the model is the existence of a critical size cluster r_c, which defines the minimum cluster size, such that clusters larger than r_c are stable and do not dissociate. The mass needed for the clusters of the condensed phase to grow is provided by diffusing adatoms within the initial homogeneous dilute phase. This analysis has been applied universally for a wide range of physical systems and especially to the epitaxial growth of ultrathin films[13–15].

In particular, island nucleation is observed in strained systems, a result of a morphological 2D-to-3D transition commonly referred to as the Stranski-Krastanov (SK) growth mode. The competition between strain energy (due to the lattice mismatch between overlayer and substrate) vs. the surface energy drives the transition. Depending on the lattice mismatch between the substrate and the film different pathways are possible for the 3D transition. For small ϵ, 3D islands nucleate above a critical thickness h_c with misfit dislocations decorating the interface, but for larger ϵ, roughening of the film is possible at much lower film thickness than h_c[16]. For Pb/Si(111) no roughening is observed. These predictions have been fully confirmed in the prototype system $Si_{1-x}Ge_x$ since ϵ can be varied extensively as a function of stoichoimetry[16].

In all SK systems mass transport is through normal random walk diffusion. The detailed study of SK growth at lower temperatures and the role different non-thermodynamic factors can play are not fully explored. Pb/Si(111) follows a similar 2D-to-3D transition and strain is also a key factor (because of the 11% lattice mismatch between Si(111) and Pb(111) as in typical SK systems), but the transition occurs at ∼150-250 K. In this work we show that a novel and faster type of nucleation dramatically different from classical nucleation is present. The novel nucleation is not driven by thermodynamic factors but by a very unusual type of mass transport. Pb(111) islands are not built gradually from the sequential aggregation of Pb adatoms; on the contrary, the deposited Pb adatoms are continually consumed by the wetting layer, which fully covers the substrate. After the wetting layer reaches a critical value $\Theta_c \approx 1.22$ ML [22% larger than the metallic Pb(111) density] nucleation is very abrupt, with multiheight, crystalline, fully completed islands, with at least $\sim 10^5$ atoms each, emerging from the compressed wetting

layer. More importantly, mass transport is not the result of classical random-walk diffusion, but involves the collective motion of millions of atoms over mesoscopic scales. This striking result is deduced from the exceedingly high island growth rate when compared to the classical rate, from directional correlations in the growth of neighboring islands and from temporal correlations in the growth direction of individual islands. For Pb/Si(111) the temperature range these unusual phenomena are observed is centered at $\sim 0.3T_m$, with T_m the Pb melting temperature. Potentially such nucleation phenomena are more universal and not exclusive to Pb/Si(111) if the corresponding temperature "window" is scaled with T_m.

3.3 Results

Experiments are presented here for Pb growth on the Si(111)-7x7 substrate, and similar data have been obtained for growth on the α–$\sqrt{3}$ x $\sqrt{3}$ Pb/Si(111) phase. Typical results are shown in Figure 3.1 and Figure 3.2. After an initial deposition of 0.82 ML at 200 K, Pb is deposited in smaller stepwise increments of $\Delta\Theta \sim 0.045$ ML (to approach Θ_c with a finer coverage control) and after each deposition, scans of large overlapping areas (their overlap identified by features on the steps) are taken to monitor nucleation changes. Nine images (the first eight are 500 x 500 nm^2 and the ninth 1500 x 1500 nm^2) acquired consecutively are shown in Figure 3.1(a-i) and no islands are seen [except two small islands nucleated at the step in Figure 3.1(i)].

Figure 3.2 shows the result of one more 0.045 ML deposition in the area of Figure 3.1(i). One normally expects to observe the nucleation of small one-layer islands which subsequently grow both in size and height. Because the nucleation and the growth are stochastic processes, the islands are expected to exhibit a wide size distribution that includes a large fraction of small islands. This is not what is observed. Large multiheight (of 4 to 7 layers instead of 1 layer islands) perfect crystalline Pb islands, all above a minimum radius of ~15 nm, emerge. The island density is very low at 1.65 x 10^{-5} islands/nm^2. The ratio $k = (\Delta\Theta_{\text{island}})/\Delta\Theta$ of the Pb amount in the islands over the last amount deposited is 2.2, but in other experiments depending on the temperature T, or flux, or how close $\Delta\Theta$ approaches Θ_c, k can be much

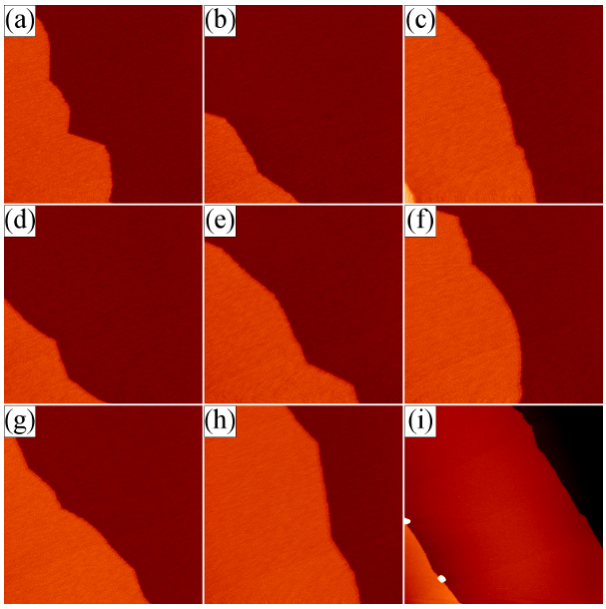

Figure 3.1 Pb wetting layer evolution on Si(111)-7x7 with Pb deposition at T = 200 K (a) 500 x 500 nm^2 $\Theta = 0.82$ ML. (b-h) 500 x 500 nm^2 areas after stepwise depositions of $\Delta\Theta \sim 0.045$ ML. (i) $\Theta = 1.17$ ML but the image area is larger, 1500 x 1500 nm^2.

higher. This indicates that the nucleation of the Pb islands is completed within the last short deposition in a very "explosive" way.

Although the STM is not the ideal instrument to study kinetics because of the finite acquisition time, which is typically ~tens of seconds depending on the scan size, one can safely conclude that the nucleation time is less than the STM acquisition time. This is seen from islands encountered earlier in the scan of any size having the same dimensions as islands encountered later in the scan; for fixed temperature the average island size is independent of scan size; under all scanning conditions only completed islands are observed both in the current experiments and in numerous previous experiments carried out by us using both STM and SPA-LEED to study quantum size effects[17]. This conclusion is also very consistent with earlier diffraction experiments with RHEED[18], x-ray[19] and with all three techniques RHEED, x-ray, and He scattering[20] that have shown a steplike intensity increase of the Pb(10) spot, during deposition, after the completion of the wetting layer. From the known flux rates in these

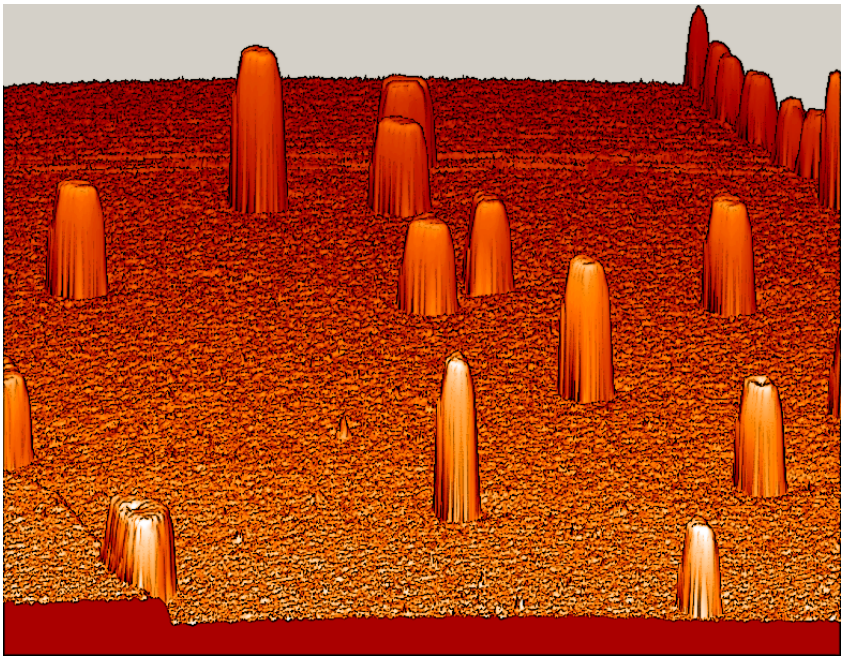

Figure 3.2 1000 x 1000 nm^2 Pb on Si(111)-7x7 with several multiheight islands forming at Θ = 1.22 ML by adding $\Delta\Theta \sim 0.045$ ML on the surface of Figure 3.1(i). The islands form explosively.

diffraction experiments F $\sim$ 0.9 ML/min the island nucleation times are extracted to be a few seconds.

In several references[18–20] the authors have speculated that high diffusion must be present despite the low temperatures, but its puzzling character was assumed to be still classical. The character of the required mass transport responsible for the explosive nucleation has been identified with further STM experiments shown in Figure 3.3(a,b). The temperature is 200 K and in Figure 3.3(a) the coverage is Θ = 1.22 ML; the surface after 3 smaller depositions totaling 0.09 ML is shown in Figure 3.3(b). Both imaged areas of Figure 3.3 are very large, 1500 x 1500 nm^2, so mass transport can be checked over mesoscopic distances. Features along the step (i.e., inward kink bottom left) are used to match the y scales in the two images and correct for minor nonlinearities of the piezo gain. Figure 3.3(c) shows the difference between the overlapping areas of Figure 3.3(a,b) so the growth direction for each island can be determined [blue marks the islands in Figure 3.3(a) and orange the ones in Figure 3.3(b)].

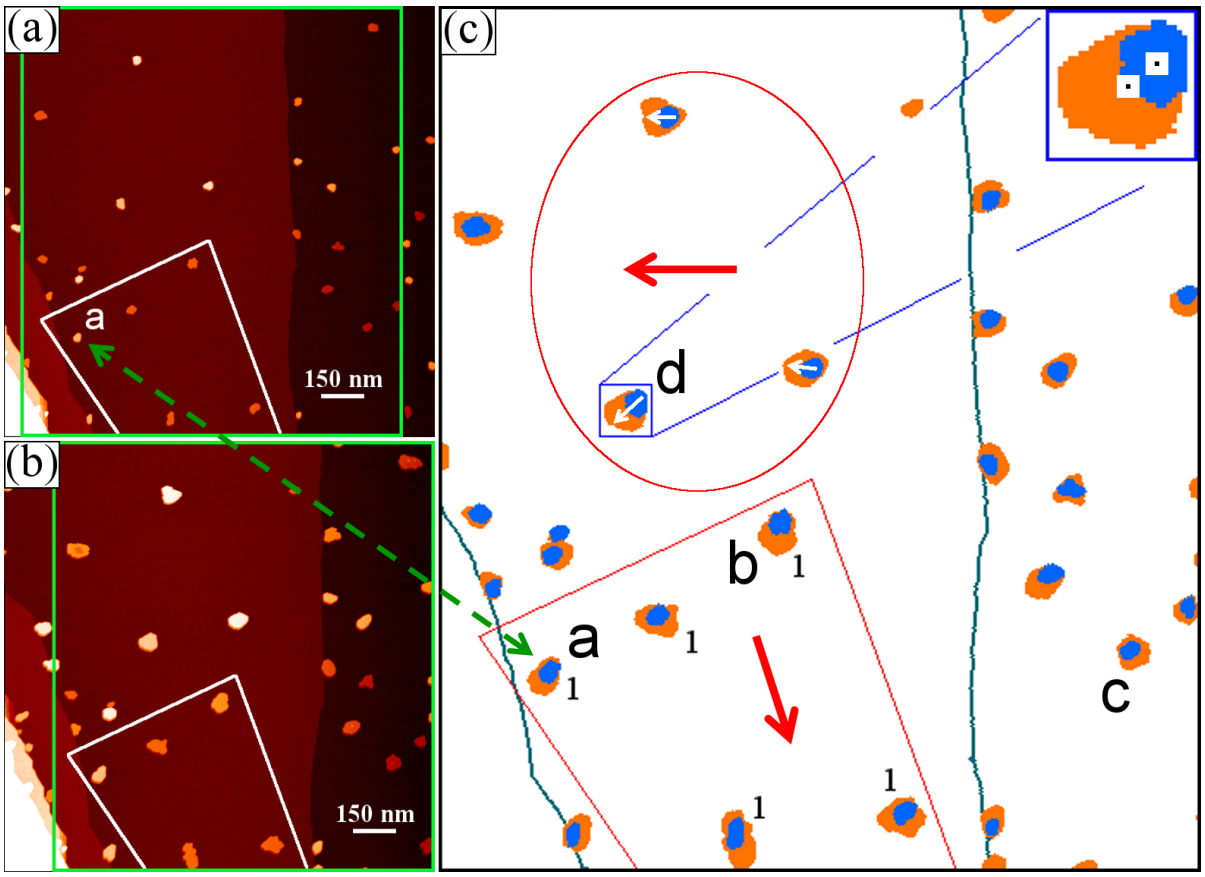

Figure 3.3 Different deposition experiment on Pb/Si(111)-7x7 at 200 K with 1500 1500 nm^2 areas imaged sequentially (a) $\Theta = 1.22$ ML. (b) After $\Delta\Theta = 0.09$ ML is added on (a). (c) Overlapping 1320 x 1500 nm^2 sections of (a) and (b) shown in green. In (c) blue shows the areas of the islands in (a) and orange the islands in (b). Inset shows typical large c.m. shift. White arrows indicate islands that paradoxically are growing in the direction of lower adatom influx (if diffusion was classical). The black 1's identify five islands within area A outlined in red in (c) growing in a similar direction indicating correlated transfer of material from the wetting layer to the islands. The same area is shown in white in (a) and (b).

In classical nucleation, islands are expected to grow isotropically since the randomly diffusing adatoms on average arrive with equal probability from all directions[13–15]. The center of mass (c.m.) of the growing islands is expected to remain unchanged. This is not the case for most of the islands in Figure 3.3(c) (with the inset showing a blowup for one of the islands). The islands must be collecting material predominantly from the same direction, since the c.m. is shifted by large distances, comparable to the initial island radius ∼20 nm. The comparison indicates that the amount collected by the islands is not incorporated randomly but in preferred directions and therefore must originate in a correlated and persistent way from far away. A different surprising result not consistent with classical nucleation is that although the islands marked with arrows face a large vacant area, (which should be more populated with high density of adatoms), the island growth is paradoxically from almost the opposite island side.

In addition to the preferential directional growth of individual islands, neighboring islands show also correlations in their growth direction [for example, the five islands marked with 1 within the area A outlined in red in Figure 3.3(c) and in white in Figure 3.3(a,b)]. This further supports that the wetting layer must be moving in a correlated way over large distances. The growth of neighboring islands can be used to estimate the distance l_0 over which the material arrives, by checking mass balance, with the main assumption that the amount added to the islands must equal the Pb amount increase within the surrounding area, after the small deposition $\Delta\Theta$. Based on nucleation theory, the latter is the amount collected within the Voronoi area around a given island. Using, for example, the top left island of the five islands, its area increases from 1035 to 2151 nm^2, and it is six layers tall so 7 x 10^4 Pb atoms are needed for its growth. Its Voronoi area is 4.3 x 10^4 nm^2 and has only collected 9.6 x 10^3 atoms after the 0.022 ML deposition. This gives a ratio ∼7 of the number of adatoms added to the available ones (if growth was isotropic), but since growth is directional the ratio is even higher, 14. This large difference indicates that material that was incorporated in the island must originate well outside its Voronoi area.

An average estimate that includes the growth of all the five islands within the outlined area A (of width $w \approx 0.4\mu m$ and length $s \approx 0.6\mu m$) gives a quantitative estimate of l_0. The islands

cover $a \approx 0.03$ A of A and the needed mass is proportional to the number of islands $n = 5$, their average height $h = 4.6$, and the measured average area increase $\Delta a \approx 1.3a$. The supply to the outlined area A is through the narrow side normal to the growth direction and given by $wl_0\Delta\Theta$. Using $\Delta\Theta = 0.022$ ML (i.e., the increase shown next in red in Figure 3.4) $s \approx 0.6\mu m$, and $l_0 = (1.3)(0.03)(hs)/\Delta\Theta$ gives 5 μm, more than 3 times the imaged area.

This simple calculation is only approximate and underestimates l_0 since it was assumed that no other islands are present in the supply area that feeds A. Because other islands must be present, which will be encountered by the moving wetting layer and compete for Pb, l_0 must be larger than 5 μm. Such diffusion distances are very consistent with the typical distances the wetting layer moves in step profile evolution experiments[21]. They are at least ∼50 times larger than $\sim$ 0.2 μm the diffusion length from the observed island density, if diffusion was classical and the scaling theory of nucleation is used.

Besides the spatial correlations in the growth of neighboring islands, there are also time correlations in the growth of single islands, which further confirm the non-stochastic motion of the wetting layer from far away. Analysis is shown in Figure 3.4 where 4 islands within the area of Figure 3.3(c) [marked by letters a, b, c, d] are analyzed to estimate their growth after six incremental depositions. The different colors correspond to amounts 1.220, 1.242 ML (used previously to estimate l_0), 1.270, 1.310 ML [corresponds to Figure 3.3(b)], 1.400, 1.490, 1.760 ML. [The island edges for the times shown in Figure 3.3(a,b) are highlighted in white.] The insets show the positions of the c.m. after each deposition, and not only is there a large shift, but the evolution of the c.m. is almost ballistic. Over the long time of the experiment (∼6 h) preferred directions in the island growth are sustained; this is incompatible with random walk diffusion. Islands a and c grow in SW, island b in S and island d in W directions. This indicates a "memory" effect of the way material is transferred from the wetting layer to the islands and coherent motion, extending to tens of μms and over hours.

3.4 Discussion

The nucleation experiments reported in this study have extended earlier work[21–26] on Pb/Si(111) with several techniques showing a very unusual type of diffusion, but none of these

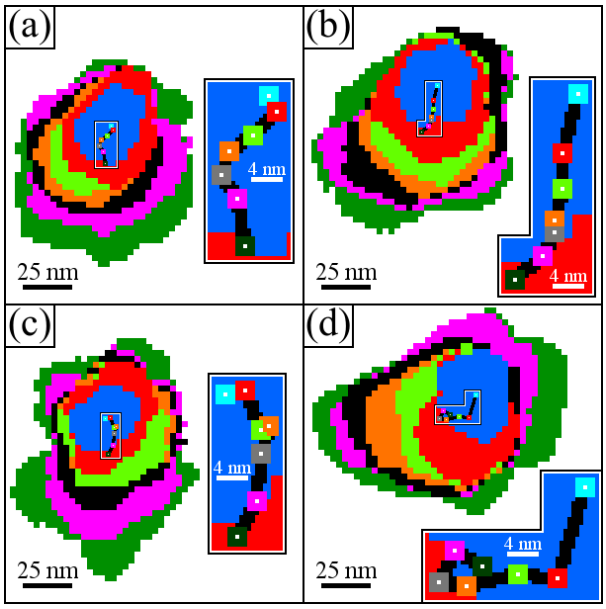

Figure 3.4 The growth of four typical islands marked by letters a, b, c, and d in Figure 3.3(c) after 6 $\Delta\Theta$ stepwise depositions with 150 x 150 nm^2 areas and coverages 1.220 ML [blue in Figure 3.3(c)], 1.242, 1.270, 1.310 ML [orange in Figure 3.3(c)], 1.400, 1.490, 1.760 ML. The edges of the four islands are highlighted in white for the times corresponding to Figure 3.3(a,b). Island a in Figure 3.3(c) is also identified in Figure 3.3(a) by the dashed green line. For most $\Delta\Theta$ depositions the same direction of growth is sustained and the c.m. positions seen in the insets evolve ballistically. These temporal correlations provide further evidence for the collective motion of the wetting layer.

earlier experiments have examined the explosive nucleation. The first non-classical fast mass transport observation was made in coarsening experiments, well after nucleation, with surface x-ray scattering. A mixture of islands was initially present with both unstable and stable heights, island stability defined by QSE[22,23]. The decay of the unstable islands was faster by orders of magnitude than what is expected from the known Pb(111) adatom detachment barrier. A more recent experiment with LEEM has shown an even more intriguing result about the wetting layer mobility itself. The refilling of a circular vacant area (a standard profile evolution experiment to measure surface diffusion) was monitored in time over large distances $\sim$0.1 mm[21]. It was found that the refilling not only is superdiffusive, $x \sim t$ (instead of random walk type diffusion $x \sim t^{1/2}$), the refilling profile shows two oppositely moving fronts with the mass generated at the outward front being the mass arriving at the inward refilling one. In a different experiment after C_{60} deposition on the α–$\sqrt{3}$ x $\sqrt{3}$ Pb/Si(111) phase, extremely fast transformations were seen, even at 20 K, between different "devil's staircase" (DS) phases as Pb adatoms are "kicked out"[24]. The change between the two DS phases shows fast and error free pattern formation at such low temperatures. A mesoscopic scale refaceting transition observed on a dense DS phase of Pb on the stepped Si(557) surface has unusually high speed at 80 K[25] analogous to the high mass transport observed in the current experiments. Collective diffusion has also been seen in Pb/Ni(111)[26] with similar exceedingly fast motion of the wetting layer when metastable Pb islands decay to their equilibrium shapes. Theoretical work has been carried out to address the question of superdiffusive motion in 2D overlayers but there is still no complete understanding as to its origin[27–30].

3.5 Conclusion

In conclusion, the current experiments have shown a novel type of nucleation not expected classically. Once a critical coverage of the Pb/Si wetting layer is reached, $\Theta_c = 1.22$ ML, perfect Pb(111) crystalline multiheight islands emerge explosively. The formation of the islands is very abrupt, despite the low temperatures, and the time of the explosion is less than the STM acquisition time and can be estimated to be a few seconds. Mass transport from the wetting layer to the islands is not via random walk diffusion as in classical nucleation, but through

the collective motion of the wetting layer, deduced from the very high transport rate and the strong spatial and temporal correlations in the island growth directions. It is an open problem to search for other systems where this unusual type of nucleation might be present.

3.6 Acknowledgements

This work was supported by the Office of Science, Basic Energy Sciences, Materials Sciences and Engineering Division of the U.S. Department of Energy (U.S. DOE), under Contract No. DE-AC02-07CH11358 with the U.S. Department of Energy.

References

[1] F. Abraham, *Homogeneous nucleation theory: the pretransition theory of vapor condensation*, vol. 1 (Academic Press, 1974), ISBN 9780120383610, URL http://www.sciencedirect.com/science/book/9780120383610. 3.2

[2] W. Kurz and D. J. Fisher, *Fundamentals of Solidification* (Trans Tech Publications, 1998), 4th ed., ISBN 9780878495221.

[3] J. W. P. Schmelzer, ed., *Nucleation Theory and Applications* (Wiley-VCH, 2005), ISBN 9783527404698, URL http://onlinelibrary.wiley.com/book/10.1002/3527604790.

[4] J. J. De Yoreo and P. G. Vekilov, Reviews in mineralogy and geochemistry **54**, 57 (2003), URL http://rimg.geoscienceworld.org/content/54/1/57.short.

[5] L. Ratke and P. W. Voorhees, *Growth and coarsening: Ostwald ripening in material processing* (Springer, 2002).

[6] M. Nishino, C. Enachescu, S. Miyashita, P. A. Rikvold, K. Boukheddaden, and F. Varret, Scientific reports **1**, 162 (2011), URL https://www.ncbi.nlm.nih.gov/pmc/articles/PMC3240980/. 3.2

[7] R. Plass, J. A. Last, N. Bartelt, and G. Kellogg, Nature **412**, 875 (2001), URL http://www.nature.com/nature/journal/v412/n6850/abs/412875a0.html. 3.2

[8] Y. Sato, S. Chiang, and N. C. Bartelt, Phys. Rev. Lett. **99**, 096103 (2007), URL http://link.aps.org/doi/10.1103/PhysRevLett.99.096103.

[9] J. de la Figuera, F. Léonard, N. C. Bartelt, R. Stumpf, and K. F. McCarty, Phys. Rev. Lett. **100**, 186102 (2008), URL http://link.aps.org/doi/10.1103/PhysRevLett.100.186102.

[10] T. O. Menteş, A. Locatelli, L. Aballe, and E. Bauer, Phys. Rev. Lett. **101**, 085701 (2008), URL http://link.aps.org/doi/10.1103/PhysRevLett.101.085701.

[11] N. H. P. Nguyen, D. Klotsa, M. Engel, and S. C. Glotzer, Phys. Rev. Lett. **112**, 075701 (2014), URL http://link.aps.org/doi/10.1103/PhysRevLett.112.075701.

[12] H. J. Zhao, V. R. Misko, and F. M. Peeters, New Journal of Physics **14**, 063032 (2012), URL http://stacks.iop.org/1367-2630/14/i=6/a=063032. 3.2

[13] J. A. Venables, G. D. T. Spiller, and M. Hanbucken, Reports on Progress in Physics **47**, 399 (1984), URL http://stacks.iop.org/0034-4885/47/i=4/a=002. 3.2, 3.3

[14] H. Brune, Surface Science Reports **31**, 125 (1998), ISSN 0167-5729, URL http://www.sciencedirect.com/science/article/pii/S0167572999800016.

[15] J. Evans, P. Thiel, and M. Bartelt, Surface Science Reports **61**, 1 (2006), ISSN 0167-5729, URL http://www.sciencedirect.com/science/article/pii/S0167572906000021. 3.2, 3.3

[16] J. Tersoff and F. K. LeGoues, Phys. Rev. Lett. **72**, 3570 (1994), URL http://link.aps.org/doi/10.1103/PhysRevLett.72.3570. 3.2

[17] M. C. Tringides, M. Jałochowski, and E. Bauer, Physics Today **60**, 50 (2007). 3.3

[18] R. Feng, E. Conrad, C. Kim, P. Miceli, and M. Tringides, Physica B: Condensed Matter **357**, 175 (2005), ISSN 0921-4526, proceedings of the 8th International Conference on Surface X-ray and Neutron Scattering, URL http://www.sciencedirect.com/science/article/pii/S092145260401172X. 3.3

[19] M. Jałochowski and E. Bauer, Journal of Applied Physics **63**, 4501 (1988), URL http://dx.doi.org/10.1063/1.340145. 3.3

[20] D. Schmicker, T. Hibma, K. A. Edwards, P. B. Howes, J. E. MacDonald, M. A. James, M. Breeman, and G. T. Barkema, Journal of Physics: Condensed Matter **9**, 969 (1997), URL http://stacks.iop.org/0953-8984/9/i=5/a=004. 3.3

[21] K. L. Man, M. C. Tringides, M. M. T. Loy, and M. S. Altman, Phys. Rev. Lett. **110**, 036104 (2013), URL http://link.aps.org/doi/10.1103/PhysRevLett.110.036104. 3.3, 3.4

[22] C. A. Jeffrey, E. H. Conrad, R. Feng, M. Hupalo, C. Kim, P. J. Ryan, P. F. Miceli, and M. C. Tringides, Phys. Rev. Lett. **96**, 106105 (2006), URL http://link.aps.org/doi/10.1103/PhysRevLett.96.106105. 3.4

[23] M. Hupalo and M. C. Tringides, Phys. Rev. B **75**, 235443 (2007), URL http://link.aps.org/doi/10.1103/PhysRevB.75.235443. 3.4

[24] A. V. Matetskiy, L. V. Bondarenko, D. V. Gruznev, A. V. Zotov, A. A. Saranin, and M. C. Tringides, Journal of Physics: Condensed Matter **25**, 395006 (2013), URL http://stacks.iop.org/0953-8984/25/i=39/a=395006. 3.4

[25] M. Czubanowski, A. Schuster, H. Pfnür, and C. Tegenkamp, Phys. Rev. B **77**, 174108 (2008), URL http://link.aps.org/doi/10.1103/PhysRevB.77.174108. 3.4

[26] T. R. J. Bollmann, R. van Gastel, H. J. W. Zandvliet, and B. Poelsema, Phys. Rev. Lett. **107**, 136103 (2011), URL http://link.aps.org/doi/10.1103/PhysRevLett.107.136103. 3.4

[27] O. U. Uche, D. Perez, A. F. Voter, and J. C. Hamilton, Phys. Rev. Lett. **103**, 046101 (2009), URL http://link.aps.org/doi/10.1103/PhysRevLett.103.046101. 3.4

[28] J. D. Howe, P. Bhopale, Y. Tiwary, and K. A. Fichthorn, Phys. Rev. B **81**, 121410 (2010), URL http://link.aps.org/doi/10.1103/PhysRevB.81.121410.

[29] L. Huang, C. Z. Wang, M. Z. Li, and K. M. Ho, Phys. Rev. Lett. **108**, 026101 (2012), URL http://link.aps.org/doi/10.1103/PhysRevLett.108.026101.

[30] E. Granato, S. C. Ying, K. R. Elder, and T. Ala-Nissila, Phys. Rev. Lett. **111**, 126102 (2013), URL http://link.aps.org/doi/10.1103/PhysRevLett.111.126102. 3.4

CHAPTER 4. COMPARISON OF CLASSICAL NUCLEATION THEORY TO PB/SI(111)-7X7

4.1 Abstract

Using Scanning Tunneling Microscopy, Pb grown on Si(111)-(7x7) has been studied and compared to classical theory. Pb initially forms a wetting layer covering the Si(111)-(7x7) surface then when a critical coverage is reached islands quickly develop. Scaling theory predicts the distribution of island sizes will be approximately Gaussian with a single peak and be continuous down to zero area due to newly nucleated islands for critical island size $i = 1$. Immediately after island formation, the Pb/Si(111)-(7x7) distribution of island sizes has a large gap at zero size, which in classical theory signifies either all islands formed at the same time with no recent island formation or the critical island size is large. Classical scaling theory predicts that the number of atoms in an island is correlated with the area of the island's Voronoi Cell or Capture Zone. Deposited atoms that land in an island's Voronoi Cell are most likely to join that island, resulting in islands with larger Voronoi Cells gaining more atoms and growing larger. For four and five layer tall islands there is a linear relationship between Voronoi Cell area and island volume with R^2 values of 0.79 and 0.86 respectively, but the x-intercept is non-zero. Six and seven layer islands had a poor relationship between Voronoi Cell area and island volume with $R^2 \sim 0.2$ for both. While observing the wetting layer with high resolution STM images, stepwise depositions show the Si(111)-(7x7) pattern disappearing then re-emerging as the total deposition amount approaches the critical coverage for island formation. Continued depositions after island formation show anisotropies in island growth at the mesoscale, suggesting the wetting layer has directional diffusion. The reason for the non-zero x-intercept and poor correlation for Voronoi Cell area and island volume is likely related

to a portion of the atoms joining the islands coming from the Pb wetting layer and highly anisotropic island growth. The basic assumptions of classical nucleation do not apply to this system and is the source of the differences between classical theory and observations.

4.2 Introduction

The Pb on Si system was predicted to be an ideal system for studying metals on semiconductors due to the mutual bulk insolubility of Pb and Si[1]. This prediction has held true over the past two decades with numerous studies on the phases[1–6] as well as many novel properties including uniform height islands due to quantum size effects[7], discrete quantum well binding energies[8], Devil's Staircase[9], uniform width nanowires[10], non-classical coarsening[11], and linear velocity collective superdiffusion[12]. As technology continues to push towards controlled self-assembly the physics learned from the Pb/Si system is sure to be on the forefront of application, however there are still regimes of the Pb/Si phase diagram that are disputed or unstudied. This paper is part of a series of papers (Hershberger et al.[13], Chapter 5) that identify the low temperature transition from wetting layer growth to island growth for Pb/Si(111)-7x7, and this paper focuses on the deviations from classical nucleation and scaling theory.

With the widespread use of both Scanning Tunneling Microscopy (STM) and Low Energy Electron Diffraction (LEED) through the 90's, patterns in sub- to few-monolayer growth appeared. The number density of clusters of atoms, or islands, in particular was found to follow equations derivable from differential equations of basic atomistic processes. One of the key numbers for determining the island density is the critical island size, i, where $i + 1$ atoms form a stable island. In the low coverage transient regime the local adatom density increases until enough atoms aggregate for the minimum stable island size of $i + 1$ atoms. This leads to islands forming at different separations depending on diffusion. Each island has a depletion zone due to the local atoms forming the island, and this depletion zone expands radially outward with time. As more islands form the depletion zones begin to overlap leading to capture zones for the islands. When the entire surface is covered with capture zones the surface switches to the steady state regime. While the majority of atoms that are deposited in the steady state regime aggregate to the island whose capture zone they land in, there can still be significant

new island formation especially for systems where $i = 1$ and island nucleation is irreversible[14]. The resulting trend is for the island size to scale closely with the size of the capture zone. The model for classical nucleation with island density increasing continuously through the transient regime, islands forming during the steady state regime, and islands scaling with capture zone is in stark contrast to the observed behavior of the Pb/Si(111) system where there are zero islands until a critical coverage is reached, after which many islands simultaneously form[13].

The reason for this difference lies with the basic assumptions for classical nucleation. First, classical nucleation assumes the atoms on the surface are monomers. In Pb/Si(111) the surface is covered by a wetting layer so there is a large number of Pb atoms already deposited on the surface. Second, classical nucleation assumes these atoms go through a random walk on the surface with the number of hops completed based on the hopping attempt rate, the terrace diffusion energy barrier, and the temperature. The Pb/Si(111) system has been shown to have mesoscale collective, directed diffusion up to 0.1 mm[12]. Third, stable islands must reach a critical island size in number of atoms in classical nucleation. It is unclear how this translates to the Pb/Si(111) system due to numerous atoms being present in the wetting layer and both experiment[13,15] and theory[16,17] suggesting wetting layer compression is key to the diffusion of the wetting layer. Fourth, in classical nucleation for critical island sizes larger than $i = 1$ there is a cohesive energy between the atoms. This is again complicated by both the presence of the Pb/Si(111) wetting layer and the larger energetic driving factor for heights in this system: quantum size effects.

With the differences between the basic assumptions of the classical nucleation model and actual features of the Pb/Si(111) it would be surprising if classical nucleation was applicable. In this chapter we compare experimental results for the island size distributions and island scaling to classical nucleation, then move into discussion of the wetting layer structure and expand on previous research on the directional diffusion in the system.

4.3 Results and discussion

Figure 4.1 shows two different experiments of Pb grown on Si(111)-(7x7). The heights in Pb(111) layers are labeled in green for a few selected islands. Both experiments have two main

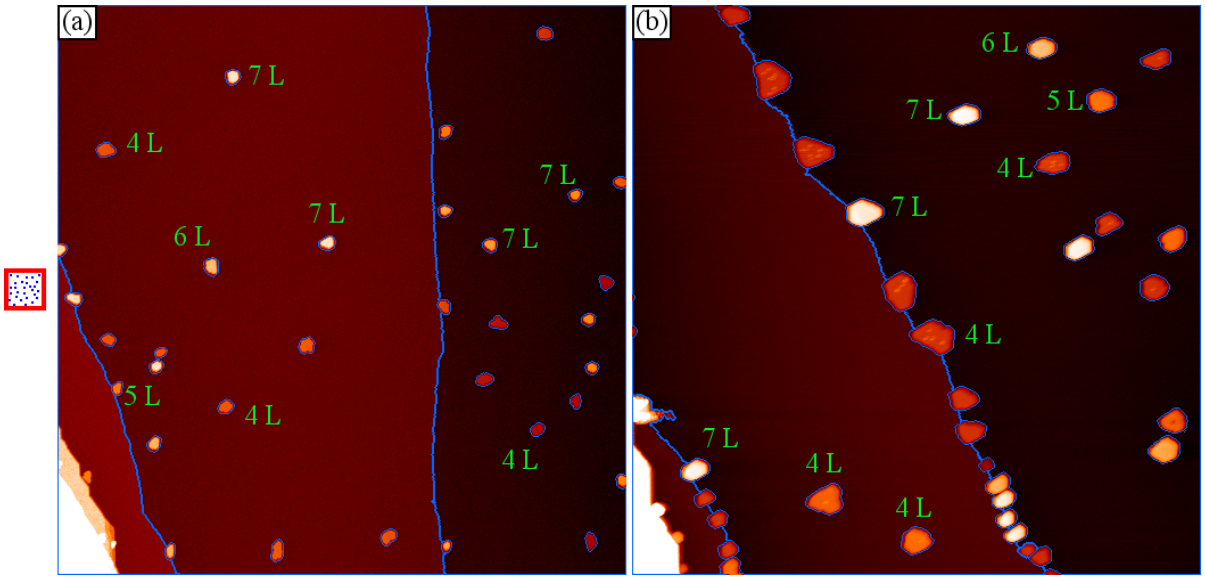

Figure 4.1 Two 1500 x 1500 nm^2 experiments where islands formed at 200 K. (a) was taken immediately after island formation at 1.22 ML. For (b) islands formed at 1.22 ML at 200 K, then an additional deposition to 1.27 ML was made at 180 K before the image was taken. The red box to the left of Figure 4.1(a) shows the size of scans with blue dots representing the area of 1 layer islands studied in typical nucleation experiments.

terraces with a single Si(111) step between them and a Si(111) step bunch raising over 30 Si(111) layers in the lower left hand corner. Both images are 1500 x 1500 nm^2. The red box to the left of Figure 4.1(a) shows the size of scans with schematic blue dots representing the area of 1 layer islands studied in typical nucleation experiments. The islands in our experiments are almost as large as the scans for typical nucleation experiments. The first experiment shown in Figure 4.1(a) had an initial deposition of 0.72 ML at 200 K, followed by 11 depositions of 0.045 ML for a total of 1.22 ML. All of the islands formed on the 11$^{\text{th}}$ deposition; the wetting layer was still island-less after the 10$^{\text{th}}$ deposition. Most of the islands formed in the middle of terraces, although some islands formed along step edges. We want to emphasize the scale of this image: 1500 x 1500 nm^2 with the central terrace starting at 700 nm wide at the bottom of the image and extending to over 1 μm as it veers off the left side of the image. The average island separation is 290 nm and the island density is 1.5 x 10^{-5} islands/nm^2.

Figure 4.2(a-c) shows the Figure 4.1(a) island's heights, areas, and volumes respectively as histograms with black bars in Figure 4.2(a) and red dots with a black line interpolation in Figure 4.2(b, c). The green line in Figure 4.2(a) shows the expected classical prediction for the height distribution. As shown in Figure 4.2(a) there were **zero** 1-, 2-, or 3-layer islands. (Out of thousands of images and tens of thousands of islands for the Pb-Si(111) system our group has never seen a 1- or 2- layer Pb island on Si(111)-7x7.) The distribution of heights is peaked at four layers and seven layers with few five or six layer islands. This has been reported before in the literature[11] and is due to quantum size effects, but is in contrast to classical predictions due to no 1-, 2-, or 3-layer islands, and the islands present have neither a Gaussian nor gamma distribution. Classical theory predicts that when islands first start nucleating–as the islands shown just did with the 11^{th} deposition–they will be mostly 1-layer tall with a few 2-layer tall islands present in a single peaked distribution and will mostly be small clusters of atoms.

Examples of scaled size distributions for $i = 1$ (light green) and $i = 6$ (dark green) from Li and Evans[18] are included in Figure 4.2(b, c, e, f) with the intensity normalized by performing a Simpson's rule integration on the data. For small critical island sizes, classical theory predicts that the area distribution will be non-zero down to zero area due to new islands nucleating even into the steady-state regime. While the small sample size of n = 33 does not allow for discussion of the shape of the distribution, the spread of the peak of the area distribution in Figure 4.2(b) is clearly shifted and narrowed from the expected classical $i = 1$ distribution. This peak would be characteristic of a classical system with i close to 6. The histograms are statistically noisy because of the very small number of islands, but the size of the very first islands is clearly too large for what has been seen before. Such large critical island sizes are possible for Pb. Nucleation experiments have shown that the critical island size for Pb atoms on top of five layer tall Pb(111) mesas can be $i = 10$ at 40 K due to quantum size effects[19]. The main point is the island area distributions indicate a large critical island size, and large critical island sizes are possible for Pb/Pb interactions, but the base assumptions of classical nucleation do not apply, so the classical model should not be applied without understanding the role of the Pb wetting layer in nucleation. This includes whether Pb atoms can act like monomers in a system where the atoms in the wetting layer are not locked in place like a Pb(111) crystal

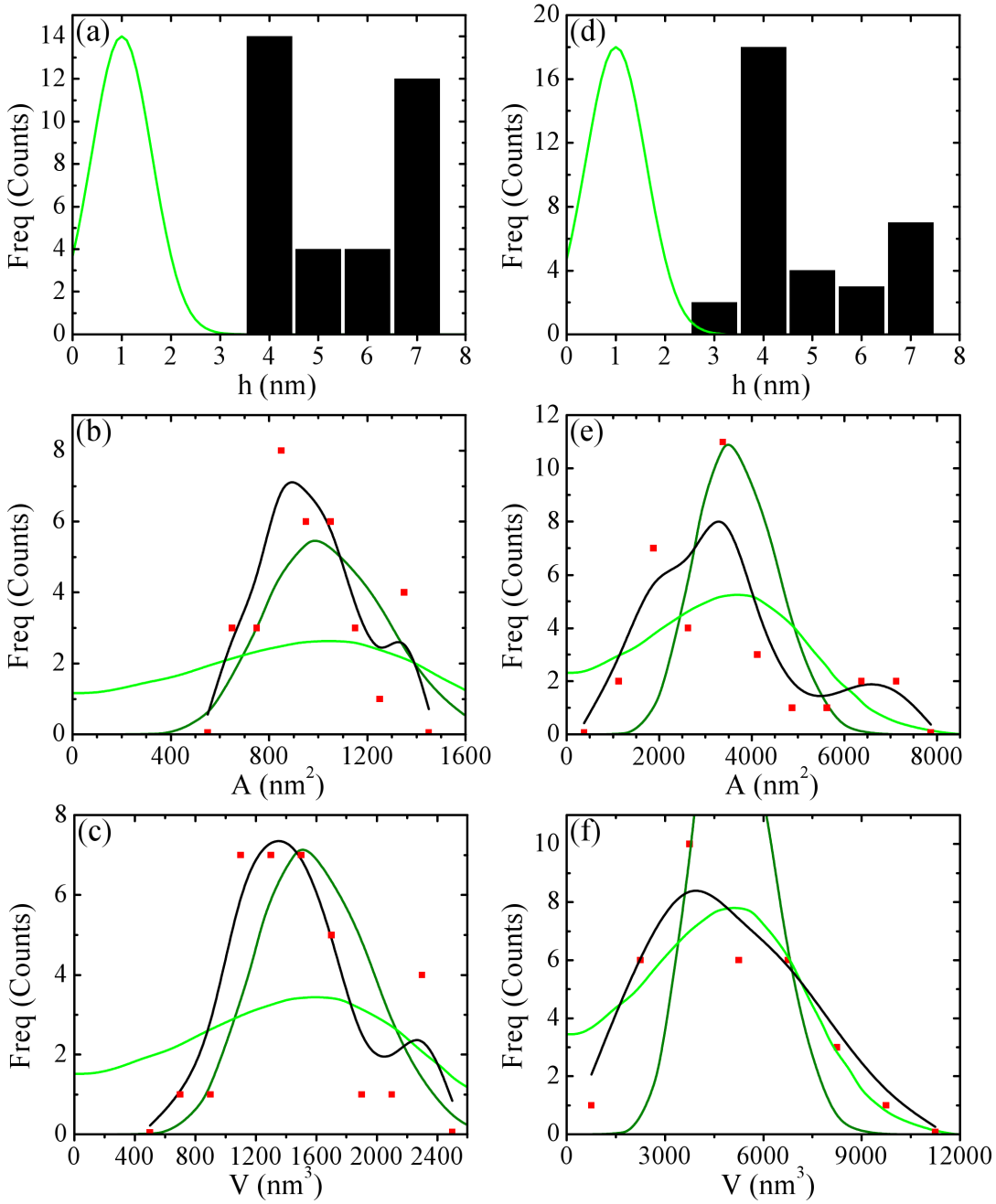

Figure 4.2 (a-c) and (d-f) are the heights, areas, and volumes for Figure 4.1(a,b). In (a, d) the green line represents the expected classical distribution of heights while the black bars are the experimental distributions. (b, c, e, f) have data points as red dots with a black line for interpolation. The light green line is the classical distribution rescaled to the data for $i = 1$ and the dark green line is for $i = 6$.

and can facilitate long distance mass transfer[12]. Figure 4.2(c) is an extrapolation of the height and area with the same seemingly large critical island size results.

The second experiment shown in Figure 4.1(b) had an initial deposition of 0.81 ML at 200 K followed by 9 depositions of 0.045 ML for a total of 1.22 ML. The sample was then cooled down to 180 K and one more deposition was added to a total of 1.27 ML before taking the scan. Figure 4.1(b) is also 1500 x 1500 nm^2 with terraces of similar dimensions as Figure 4.1(a). There are two main differences between Figure 4.1(a,b). First, the islands of Figure 4.1(b) have a stronger preference to nucleate along the step edge. This is likely a result of directional diffusion that has been mentioned before[13] and will be discussed further later in this paper. The second feature is the relative number of 4-layer islands has increased, and there are a few 3-layer islands as shown in Figure 4.2(d). Both of these are associated with a higher flux in the literature[11], but in this case the deposition flux was the same as in Figure 4.1(a). The cause for this difference has not been determined, however experiments carried out at other growth conditions show that the deposition history–one deposition vs. multiple depositions–affects island nucleation and distributions. This history dependence is the same as hysteresis seen in other phase transitions like ferromagnets.

Figure 4.2(e, f) shows the area and volume distributions for Figure 4.1(b). Similar to Figure 4.2(b,c), Figure 4.2(e, f) has gaps in the distribution when compared to classical nucleation, although the x-axis scale of the graphs in Figure 4.2(e, f) slightly masks the gap. The smallest island in Figure 4.1(b) is ~900 nm^2, radius of ~17 nm, height of 3 layers, and ~26,000 atoms (shorthand: 26k atoms).

Figure 4.3(a) shows the Voronoi Cells for the same experiment as Figure 4.1(a). Using only this image about half of the Voronoi Cells extended off the edge of the image, so we used other images (not shown here) that had slight translations from Figure 4.1(a) to locate the nearest islands and construct the proper Voronoi Cells. The locations of these extra islands are represented by blue dots in the white margins of Figure 4.3(a) with the corresponding Voronoi Cells. Only islands 16, 20, 32, and 33 did not have enough information to be 100% confident the Voronoi Cells were correct, but we believe they are close. We have ignored the single step on the right side of the image for Voronoi Cell construction since the scale of our image is so

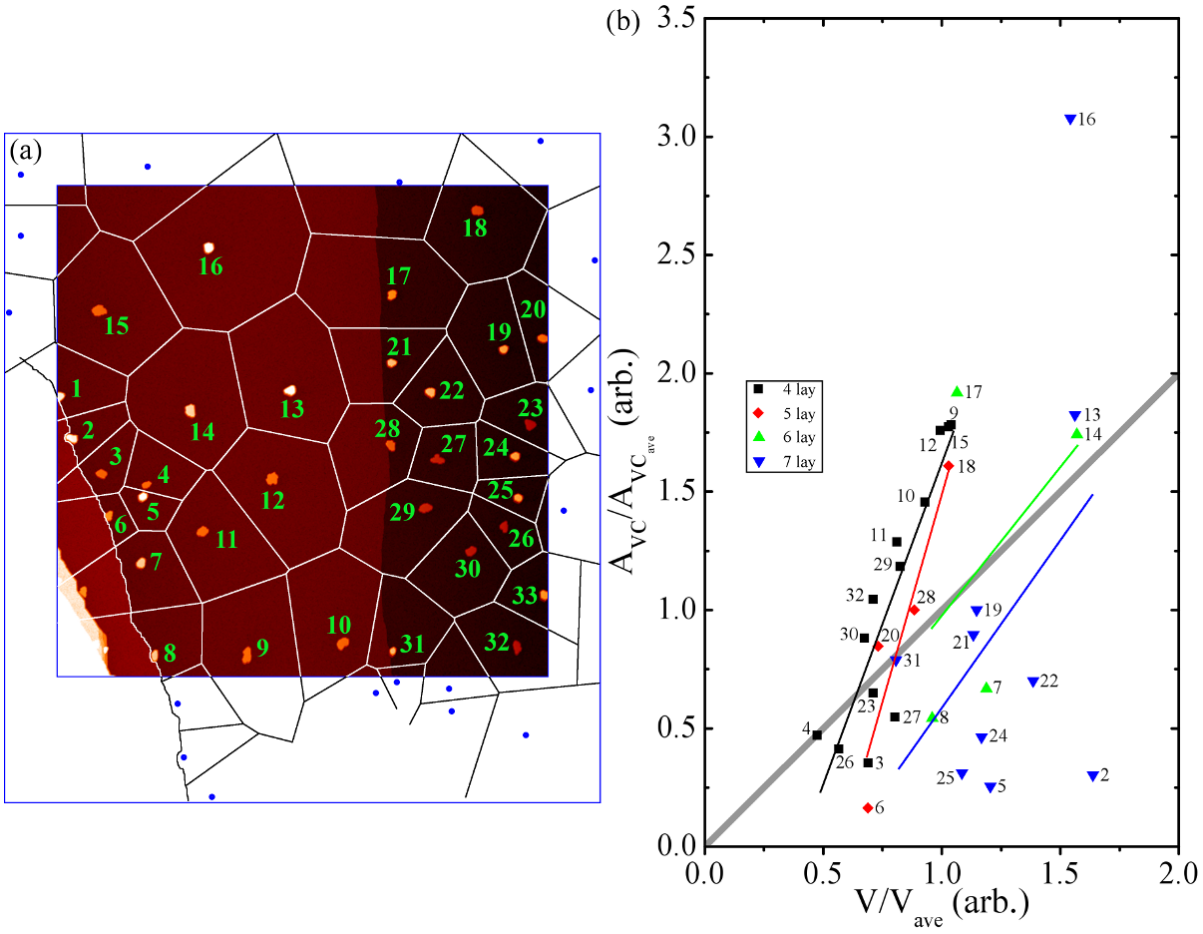

Figure 4.3 Voronoi cells for Figure 4.1(a). Additional images with slight translations were used to fully develop the Voronoi cells for this image. The lower left corner is a Si step bunch with over 30 Si steps, so this was treated as a barrier for the VC, but otherwise steps were treated the same as terraces. (b) shows the area of the Voronoi cells vs. the volume of the islands for (a). The grey line is a y = x line to compare to classical. The colored lines are best fit lines for particular heights.

large (island 28 is 100 Pb atoms wide). In later depositions, islands 28 and 31 actually grow over the step and islands 21 and 17 grow flush to the step. There is a step bunch with over 30 Si steps in the lower left corner of Figure 4.1(a) and the first step here is treated as the edge of the Voronoi Cell. Figure 4.3(b) shows the normalized area of the Voronoi Cell vs. the normalized volume of all heights of islands from Figure 4.1(a). The grey line is the y = x line. The islands are color coded according to their height, with colored lines showing a best fit line for that particular height.

The R^2 values for the four, five, six, and seven layer tall islands are 0.79, 0.86, 0.22, and 0.18 respectively with good correlation reserved for values above 0.95. For the four and five layer tall islands some of their growth is correlated to the size of their Voronoi cell area, but for six and seven layer tall islands there is very poor correlation for the island size to the Voronoi cell area. For the scaling theory of nucleation the relation between scaled island area and scaled Voronoi area is expected to be a $x = y$ line through the origin. The fitted lines in Figure 4.3(b) have non-zero intercepts and their slope is higher than 45°. Li and Evans [18] provide calculations in their Figure 9 that show classical theory predicts the island size is highly correlated to the area of the Voronoi Cell with a nearly linear relationship going through the origin. This is represented by the grey line in Figure 4.3(b). While the four and five layer islands have a linear relationship, their x-intercepts are far from zero signaling there is a minimum size of island irrespective of the Voronoi cell area. After several more depositions to a total of 1.27 ML, the R^2 value for the 7 layer islands increased to 0.76, with the 4 and 5 layer island's R^2 hovering around 0.85, indicating that after the initial island growth the Voronoi cell area may play a role in continued island growth, but a significant portion of the island growth is not related to the Voronoi cell area. This is however puzzling due to the strongly anisotropic island growth discussed later. In order to try to understand the initial island size distributions, the wetting layer has been studied as the coverage approached the critical coverage where the islands form.

Figure 4.4 shows a series of 20 x 20 nm^2 STM images for depositions of Pb on the Si(111)-7x7 surface. The images are near to each other, but not necessarily overlapping. The total deposited amount is listed in the caption. From Figure 4.4(a-d) the Si(111)-7x7 pattern is gradually covered by Pb. Figure 4.4(e-g) shows an amorphous surface with few signs of organi-

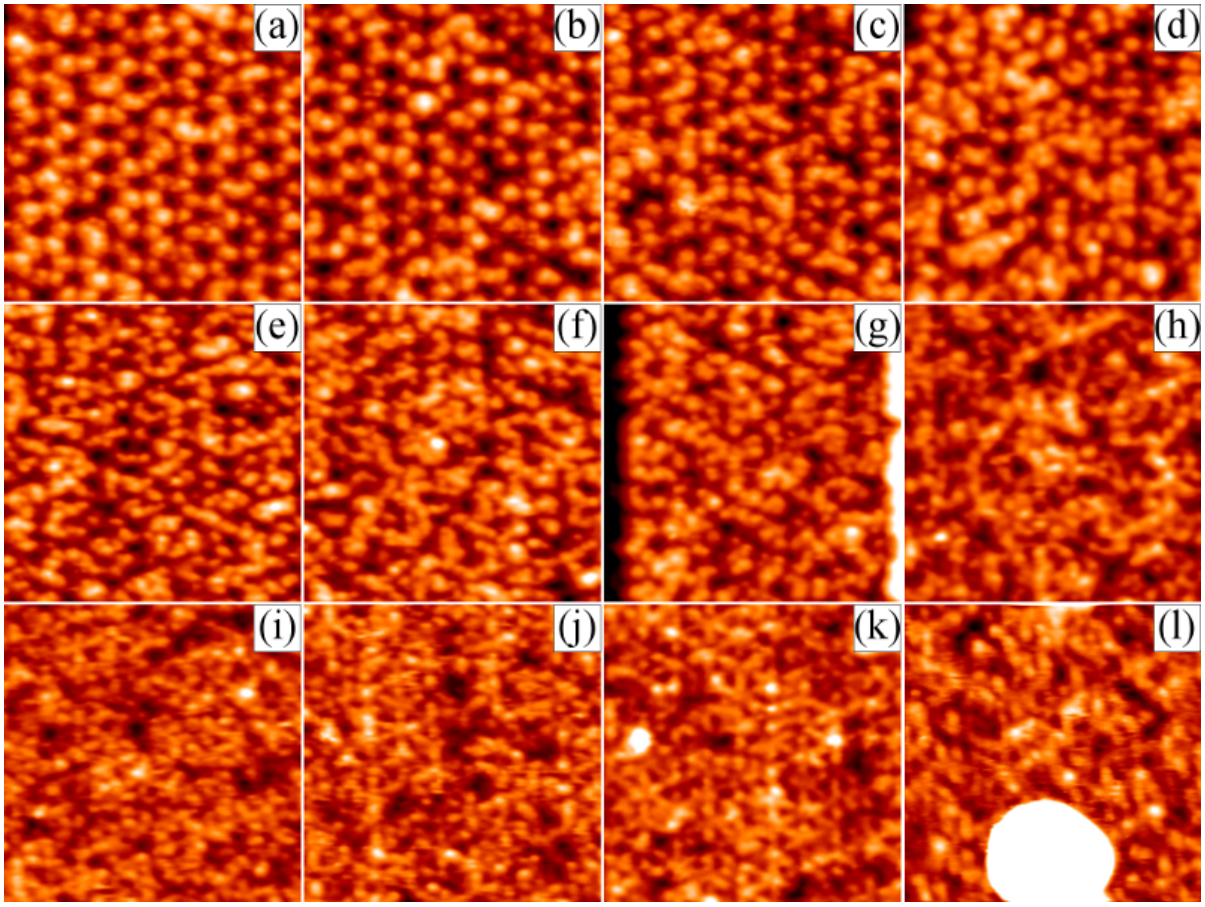

Figure 4.4 Si(111)-7x7 surface with increasing amounts of Pb deposited at 185 K. (a-l) are 20 x 20 nm^2. Deposition amount totals: (a) 0.39 ML, (b) 0.46 ML, (c) 0.52 ML, (d) 0.59 ML, (e) 0.66 ML, (f) 0.72 ML, (g) 0.79 ML, (h) 0.98 ML, (i) 1.05 ML, (j) 1.11 ML, (k) 1.18 ML, (l) 1.24 ML. The listed coverage is the nominal coverage over the whole surface. The conditions of this experiment are different from the ones in Figure 4.1.

zation. Starting in Figure 4.4(h) a few linear streaks appear with a linear pattern emerging in Figure 4.4(i-k). Ganz suggested that these streaks are Pb atoms above the dimer chains of the Si(111)-7x7 and there is no atomic resolution due to the metallic nature of the wetting layer[3]. Figure 4.4(k) was immediately before islands formed, and Figure 4.4(l) shows the wetting layer with a small island. The transition from wetting layer to Pb islands is an extremely quick process estimated to occur in a matter of seconds[20] resulting from the wetting layer reaching a critical compression. This compression allows diffusion with $x \sim t$ instead of the classical $x \sim \sqrt{t}$ and also provides a source of Pb atoms allowing the island volumes to exceed the amount of Pb deposited[13]. The wetting layer in Figure 4.4(l) looks most similar to the wetting layer in Figure 4.4(h) suggesting the amount of Pb in the wetting layer after islands form has reverted to the amount in Figure 4.4(h). This supports other Pb/Si(111) papers that have measured the volume of the islands and have shown the volume to be several times larger than the amount in the most recent deposition, implying that the Pb wetting layer becomes compressed during deposition, then decompresses when islands form[13]. The material coming from the wetting layer to form islands is not the amount within the Voronoi cells, and this could explain why the six and seven layer tall islands' volumes are able to deviate from the prediction according to the Voronoi cell area.

Figure 4.5 shows the islands from Figure 4.1(a) in blue at 1.22 ML and from a later deposition in red at 1.24 ML. The islands have been converted from an STM image to colored pixels representing their area. On the right is a 90 x 90 nm^2 zoomed in image of each island with the island number in black. The island center of mass (CM) has been calculated and marked with a green spot for blue islands (1.22 ML) and a white spot for red islands (1.24 ML). The blue number in each box is the magnitude of the change of position of the CM, and the larger image on the left has an arrow over the island indicating the direction of the change of the CM. Each island also has a black line running through the CM of the blue island. This black line is perpendicular to the direction of the change of CM and divides the island into a "short" side and a "long" side. The red percent in each box is the percent of the number of atoms that went to the long side out of the total number of atoms that joined the island, i.e. the anisotropy of atoms joining the island. For example, island 3 had 7,800 atoms join the short side and 12,900

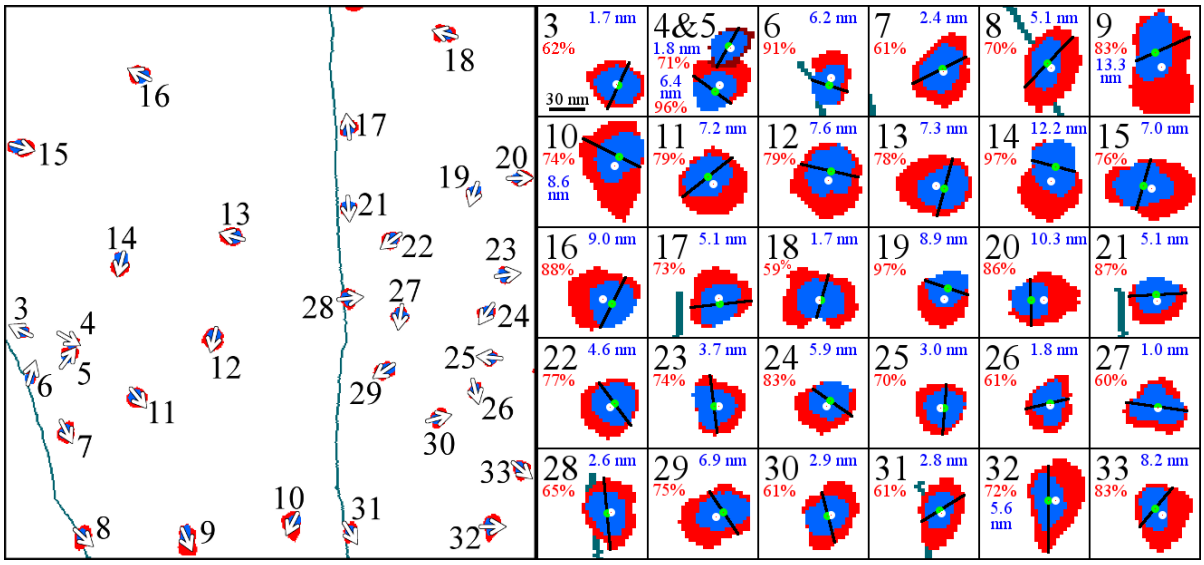

Figure 4.5 On the left, a 1440 x 1500 nm^2 overlay where blue islands are from a 1.22 ML deposition (same as Figure 4.1(a), Figure 4.3(a)), and red islands are from a 1.24 ML deposition. The teal line represents the step edge. Each island has an arrow showing the direction of the change of the center of mass. On the right, each box is 90 x 90 nm^2. Green dots show the center of mass of the 1.22 ML (blue) island, white dots show the center of mass of the 1.24 ML (red) island. The blue number is the magnitude of the change in center of mass. Each island has a black line running through the initial center of mass and perpendicular to the vector between the initial and final center of mass. This divides the island into a "long" and "short" side, with the long side being the side the final center of mass rests in. The red number is the percent of atoms that joined the long side, i.e. the anisotropy of atoms joining the island. For example, island 19 had 1.5k atoms join the short side and 50.7k atoms join the long side for an anisotropy ratio of 97%.

atoms join the long side where 12,900/(7,800+12,900) = 62%. The average number of atoms joining an island is around 50k atoms.

Many of the islands have large changes in the CM, with some approaching the radius of the initial island. For reference, the average initial radius of the islands is 17.5 nm with a minimum radius of 14 nm and maximum of 21 nm. This large change in CM is reflected by the large anisotropy in number of atoms joining the each side of the island. Out of 25 islands, 15 of them have an anisotropy of 75% or higher, meaning 3 atoms join the long side for every atom that joins the short side. The highest anisotropies seen in islands 5, 14, and 19 have [(number atoms added short)/(number atoms added long)] of [1.5k/39.4k], [2k/68.7k], and [1.5k/50.7k] respectively. This is another indication of the directional diffusion occurring on the surface and expands on previously reported results[13]. Such attachment anisotropies have not been seen in other nucleation studies.

4.4 Conclusion

The Pb/Si(111)-7x) system has been compared to classical nucleation theory and found to not follow the predictions. The basic assumptions of classical nucleation theory–monomers following random walk diffusion to form islands of a critical size with a cohesive energy–do not apply to the Pb/Si(111)-7x7 system. This results in the island size distributions and the island scaling not following the classical predictions. In particular the scaling differs depending on island height with four and five layer islands having non-zero intercepts and six and seven layer islands having poor correlation of island volume and Voronoi cells size. Part of the deviation from classical is due to the wetting layer causing unusual diffusion in the system. The directional diffusion of the wetting layer causes large anisotropies in the growth of the islands with large ratios in the number of atoms that join islands on preferred vs. non-preferred sides. With classical models ruled out, new theories will need to be developed and refined to explain the collective diffusion and resulting island behavior for the Pb/Si(111)-7x7 system.

References

[1] E. Ganz, F. Xiong, I.-S. Hwang, and J. Golovchenko, Phys. Rev. B **43**, 7316 (1991), URL http://link.aps.org/doi/10.1103/PhysRevB.43.7316. 4.2

[2] G. L. Lay, J. Peretti, M. Hanbücken, and W. Yang, Surface Science **204**, 57 (1988), ISSN 0039-6028, URL http://www.sciencedirect.com/science/article/pii/0039602888902683.

[3] E. Ganz, H. Ing-Shouh, X. Fulin, S. K. Theiss, and J. Golovchenko, Surface Science **257**, 259 (1991), ISSN 0039-6028, URL http://www.sciencedirect.com/science/article/pii/003960289190797V. 4.3

[4] M. Hupalo, S. Kremmer, V. Yeh, L. Berbil-Bautista, E. Abram, and M. Tringides, Surface Science **493**, 526 (2001), ISSN 0039-6028, URL http://www.sciencedirect.com/science/article/pii/S0039602801012626.

[5] A. Petkova, J. Wollschläger, H.-L. Günter, and M. Henzler, Surface Science **471**, 11 (2001), ISSN 0039-6028, URL http://www.sciencedirect.com/science/article/pii/S0039602800009109.

[6] A. Petkova, J. Wollschläger, H. L. Günter, and M. Henzler, Journal of Physics: Condensed Matter **11**, 9925 (1999), URL http://stacks.iop.org/0953-8984/11/i=49/a=310. 4.2

[7] K. Budde, E. Abram, V. Yeh, and M. C. Tringides, Phys. Rev. B **61**, R10602 (2000), URL http://link.aps.org/doi/10.1103/PhysRevB.61.R10602. 4.2

[8] M. H. Upton, C. M. Wei, M. Y. Chou, T. Miller, and T.-C. Chiang, Phys. Rev. Lett. **93**, 026802 (2004), URL http://link.aps.org/doi/10.1103/PhysRevLett.93.026802. 4.2

[9] M. Hupalo, J. Schmalian, and M. C. Tringides, Phys. Rev. Lett. **90**, 216106 (2003), URL http://link.aps.org/doi/10.1103/PhysRevLett.90.216106. 4.2

[10] L. L. Wang, X. C. Ma, P. Jiang, Y. S. Fu, S. H. Ji, J. F. Jia, and Q. K. Xue, Phys. Rev. B **74**, 073404 (2006), URL http://link.aps.org/doi/10.1103/PhysRevB.74.073404. 4.2

[11] C. A. Jeffrey, E. H. Conrad, R. Feng, M. Hupalo, C. Kim, P. J. Ryan, P. F. Miceli, and M. C. Tringides, Phys. Rev. Lett. **96**, 106105 (2006), URL http://link.aps.org/doi/10.1103/PhysRevLett.96.106105. 4.2, 4.3, 4.3

[12] K. L. Man, M. C. Tringides, M. M. T. Loy, and M. S. Altman, Phys. Rev. Lett. **110**, 036104 (2013), URL http://link.aps.org/doi/10.1103/PhysRevLett.110.036104. 4.2, 4.3

[13] M. T. Hershberger, M. Hupalo, P. A. Thiel, C. Z. Wang, K. M. Ho, and M. C. Tringides, Phys. Rev. Lett. **113**, 236101 (2014), URL http://link.aps.org/doi/10.1103/PhysRevLett.113.236101. 4.2, 4.3, 4.3, 4.3

[14] J. Evans, P. Thiel, and M. Bartelt, Surface Science Reports **61**, 1 (2006), ISSN 0167-5729, URL http://www.sciencedirect.com/science/article/pii/S0167572906000021. 4.2

[15] K. L. Man, M. C. Tringides, M. M. T. Loy, and M. S. Altman, Phys. Rev. Lett. **101**, 226102 (2008), URL http://link.aps.org/doi/10.1103/PhysRevLett.101.226102. 4.2

[16] L. Huang, C. Z. Wang, M. Z. Li, and K. M. Ho, Phys. Rev. Lett. **108**, 026101 (2012), URL http://link.aps.org/doi/10.1103/PhysRevLett.108.026101. 4.2

[17] E. Granato, S. C. Ying, K. R. Elder, and T. Ala-Nissila, Phys. Rev. Lett. **111**, 126102 (2013), URL http://link.aps.org/doi/10.1103/PhysRevLett.111.126102. 4.2

[18] M. Li and J. Evans, Surface Science **546**, 127 (2003), ISSN 0039-6028, URL http://www.sciencedirect.com/science/article/pii/S003960280301269X. 4.3, 4.3

[19] S. M. Binz, M. Hupalo, and M. C. Tringides, Phys. Rev. B **78**, 193407 (2008), URL http://link.aps.org/doi/10.1103/PhysRevB.78.193407. 4.3

[20] A. V. Matetskiy, L. V. Bondarenko, D. V. Gruznev, A. V. Zotov, A. A. Saranin, and M. C. Tringides, Journal of Physics: Condensed Matter **25**, 395006 (2013), URL http://stacks.iop.org/0953-8984/25/i=39/a=395006. 4.3

CHAPTER 5. SPATIAL NON-UNIFORM ISLAND GROWTH SIGNALS NON-CLASSICAL DIFFUSION IN PB/SI(111)-7X7

5.1 Abstract

In classical nucleation there is a notable regime change between the dilute phase of atoms diffusing randomly across the surface and the condensed phase once stable islands start forming. Soon after island formation most adatoms are expected to join already present islands based on their capture zones with new island formation occurring if the critical island size i is small or if island formation is irreversible. In either case the island density vs. coverage should be a gradual curve that reaches some steady state. Experiments with Pb/Si(111) at low temperatures show three generations of islands form with distinctly different island sizes and island densities (Figure 5.1), all while temperature and flux is kept constant. This leads to a step function in the island density as coverage increases and suggests that after an initial very high mobility in the wetting layer phase, 1^{st} and 2^{nd} generation islands can partially pin the superdiffusion.

5.2 Introduction

Understanding epitaxial thin film nucleation and island growth has been a priority for the surface science community for the past several decades with a general understanding of the classical case[1]. For strained heterosystems near equilibrium the typical growth mode is Stranski-Krastanov where initial growth is layer by layer to allow lattice relaxation, followed by island growth. The Pb/Si(111) system studied below room temperature had long been classified as Stranski-Krastanov. There were hints that Pb/Si(111) was not Stranski-Krastanov including the temperature range indicating the system was far from equilibrium and experi-

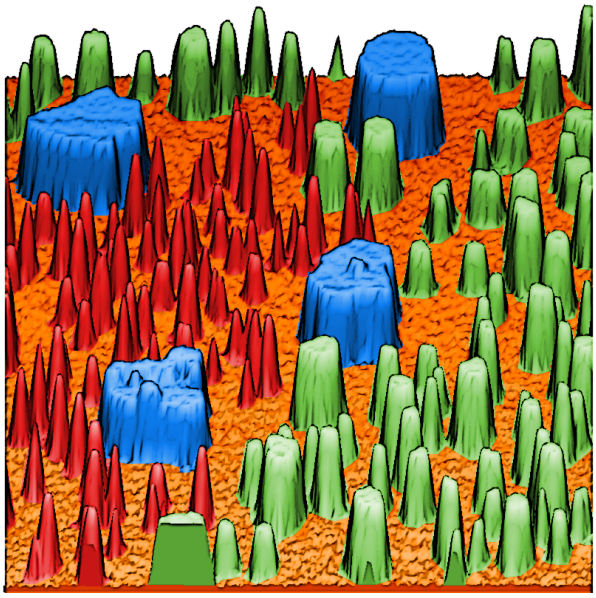

Figure 5.1 Abstract Figure: 600 x 600 nm^2 3D rendered STM image. Islands have been color coded according to generation with first generation in blue, second generation in green, and third generation in red. All islands in a generation formed for the same deposited amount in stepwise deposition experiments and each generation formed at different total coverages, contrary to classical nucleation theory.

mental evidence that the wetting layer crystallizes underneath Pb islands[2], but Chapter 3[3] shows the initial island nucleation and mass transport is unlike any classical case. This result is added to the list of remarkable properties of the Pb/Si(111) system including an experimentally realized Devil's Staircase[4], uniform height from quantum size effects[5], discrete quantum well binding energies[6], superconductivity in both the islands[7–9] and wetting layer[10,11], and collective superdiffusion[12,13] allowing fast structural transformations[14]. This chapter is the final of a series of papers (Hershberger et al.[3], Chapter 4) that identify the low temperature transition from wetting layer growth to island growth for Pb/Si(111)-7x7. Chapter 5 continues the non-classical island growth discussion from Chapter 4, focusing on continued deposition after the initial islands form and relating island growth to the known wetting layer properties.

Although nucleation theory has been presented in the Introduction Chapter 1.3 and Chapter 4, highlights of the theory pertaining to this chapter are noted. The Scaling Theory of Nucleation is a series of equations based on basic atomistic processes that has been used in epitaxial growth experiments to determine the island density for classically behaving systems.

This theory assumes atoms follow random walk diffusion across the surface with an energy barrier to hopping and a critical island size, i, with $i+1$ atoms forming a stable island. Typically island formation quickly reaches a steady state, however for small critical island sizes or if island nucleation is irreversible islands can continue forming well after island capture zones cover the surface[1]. Once a steady state is reached, newly deposited atoms tend to join the island of whichever capture zone they land in with island sizes scaling according to their capture zone area. This is in stark contrast to the observed behavior of the Pb/Si(111) system where there are zero islands until a critical coverage is reached, after which many islands form simultaneously by collecting a large number of atoms ($\sim 10^5$). Further island growth leads to sudden jumps in island density because new islands form in multiple generations.

Part of the difference in this island nucleation behavior may be a result of the behavior of the wetting layer and its role in mass transport across the surface. Studies of the Pb/Si(111) wetting layer at low temperatures, ~200 K, using laser induced thermal desorption and low energy electron microscopy to conduct a profile evolution diffusion study of an initial steep profile show the wetting layer diffusion does not follow classical expectations. When Pb is removed with the laser, the refilling front moves at a constant velocity and the front does not widen. The time constant for refilling is coverage dependent then becomes constant above a critical coverage Θ_c, orders of magnitude smaller than for $\Theta < \Theta_c$. Above the critical coverage the temperature dependence for refilling follows an Arrhenius form[12]. A model was proposed by Man et al.[12] that the collective diffusion was due to thermally generated adatom diffusion on top of the wetting layer. However, theoretical calculations by Huang et al.[15] note that conventional adatom diffusion cannot explain the diffusion behavior below the critical coverage. This theory study proposes collective liquidlike motion of the Pb atoms in the dense wetting layer, and supports the idea that below a critical coverage the collective diffusion can rapidly drop[15].

The large compression observed in the amorphous wetting layer has been discussed in the literature with suggestions that the wetting layer has a coverage of several monolayers of Pb depending on temperature[16–18]. In one case it was noted that when islands form, there are not vacancies in the wetting layer, and the roughness observed in STM does not increase[18].

This was one of the suggestions that the wetting layer is actually compressed besides the flux calibration based on diffraction oscillations. However, these experiments did not probe the explosive nucleation discussed in this Thesis. From x-ray reflectivity measurements at 610 K it was found that the liquid Pb close to the Si(111) surface was in a compressed state with a density 30% percent higher than the bulk close-packed solid Pb density. While no final explanation was given, it was estimated that a charge transfer of $0.70e$ per Pb atom would be needed to explain the observed atomic radii shrinkage[19]. At the very least, the x-ray reflectivity results demonstrate that a compressed Pb phase is possible in the liquid Pb on Si(111) system, although it is not clear if the liquid Pb phase is related to the compressed state and unusual mobility at the much lower temperatures of the current studies.

Most diffusion studies so far in the Pb/Si(111) system have focused on the behavior of the wetting layer before island formation[12,13,15], or the diffusion of Pb on Pb islands during ring formation[20,21]. With these studies in mind, this paper attempts to merge the current understanding of the wetting layer behavior with the observed nucleation of islands on the surface. This study is first time among nucleation experiments where areas on the order of μms are scanned to capture the beginning of the very first nucleation events.

5.3 Results

Figure 5.2 shows 1.5 x 1.5 μm^2 STM scans following the deposition experiment along with a graph showing the full image island density vs. coverage Θ. The gray areas on the STM scans are regions that were not covered in that particular scan and have been offset so the presented images are lined up. The red box to the left side of Figure 4.1(a) in Chapter 4 shows the typical size of scans for nucleation experiments with a schematic showing the nucleating islands are much smaller in comparison to the current experiments. The experiment started with a deposition to 0.72 ML at 200 K, then 11 stepwise depositions until islands form in Figure 5.2(a) at 1.22 ML. The first round of island formation has been termed "1^{st} generation" (1^{st} gen) islands and had an island density of $\sim$1.5 x 10^{-5} islands per nm^2. These 1^{st} gen islands are large and stable with an initial average area of $\sim$1000 nm^2 and heights ranging from 4 to 7 layers tall containing an average of 95,000 atoms with zero islands coarsening and few islands

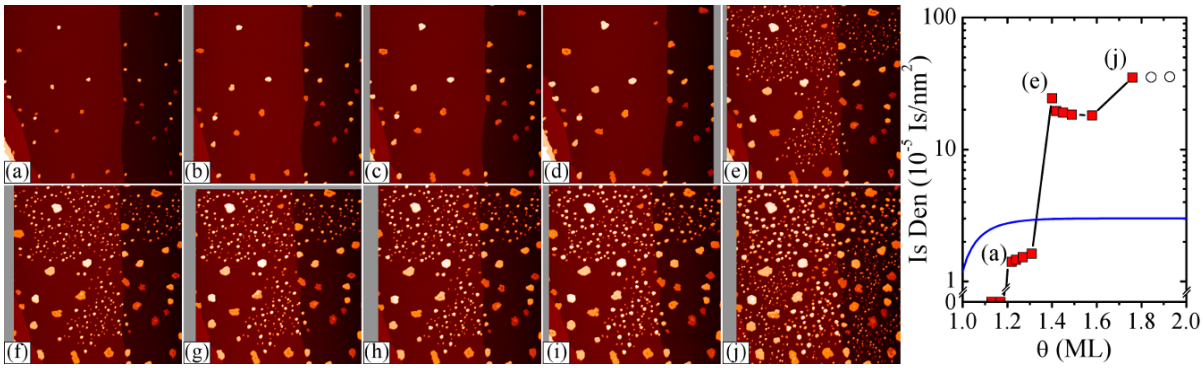

Figure 5.2 Deposition series for Pb on Si(111)-7x7. The graph on the right tracks the overall image island density for each deposition with the formations of the 1st, 2nd, and 3rd gens labeled with their image letter (a), (e), and (j) respectively. Depositions in this experiment started at 0.72 ML and continued with 0.045 ML intervals until 1st gen islands formed at 1.22 ML shown in (a). With each deposition the 1st gen islands grew larger. In (e) 2nd gen islands form in particular regions of the surface creating a sharp increase in island density. Some island coarsening slightly decreases the island density, but the 3rd gen forming in (j) again raises the density as most of the image is covered by islands. In a classical case the island density is expected to reach a steady state as shown by the blue line with an offset of 1 ML. Coverages in ML for images are (b) 1.24, (c) 1.27, (d) 1.31, (e) 1.40, (f) 1.42, (g) 1.45, (h) 1.49, (i) 1.58, and (j) 1.76.

coalescing through the remainder of the experiment. Further depositions increase the sizes of these islands, as discussed in previous work[3].

While keeping the same flux and temperature, Figure 5.2(e) shows total deposition to 1.40 ML which caused new islands to form across portions of the surface that have been termed "2nd generation" islands. The 2nd gen islands have an initial local island density of ~60 x 10^{-5} islands per nm^2 increasing the overall image island density by a factor of 10. As previously reported[22], these islands undergo coarsening leading to a slight drop in island density. As depositions continue the 2nd gen islands grow larger in area, indicating the material deposited near the 2nd gen islands is going to those islands as opposed to going the wetting layer or 1st gen islands. There are noticeable regions where the 2nd gen islands do not form. The locations of these 2nd gen islands relative to the 1st gen islands will be discussed further in Figure 5.4.

Continued deposition at constant flux and temperature leads to the formation of the "3rd generation" in Figure 5.2(j). These islands formed in the spaces between the 1st gen islands

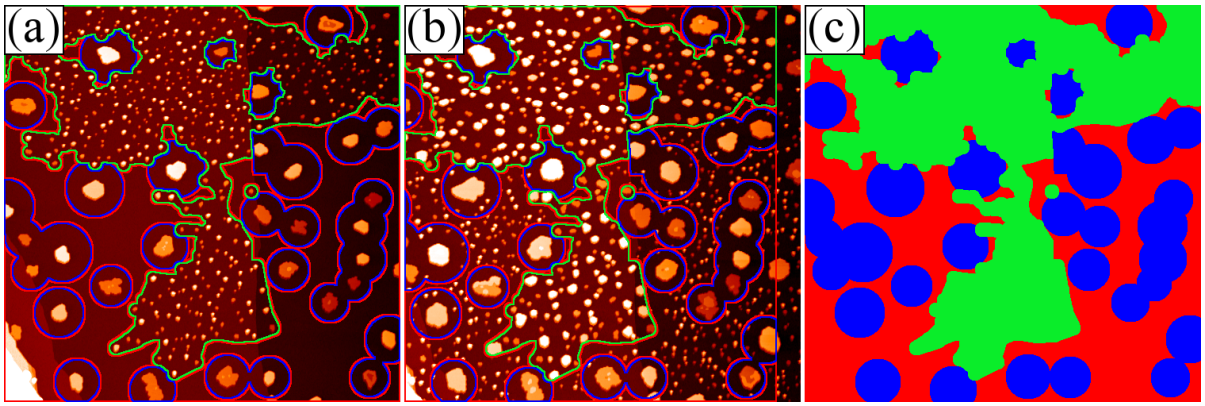

Figure 5.3 Images from Figure 5.2(e,j) where the 2nd and 3rd generation form are shown in Figure 5.3(a,b). The surface has been divided into regions based on generation to allow for mass balance calculations. 1st gen regions were based on their initial volume. 2nd gen regions were based on average size, and could encroach on the 1st gen regions. 3rd gen regions filled in the remaining area.

that the 2nd gen islands did not occupy. There are noticeable depletion rings around the 1st gen islands where no islands formed, giving an idea of the typical diffusion distance for atoms on the surface at this point. The 3rd gen started with a local island density of ~70 x 10^{-5} islands per nm^2 causing a steep increase in the island density across the surface. This stepwise change in island density with multiple island sizes has not been observed before in island nucleation to our knowledge and also is inconsistent with the assumptions of nucleation theory. Typically in nucleation the island density will quickly reach a steady state, with the blue line on the graph representing an expected classical case, including a 1 ML offset to factor in the delayed island formation.

Figure 5.3 shows the images when the 2nd gen forms in (a)–same as Figure 5.2(e)–and the 3rd gen forms in (b)–same as Figure 5.2(j). These panels have been overlaid with the three regions shown in (c). Regions near 1st gen islands are colored blue, near 2nd gen islands are green, and all remaining regions are red. The 1st gen regions were scaled based on the radius of a circle required to collect the island's volume by changing the density of the wetting layer from 1.22 ML to 1.00ML under the assumption that the area can collect all the compressed material locally. The 2nd gen regions were formed by putting circles around each 2nd gen island

with the radius based on the 2nd gen initial island density with a scaling factor of ∼1.2 on the radius to account for the random location of islands. Then any areas enclosed with 2nd gen regions were filled in as well. If a 2nd gen area intruded on a 1st gen area, the 2nd gen area took precedence. Using this method, approximately 30.2% of the image belongs to 1st gen, 39.2% to 2nd gen, and 30.6% to 3rd gen.

Figure 5.3(b) shows that almost all of the area that had not been reserved for 1st or 2nd gen formed 3rd gen islands. Additionally there are some places where 3rd gen islands form inside the 1st gen zone, and a few spots where 3rd gen islands form between 1st and 2nd gen zones. This combined with the higher local island density for 3rd gen islands suggests the diffusion length has decreased further for the formation of the 3rd gen islands, but since temperature and flux were held constant the source of the change in the diffusion must originate from the surface the atoms are diffusing through: the wetting layer.

The regions of Figure 5.3 have been compared with island volume integrations to investigate where mass is located on the surface. Figure 5.2(a,e,j) have had the total volumes of the islands on the surface measured by multiplying the height by the area of the islands, then those volumes were converted to ML of Pb(111) in those islands using the Pb step height 0.286 nm and the area of the image. The tops of the islands were used for the island's area. Tip convolution effects are a limitation of the STM-based methods and results in uncertainties of the island volumes, but this approximation does not affect the jumps in island density and the inhomogeneity of the diffusion process. The results are shown in Table 5.1 with all coverages reported and calibrated to the Pb(111) ML. The volumes of the islands and mass in the 1st, 2nd, and 3rd gen regions is reported in a unit called VolML which is equivalent to the percent of the image that would be covered by the Pb contained in a particular object. This allows direct comparison between the total volume of the Pb islands in the image and the Pb deposited on the surface in ML. The conversation is shown in Equation 5.1 with units in parenthesis:

$$\frac{V(nm^3)}{h_{Pb}(nm/Layer)A_{im}(nm^2/image)} = V(VolML) \tag{5.1}$$

where V is the total integrated volume of the islands or the calculated mass available in the generation regions, h_{Pb} is the height of the Pb(111) step, and A_{im} is the area of the image.

Table 5.1 Integrations of the total amount of material in the islands for each generation converted from volume to ML using the Pb(111) step height 0.286 nm and the area of the image. The analysis shows that material from the other regions must feed the 1st gen islands.

Fig. 1—Gen	Total Dep (ML)	ΔDep (ML)	VolML in Region (30.2/39.2/30.6)%			VolML in Islands			Island Total (VolML)	Wet Layer Ave. (ML)	VolML Gained by Islands		
			1st Gen	2nd Gen	3rd Gen	1st Gen	2nd Gen	3rd Gen			1st Gen	2nd Gen	3rd Gen
(a)—1st	1.22		0.07	0.09	0.07	0.04			0.04	1.18			
(e)—2nd	1.40	0.18	0.12	0.16	0.12	0.18	0.08		0.26	1.14	0.14		
(j)—3rd	1.76	0.36	0.23	0.30	0.23	0.33	0.29	0.05	0.67	1.09	0.15	0.21	

The first column in the table lists which image from Figure 5.2 the data is from: (a) where the 1st gen forms, (e) where the 2nd gen forms, or (j) where the 3rd gen forms. The Total Dep column is the total coverage deposited at that point, while the ΔDep is the amount deposited since the previous row (there were depositions in between, but for comparison between generations these other depositions are ignored). The red columns are how material is available in the 1st gen region, 2nd gen region, and 3rd gen region in units of VolML calculated from the area image percents in Figure 5.3 assuming the wetting layer cannot drop below 1.00 ML (i.e. 0.22 ML x 30.2% = 0.07 VolML). This assumption that locally the density of the wetting layer surrounding the 1st gen islands can drop as low as 1 ML, (the density of the uncompressed layer) will be tested by comparing the amounts required at each generation to provide the mass to the islands. The green columns are the amount of material in the islands from the STM island measurements reported in VolML. The purple Wetting Layer column is the total deposition minus the total amount in the islands. The blue-green columns show the change in island volume in VolML from the green columns. Interpretation of the values is left to the discussion section.

Figure 5.4 is designed to investigate the relation between the locations of the 1st gen islands and the locations of the 2nd gen islands. Figure 5.4(b,d) are the original STM 1500 x 1500 nm^2 images with Figure 5.4(b) the same as Figure 5.2(e). Figure 5.4(d) is from a different experiment where the initial 1st gen islands were formed at 200 K, then the temperature was immediately lowered to 180 K for further deposition. Figure 5.4(a,c) were constructed by setting all 1st gen islands at a distance of zero, then making a contour map of the distance from a 1st gen island. All distances closer than 30 nm were colored white and above 30 nm the

color coding changed every 30 nm according to the legend. It is important to note that near the edges it is possible that there is a 1st gen island just off the image that could change the distance coding for that section.

This map shows a few interesting trends. In Figure 5.4(a), hardly any 2nd gen islands formed closer than 90 nm–the white, light purple, or purple regions. The few 2nd gen islands that did form closer than 90 nm to a 1st gen island were typically around 1st gen islands that were isolated from other 1st gen islands. Second, almost all of the regions farther than 180 nm–the green, yellow, orange and red regions–are covered with second generation islands. Figure 5.4(c) has a similar minimum distance effect, but requires distances above 240 nm–yellow, orange, and red regions–to be mostly covered. This result is likely from the experiment procedure. For Figure 5.4(c,d) the 1st gen islands were formed at 200 K, but immediately afterwards cooled down to 180 K. It is known that lowered temperatures increase the amount of material that can be stored in the wetting layer before Pb islands form[16–18]. There have also been Pb island ring growth experiments where large Pb islands were formed at 240 K, then the temperature was dropped 180 K for the ring studies. These experiments show 2nd gen islands covering the surface, but the change in island density was attributed to the change in temperature resulting in lowered diffusion[20]. In the Figure 5.4(c,d) experiment the farther distance of the 2nd gen islands could be reflective of more material being required to join the wetting layer when the temperature was lowered so the critical coverage is only reached when islands are further from 1st gen islands. Another possibility for the increased average distance in Figure 5.4(c,d) is a lowered superdiffusion co-efficient due to Arrhenius behavior[12]. The distance effect is investigated further in Figure 5.5.

Figure 5.5(a, d) show histograms of the distances between the 1st and 2nd gen islands. Figure 5.5(b, e) show histograms of the distance from a 2nd gen island to the nearest 2nd gen neighbor. Figure 5.5(c, f) is a graph showing the percent of each zone covered by 2nd gen islands or the probability to nucleate an island r distance away from a given 1st gen island taken as the origin. Figure 5.5(a-c) come from Figure 5.4(b) and Figure 5.5(d-f) come from Figure 5.4(d).

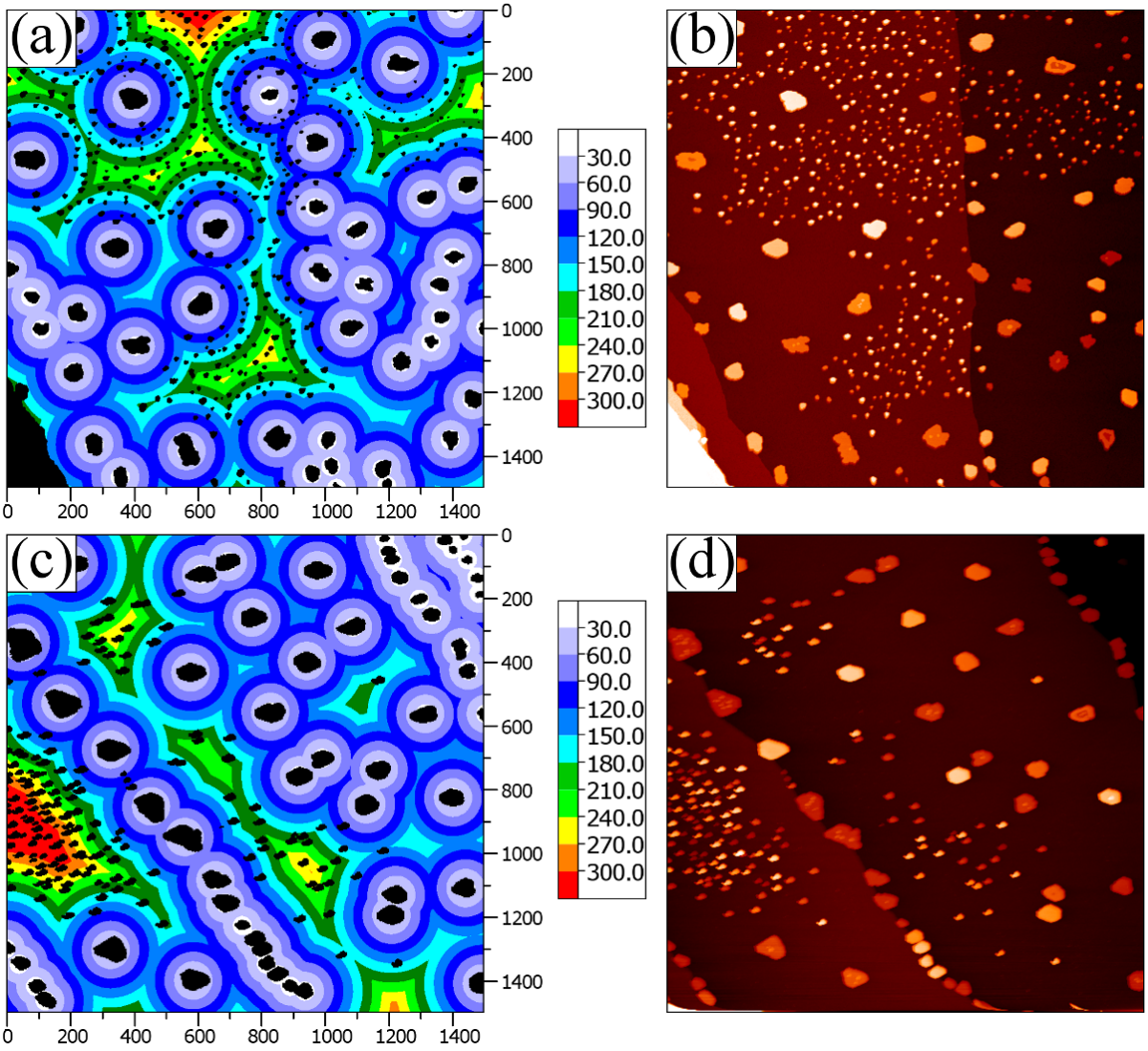

Figure 5.4 Two experiments with 1st and 2nd gen islands where (a,c) show the distance of a particular point from the center of the nearest 1st gen island with islands overlaid in black, and (b,d) are the original STM images. All numbers are in nm with the original images being 1500 x 1500 nm^2. In the first experiment shown in (a,b) 1st gen islands were formed at 200 K, then depositions continued at 200 K. In the second experiment in (c,d) 1st gen islands were formed at 200 K, but then the surface was cooled to 180 K to form 2nd gen islands. The initial 1st gen islands were determined by growth at 200 K with the islands being larger in (d) with more islands trapped at step. This may be caused by the wetting layer moving normal to the steps during island formation.

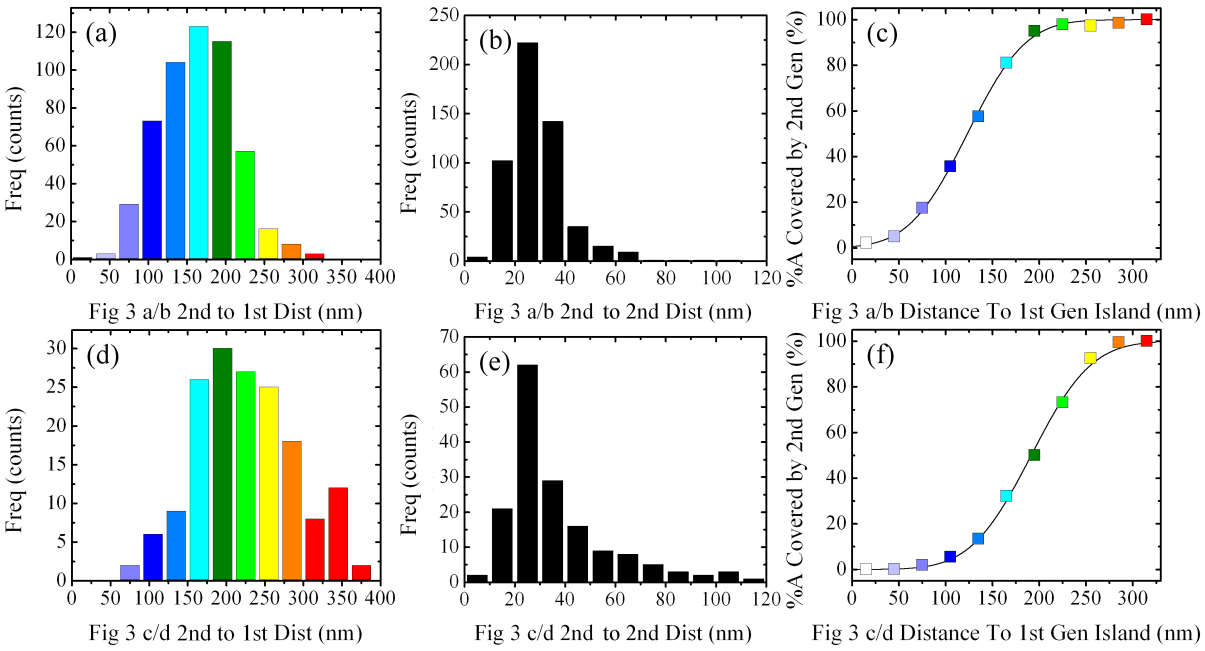

Figure 5.5 Statistics from the experiments shown in Figure 5.4. Figure 5.5(a-c) is from Figure 5.4(b) and Figure 5.5(d-e) is from Figure 5.4(d). Figure 5.5(a,d) shows a histogram of the distance between 1st gen and 2nd gen islands with corresponding colors to Figure 5.4. (b,e) shows a histogram of the nearest neighbor distance between 2nd gen islands. Since different distance regions on the surface do not have the same total area this skews the absolute number of 2nd gen islands seen in (a,d), so (c,f) reports the percent of each distance region covered by 2nd gen islands. Black lines are an error function fit of the data with the fits discussed in the text. This possibly indicates that directional diffusion primarily feeds the 1st generation islands so 2nd generation islands form at the areas farther away from them.

Figure 5.5(a, d) have bin widths of 30 nm with the bins color coded to Figure 5.4. The distribution of Figure 5.5(a) is uni-modal with a large jump at 90 nm and a large drop at 210 nm. The dropoff at 210 nm is related to a decrease in the amount of area on the surface that is actually farther than 210 nm from a 1^{st} gen island. The peak in the Figure 5.5(d) 1^{st} to 2^{nd} gen distribution is slightly higher than Figure 5.5(a) at around 200 nm. The Figure 5.5(d) distribution has a more gradual drop off, but again, the decrease is related to less of the surface being the farther distances away from 1^{st} gen islands.

Figure 5.5(b, e) show the distributions of the 2^{nd} gen island to the nearest 2^{nd} gen island without pair removal. These distributions both show a peak between 20 and 30 nm. This distance is much smaller than the average island separation for the 1^{st} gen islands. In fact, it is almost as small as the 1^{st} gen initial average island radius ($\sim$17.5 nm). While there does not appear to be a significant shift in the peak location due to the lowered temperature to form the 2^{nd} gen in Figure 5.4(d), there is a longer extended tail for the distribution in Figure 5.5(e). While not shown here, after the initial 2^{nd} gen islands formed there was limited numbers of new 2^{nd} gen islands that formed on subsequent depositions which filled in areas that would be expected to have 2^{nd} gen islands, specifically the light green region on the top edge of Figure 5.4(c) and the dark green spot in the upper right of Figure 5.4(c). This continued island nucleation decreased the extent of the tail in the 2^{nd} gen to 2^{nd} gen histogram, and is attributed to the lowered temperature.

Due to the histogram of 1^{st} to 2^{nd} gen island distance being skewed by a decreasing availability of the farther away regions, the area percent coverage was graphed in Figure 5.5(c, f). The percent of coverage for each 30 nm range (0 to 30 nm, 30 to 60 nm, 60 to 90 nm, etc.) was calculated by drawing a circle around each 2^{nd} gen island with a radius of 33 nm (based on average island separation) and summing the area of the range covered, then dividing by that range's total area. This in effect was an integration of the area covered with renormalization to account for the higher ranges, i.e. 270 nm to 300 nm, covering a smaller portion of the total surface area. It is little surprise that the resulting graph follows an error function distribution, which is the integration of a Gaussian distribution. From this we can extract the average distance and standard deviation of where 2^{nd} gen islands form by using an error function fit of

form:

$$y = C + D \text{ erf}\left[\frac{(x-a)}{b}\right] \tag{5.2}$$

where a is the average distance, b is the standard deviation, and C and D are constants both equal to 50 to shift the error function to have a range between 0 and 100 percent. In the first experiment in Figure 5.4(b) the average 2^{nd} gen island formation was at 123.1 nm with standard deviation 69.4 nm, and in the second experiment in Figure 5.4(d) the average 2^{nd} gen island formation was at 191.4 nm with standard deviation 71.6 nm.

5.4 Discussion

The island density results observed in Figure 5.2 are contrary to classical nucleation. In classical nucleation, there can be significant island formation in the steady-state regime if the critical island size is small or if island formation is irreversible[1]. None of the 1^{st} gen islands dissociated or grew smaller and it is very unlikely that the material from the few 2^{nd} gen islands that dissociated would be able to specifically make it to the open regions between the 1^{st} gen islands to contribute to 3^{rd} gen islands. The classical explanation for continued island nucleation using irreversible island formation does not seem like a reasonable explanation for the 2^{nd} and 3^{rd} gen islands in the Pb/Si(111)-7x7 system.

Concerning the possibly that small critical island size can allow for continued island formation, we will start with the assumption that critical island size is valid for this system and discuss the impact. Next we will follow previous discussion[3] that classical nucleation does not hold for this system. Assuming classical nucleation does hold, due to the very low density of 1^{st} generation islands it is unlikely that the critical island size was small when the 1^{st} gen islands formed. As discussed in Chapter 4 Figure 2, the island size distributions would suggest a critical island size of upward of $i = 6$ if classical nucleation were to hold. It is possible after the 1^{st} gen islands formed the critical island size changed, but if the critical island size changed right after the 1^{st} gen islands formed it would be expected that a few islands would form with each deposition, instead of no islands forming for several depositions then all 2^{nd} gen islands forming at the same time as observed in the experiment.

As previously discussed[3], the Pb/Si(111)-7x7 system first forms a wetting layer of Pb. The initial island formation does not follow classical nucleation where single nucleation sites gradually build up to islands as more material is deposited. Instead it is an explosive nucleation forming four to seven layer tall islands where the islands gained more material than was actually deposited signaling the wetting layer is not an isolated layer, but a reservoir for Pb atoms[3].

One possible explanation for the 2nd gen islands is the collective diffusion coefficient changed after the 1st gen islands formed. This is a distinct idea from the critical island size change and is aligned with the islands forming at a certain wetting layer density. The change in diffusion length is plausible considering the wetting layer was initially compressed to 22% more dense than the Pb(111) plane. Based on the volumes of the initial Pb islands being larger than the amount deposited[3], material must have come from the wetting layer, lowering its density. Experiments with LEEM and theory studies show that the density of the wetting layer is critical to the superdiffusion in the Pb/Si(111) system[12,15]. The LEEM experiments and following theory suggest the classical nucleation equation with a diffusion barrier ΔE and successful hopping proportional to $e^{\left(\frac{-\Delta E}{k_B T}\right)}$ does not correctly model this system[15]. Immediately after the 1st gen formation, the 2nd gen regions could have had diffusion "frozen out" by low local coverages due to material going from the wetting layer to the 1st gen islands. As depositions continued, the density of the local wetting layer increased enough to allow diffusion again. The presence of the 1st gen islands could have caused pinning centers for the density of the wetting layer, preventing the wetting layer from reaching the density (and hence long diffusion length) when the 1st gen formed, resulting in a lower density and lower diffusion length for the 2nd gen islands. During deposition local regions are still able to reach the critical density to form islands, but due to lowered collective diffusion the island density is much higher. The idea that the wetting layer could transfer mass until it fell below the critical density originates from Pb island rings growth experiments[20,21]. In these experiments Pb would be transferred to stable islands until the Pb wetting layer fell beneath the critical density. A small Pb deposition could restart the process of island ring growth. However, this chapter is the first time the wetting layer diffusion has been used to explain the drastic change in island size and density at constant temperature and flux.

The information in Table 5.1 gives some interesting insight on the mass balance in the system as islands are forming. Throughout this analysis there is a key assumption that island formation cannot cause the wetting layer to drop below the density of the Pb(111) plane, i.e. below 1.00 ML. This is a reasonable assumption since other experiments show the diffusion in the wetting layer drastically drops as the wetting layer coverage decreases below a critical point, and if the wetting layer was less dense than the islands, there should be a flow of material from the islands to the wetting layer to balance densities.

From Table 5.1, immediately after the initial island formation in Figure 5.2(a) the 1^{st} gen islands had a volume of 0.04 VoLML. This is less than the amount available in the 1^{st} gen region and is normal. In Figure 5.2(e) the amount in the islands, 0.18 VolML, is larger than the amount available in the 1^{st} gen region, 0.12 VolML. This shows that material must be transferring across areas suggesting mesoscopic scale motion. The exact nature of this motion, what causes the nucleation sites, and what causes the flow of material to these locations is still not known and must be related to local concentration fluctuations. Resolution of these questions requires experiments using a technique with both real time and spatial resolution beyond the STM capabilities. The amount for the 1^{st} gen islands in Figure 5.2(j) reaches the same conclusion with the amount in the 1^{st} gen islands being 0.33 VolML while the amount available was 0.23 VolML. Looking at the 2^{nd} gen islands for Figure 5.2(j), their total volume, 0.29 VolML, has reached the total amount available in their region, 0.30 VolML. Based on Figure 5.4 and Figure 5.5 showing the 2^{nd} gen islands tend to form in areas farther from 1^{st} gen islands, it seems that as the 1^{st} gen islands grow they gather material from outside their region. Near to the 1^{st} gen islands more material is collected, preventing islands from being able to grow in the 3^{rd} gen region when the 2^{nd} gen islands form. The 2^{nd} gen regions are able to collect the material in their local area, possibly collecting some material from the 3^{rd} gen region as well. The high density of the 2^{nd} gen islands pins the wetting layer around the 2^{nd} gen islands. The idea that the 1^{st} gen islands do not collect from the 2^{nd} gen region after 2^{nd} gen formation is supported by observing that from (e) to (j) the 1^{st} gen grows (0.15 VolML) more than the material added to the 1^{st} gen region (0.23 - 0.12 = 0.11 VolML), while at the same time the 2^{nd} gen island total volume (0.29 VolML) approaches the total amount available

in the 2nd gen region (0.30 VolML). With the 2nd gen islands present on the surface and also collecting material, it seems like the 1st gen islands would not be able to collect from that region as well. Following with the idea that the 2nd gen islands have a higher density because of a lowered diffusion distance hence a lower wetting layer density and keeping some smoothness to the density profile, it is likely that at least a small amount of material left the 2nd gen area between (a) and (e). The generalized conclusion from the mass balance analysis of Figure 5.3 and From Table 5.1 was based on the integrated island volumes in each region and was used to check for evidence that the wetting layer drops below Θ_c.

This discussion has completely left out geometry considerations. From previous experiments the highly anisotropic growth of the 1st gen islands (material is added from the same direction in neighboring islands as discussed in chapter 3) suggests a careful study of the island growth and relative island locations is needed. Another important series of experiments could attempt to extract the local density from the differences in the amorphous pattern in Chapter 4 Figure 4.4 to map local wetting layer densities. In that image the global coverage listed is based on the flux rate and deposition time. This wetting layer density mapping could add more information about the directional diffusion and how it relates to the wetting layer dropping below Θ_c.

The data in Figure 5.5(c, f) gives evidence for the distance from the 1st gen islands being important to the nucleation of the 2nd gen islands, and supports that the islands can cause the local wetting layer to be pinned at a lower density. Following the model that islands form when the local wetting layer density reaches a critical point, the results suggest the wetting layer density is lower near the 1st gen islands than in regions far away from 1st gen islands. Examining Figure 5.2(j) shows that 3rd gen islands form even closer to the 1st gen islands, pointing to the diffusion distance changing. The overall conclusion is that the 2nd gen islands do require a minimum distance from the 1st gen islands in order to form, which provides evidence for the local density and the diffusion distances being critical for island nucleation. It also suggests long range diffusion is still operating and feeding material to the 1st gen islands from the empty regions that did not form 2nd gen islands.

If the assumption for the 2nd gen islands being formed due to a changing diffusion length caused by a change in wetting layer density is correct, this may be able to explain the strong

anisotropy of the 1st gen island growth discussed in Chapters 3 and 4. If during initial 1st gen island growth only portions of the wetting layer had the local density decreased by transferring atoms to the 1st gen island, then there would be zones where Pb atoms could diffuse and zones where diffusion was frozen out by a low local wetting layer density. This could explain Chapter 4 Figure 5 that shows highly anisotropic island growth and Chapter 3 Figure 4 which shows island have preferred growth directions that persist over multiple depositions. The wetting layer on one side of the island could have a low density and not allow diffusion. Note that the paths tracking the centers of mass in Chapter 3 Figure 4 are not straight lines. As deposition continues, the wetting layer density in zones that had been initially depleted could increase to a point where diffusion was active again changing the number of incoming atoms to the islands.

The ultrafast diffusion experiments have shown that material is transported linearly $x \sim t$ (and not $x \sim t^{1/2}$ as in normal random walk) from the wetting layer to the islands. Since many islands exist within the collection area it is not possible for all of them to grow isotopically.

5.5 Conclusions

In summary, experiments depositing Pb on Si(111)-7x7 at low temperatures show non-classical island nucleation. Continued depositions after initial island formation cause a second and third generation of islands to form with distinctly different island sizes and densities while the temperature and flux is held constant. An analysis of the volume of the islands suggests the 1st gen islands collect more material than in their immediate area, signaling they could be lowering the density of the wetting layer across the surface with collective diffusion required to move the material. The locations of the 2nd gen island formation and empty areas lacking 2nd gen formation suggest the relative distance between 1st and 2nd gen is key, and supports ideas that the wetting layer density is decreased by previous island formation, causing superdiffusion to be limited. This model could help explain previous observations that Pb island growth is highly anisotropic, however further studies are needed to understand the relationship between the wetting layer diffusion and island growth. The unusual results of explosive nucleation, jumps in island number density, and collective diffusion resulting in islands and empty areas are seen directly from the raw STM data, but the full explanation is still open for theorists.

References

[1] J. Evans, P. Thiel, and M. Bartelt, Surface Science Reports **61**, 1 (2006), ISSN 0167-5729, URL http://www.sciencedirect.com/science/article/pii/S0167572906000021. 5.2, 5.4

[2] R. Feng, E. H. Conrad, M. C. Tringides, C. Kim, and P. F. Miceli, Applied Physics Letters **85**, 3866 (2004), URL http://dx.doi.org/10.1063/1.1812593. 5.2

[3] M. T. Hershberger, M. Hupalo, P. A. Thiel, C. Z. Wang, K. M. Ho, and M. C. Tringides, Phys. Rev. Lett. **113**, 236101 (2014), URL http://link.aps.org/doi/10.1103/PhysRevLett.113.236101. 5.2, 5.3, 5.4

[4] M. Hupalo, J. Schmalian, and M. C. Tringides, Phys. Rev. Lett. **90**, 216106 (2003), URL http://link.aps.org/doi/10.1103/PhysRevLett.90.216106. 5.2

[5] K. Budde, E. Abram, V. Yeh, and M. C. Tringides, Phys. Rev. B **61**, R10602 (2000), URL http://link.aps.org/doi/10.1103/PhysRevB.61.R10602. 5.2

[6] M. H. Upton, C. M. Wei, M. Y. Chou, T. Miller, and T.-C. Chiang, Phys. Rev. Lett. **93**, 026802 (2004), URL http://link.aps.org/doi/10.1103/PhysRevLett.93.026802. 5.2

[7] D. Eom, S. Qin, M.-Y. Chou, and C. K. Shih, Phys. Rev. Lett. **96**, 027005 (2006), URL http://link.aps.org/doi/10.1103/PhysRevLett.96.027005. 5.2

[8] T. Nishio, T. An, A. Nomura, K. Miyachi, T. Eguchi, H. Sakata, S. Lin, N. Hayashi, N. Nakai, M. Machida, et al., Phys. Rev. Lett. **101**, 167001 (2008), URL http://link.aps.org/doi/10.1103/PhysRevLett.101.167001.

[9] C. Brun, I.-P. Hong, F. m. c. Patthey, I. Y. Sklyadneva, R. Heid, P. M. Echenique, K. P. Bohnen, E. V. Chulkov, and W.-D. Schneider, Phys. Rev. Lett. **102**, 207002 (2009), URL http://link.aps.org/doi/10.1103/PhysRevLett.102.207002. 5.2

[10] T. Zhang, P. Cheng, W.-J. Li, Y.-J. Sun, G. Wang, X.-G. Zhu, K. He, L. Wang, X. Ma, X. Chen, et al., Nature Physics **6**, 104 (2010), URL http://www.nature.com/nphys/journal/v6/n2/abs/nphys1499.html. 5.2

[11] C. Brun, T. Cren, V. Cherkez, F. Debontridder, S. Pons, D. Fokin, M. Tringides, S. Bozhko, L. Ioffe, B. Altshuler, et al., Nature Physics **10**, 444 (2014), URL http://www.nature.com/nphys/journal/v10/n6/abs/nphys2937.html. 5.2

[12] K. L. Man, M. C. Tringides, M. M. T. Loy, and M. S. Altman, Phys. Rev. Lett. **101**, 226102 (2008), URL http://link.aps.org/doi/10.1103/PhysRevLett.101.226102. 5.2, 5.3, 5.4

[13] K. L. Man, M. C. Tringides, M. M. T. Loy, and M. S. Altman, Phys. Rev. Lett. **110**, 036104 (2013), URL http://link.aps.org/doi/10.1103/PhysRevLett.110.036104. 5.2

[14] A. V. Matetskiy, L. V. Bondarenko, D. V. Gruznev, A. V. Zotov, A. A. Saranin, and M. C. Tringides, Journal of Physics: Condensed Matter **25**, 395006 (2013), URL http://stacks.iop.org/0953-8984/25/i=39/a=395006. 5.2

[15] L. Huang, C. Z. Wang, M. Z. Li, and K. M. Ho, Phys. Rev. Lett. **108**, 026101 (2012), URL http://link.aps.org/doi/10.1103/PhysRevLett.108.026101. 5.2, 5.4

[16] M. Jałochowski and E. Bauer, Journal of Applied Physics **63**, 4501 (1988), URL http://dx.doi.org/10.1063/1.340145. 5.2, 5.3

[17] K. Edwards, P. Howes, J. Macdonald, T. Hibma, T. Bootsma, and M. James, Surface Science **424**, 169 (1999), ISSN 0039-6028, URL http://www.sciencedirect.com/science/article/pii/S0039602898008802.

[18] M. Hupalo, S. Kremmer, V. Yeh, L. Berbil-Bautista, E. Abram, and M. Tringides, Surface Science **493**, 526 (2001), ISSN 0039-6028, URL http://www.sciencedirect.com/science/article/pii/S0039602801012626. 5.2, 5.3

[19] H. Reichert, M. Denk, J. Okasinski, V. Honkimäki, and H. Dosch, Phys. Rev. Lett. **98**, 116101 (2007), URL http://link.aps.org/doi/10.1103/PhysRevLett.98.116101. 5.2

[20] M. Hupalo and M. C. Tringides, Phys. Rev. B **75**, 235443 (2007), URL http://link.aps.org/doi/10.1103/PhysRevB.75.235443. 5.2, 5.3, 5.4

[21] M. Tringides, M. Hupalo, K. Man, M. Loy, and M. Altman, *Wetting Layer Super-Diffusive Motion and QSE Growth in Pb/Si* (Springer Berlin Heidelberg, Berlin, Heidelberg, 2011), pp. 39–65, ISBN 978-3-642-16510-8, URL http://dx.doi.org/10.1007/978-3-642-16510-8_3. 5.2, 5.4

[22] C. A. Jeffrey, E. H. Conrad, R. Feng, M. Hupalo, C. Kim, P. J. Ryan, P. F. Miceli, and M. C. Tringides, Phys. Rev. Lett. **96**, 106105 (2006), URL http://link.aps.org/doi/10.1103/PhysRevLett.96.106105. 5.3

CHAPTER 6. INVESTIGATION OF THE GROWTH OF EPITAXIAL GRAPHENE ON SIC WITH SPALEED

6.1 Abstract

Long before graphene became a hot topic, the SiC(0001) system with a "graphite monolayer" had been characterized in 1975. For the next three decades leading up to the recent graphene revolution the nature of SiC(0001) surface, the $6\sqrt{3}/0^{\text{th}}$/buffer layer of graphene, and the fully formed layers of graphene were debated through Low Energy Electron Diffraction, Scanning Tunneling Microscopy, Photoemission Spectroscopy, theoretical modeling, and many other techniques. With the recent realization of single layer graphene systems, the SiC system has been revisited to investigate the properties of graphene. While this system has been widely studied, there is still debate about the structure of the buffer layer of the SiC(0001) system. In this paper we use Spot Profile Analyzing Low Energy Electron Diffraction to further the structure discussion. The $5/13^{\text{th}}$ spot has been identified as key to determining the status of the surface, with the $5/13^{\text{th}}$ spot first appearing with the onset of the buffer layer. Additionally, a broad component likely related to electron confinement in a 2D layer surrounds the (00) specular and Gr{10} spots when monolayer graphene is on the surface and can also be used to identify the transition from the buffer layer to graphene.

6.2 Introduction

With graphene's isolation and discovery of remarkable properties in 2004[1,2] there has been a rush to develop new techniques to isolate large, defect free sheets of graphene[3–5]. One of the best methods for preparing graphene has been known and studied since 1975[6]–epitaxial preparation of Graphene on SiC–although until the early 2000's the grown over layers were

thought of in terms of a few layers of graphite. In this method a sample of SiC is heated to ∼1100°C causing Si to evaporate quicker than C[1,7]. This leaves a carbon rich layer behind. The first carbon layer is referred to as the buffer layer[8] or 0^{th} layer graphene[9] and is the source of the $6\sqrt{3}$ R30° diffraction pattern[6]. It has been confirmed that this buffer layer only contains carbon atoms[10]. Although scanning tunneling microscopy (STM) has shown the atom arrangement of the buffer layer is similar to graphene[11], x-ray standing wave studies have shown that there are two chemically distinct carbon species in the sp^2 and sp^3 configurations with the sp^3 carbon bonded to Si atoms in the topmost layer of SiC[10] with additional dangling bonds[12] from the surface Si atoms visible in STM[13]. (There is disagreement between the percent of bonding between the sp^3 carbon atoms in the buffer layer and the topmost Si layer[10,14–16], but this discrepancy is most likely due to differences in surface preparation.) This causes the buffer layer band structure to lack the typical Dirac cones associated with graphene[12,17,18], and under still not well characterized growth conditions[19] cause a semiconducting bandgap to open[16,20]. Further heating causes an additional carbon rich layer to form at the SiC surface thus becoming a new 0^{th} layer and separating the previous 0^{th} layer from the surface[14]. This changes the previous buffer layer into slightly n-doped graphene with Dirac cones at the K-point typical for one graphene layer[9,21] and a gapped band structure for bi-layer graphene[18]. Through numerous studies[1,6,13,22,23] there is general consensus that there are multiple structures present for various conditions including 1x1 SiC, 3x3, $\sqrt{3}$ R30°, $6\sqrt{3}$ R30°, 6x6/Psuedo6x6, 5x5, and graphene rotated 30° from the 1x1 SiC. The exact nature of these structures continues to be debated in the literature[11,13,14,16,20]. Understanding the structure of the graphene and SiC interface is extremely important as experiments attempt to dope graphene by intercalating atoms.

The initial 1975 paper immediately identified the buffer layer reconstruction as a $6\sqrt{3}$ R30° of SiC due to the graphite/graphene spot (∼125%BZ_{SiC}) being commensurate with 13 times the SiC $6\sqrt{3}$ structures (∼125%BZ_{SiC})[6]. Various STM studies[22] clearly show a 6x6/psuedo 6x6 repeating unit cell with some STM studies[13] showing evidence of a $6\sqrt{3}$ unit cell. The 2D Low Energy Electron Diffraction (LEED) pattern shows a multitude of spots including 6x6 superstructure spots around both the SiC{10} spots and the Gr{10} spots and various other

satellite spots[6,22,23]. Due to the electron gun typically blocking the specular, LEED patterns are unable to resolve closer than $\sim$40%BZ_{SiC} to the specular leaving the long range order spots 6x6 (16.$\bar{6}$%BZ_{SiC}) and $6\sqrt{3}$ (9.623%BZ_{SiC}) poorly studied. The actual distance between these satellite spots and the SiC spot has recently been shown to be incommensurate by 0.5%BZ_{SiC} using x-rays[16] for a specially prepared buffer layer system[19], with the buffer layer lattice moving closer to commensurate when the 1st ML graphene forms[16].

Part of the difficulty of this system has been the proposed $6\sqrt{3}$ unit cell has 554 atoms at just the interface: 108 surface layer SiC silicon atoms, 108 surface layer SiC carbon atoms, and 336 carbon atoms in the buffer layer. Each additional layer of SiC adds 216 atoms, and the 1st ML graphene adds another 336 carbon atoms, making modeling a daunting task. As far as we know only one calculation of the band structure for the full $6\sqrt{3}$ structure has been performed with the assumption that the surface SiC atoms were locked to the bulk locations[15]. Considering the buffer layer is formed by Si desorption, it is not hard to imagine the number of Si atoms at the surface could vary depending on the temperature and time of desorption. Indeed, the semiconducting buffer layer requires a precise set of conditions for formation[16]. The surface structure, phases, and locations of the atoms in the graphene/buffer/SiC(0001) system is not resolved. The goal of this paper is to provide more information about the changing surface through SPALEED diffraction patterns by measuring many of the superstructure spots (both of the 6x6 and $6\sqrt{3}$ periodicity) with high wavevector resolution (0.3%BZ).

With the Spot Profile Analyzing Low Energy Electron Diffraction (SPALEED) we have studied the region close to the specular and observed strong 6x6 spots, but could not detect any spots associated with the first order $6\sqrt{3}$. We have also used SPALEED high resolution line profiles to resolve the spots associated with the $6\sqrt{3}$ pattern along the SiC{10} and Gr{10} directions. From 2D scans we identified four key bright satellite spots in the first Brillouin Zone which can be expressed as additions of the SiC{10} and Gr{10} reciprocal lattice vectors.

Additionally, we investigate a mysterious broad component in the diffraction patterns that is not present for the bare SiC(0001) surface or the surface covered with buffer layer, but quickly develops with graphene present. This broad component surrounding the (00) specular spot and the Gr{10} spots has been shown in the data in the literature for both the Gr/SiC[24] and

Gr/Ir(111)[25] systems, but has not received any attention. With our analysis we eliminate the typical sources of multiple components for diffraction spots related to surface morphology[26]. We propose it is a feature of graphene irrespective of substrate and possibly related to electron confinement within a perfect 2D layer of monolayer thickness.

6.3 Satellite spots of the buffer layer

Several challenges have contributed to the difficulty in understanding the growth of epitaxial graphene on SiC. The large unit cell, multiple layers involved in the growth, dense temperature and time dependent phase diagram, and multitude of satellite spots make this a challenge rivaling the structure of the Si(111)-7x7. Throughout the literature there have been many examples of the 2D diffraction pattern of the graphene on SiC system using LEED[1,13,22]. However, LEED is known for having poor resolution of the spots. SPALEED was developed to address this issue.

Figure 6.1 shows SPALEED diffraction patterns for a SiC(0001) sample that was covered with the buffer layer and had some regions of 1st ML graphene. The 2D scans in Figure 6.1(a,b) are the same scan taken at 193.8 eV with different labels. In Figure 6.1(a) the SiC spots are labeled in green while the graphene spots are labeled in red. The specular is located in the middle and the six bright spots surrounding it are at $\sim$1/6th of the SiC distance (again, the actual distance is under debate with a specially prepared sample showing a deviance by 0.5%BZ$_{SiC}$ from a spacing of 16.$\bar{6}$%BZ$_{SiC}$ using x-rays[16]). Throughout the paper we will use the term "6x6 spots" to refer to the 6-fold symmetric spots spaced $\sim$1/6th of the SiC lattice around any spot.

Figure 6.1(b) has pink lines added that are rotated 15° from the SiC{10} spots to show the pseudo six-fold symmetry of the surface (both SiC and graphene are three-fold symmetric with two domains possible). In the upper right the Gr(10) spot and the SiC(01) spot are labeled with an SiC(11) spot also circled. The symmetric spots to these are circled in the bottom left along with the key satellite spots for this diffraction pattern. The first key spot is circled in dark green and located at the SiC{7/6,0} location. It is brighter than the other 6x6 spots (50% brighter at 193.8 eV, there is an energy dependent component to this ratio)

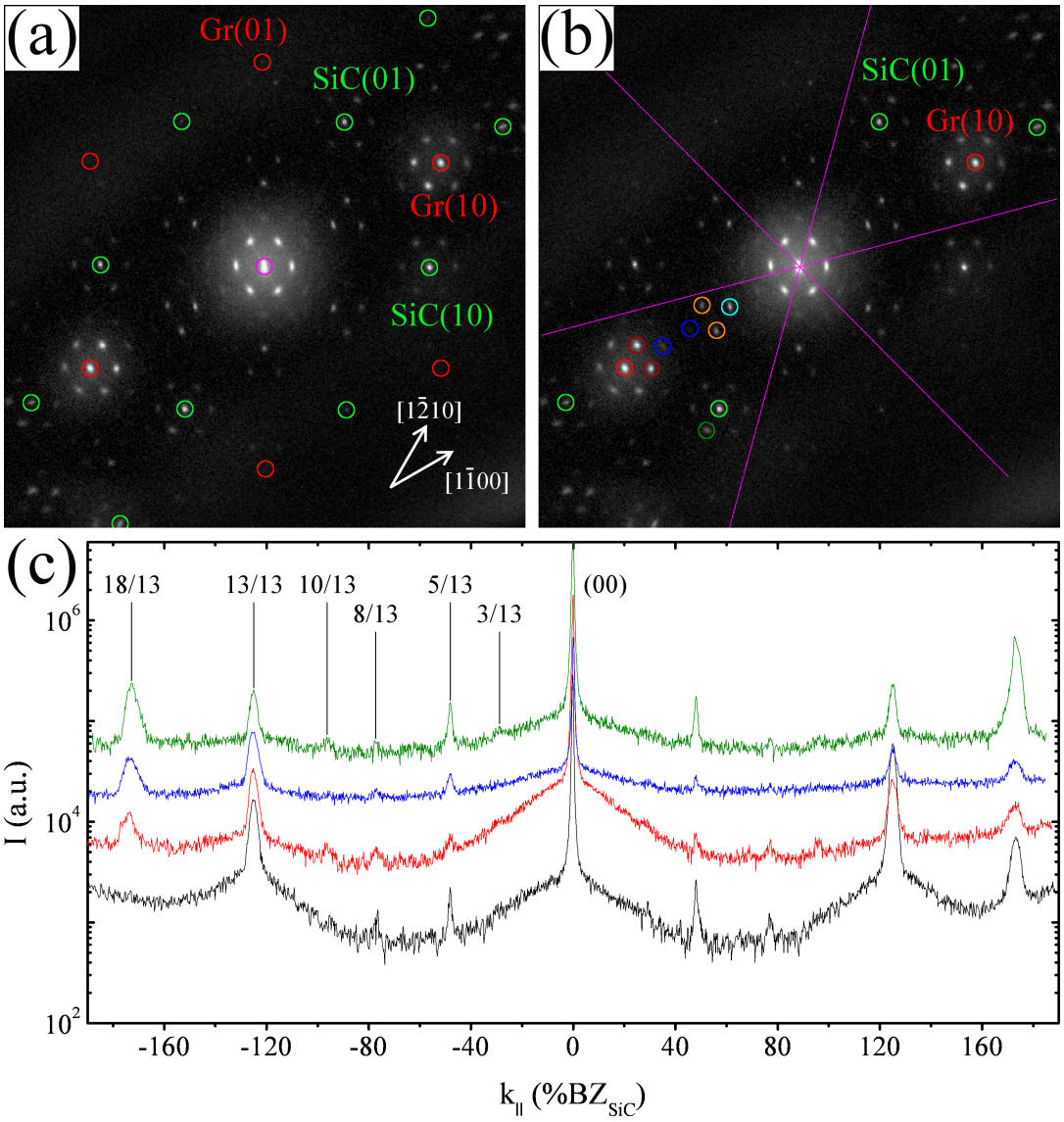

Figure 6.1 Diffraction patterns collected with SPALEED showing the satellite spots for a SiC(0001) sample covered with the buffer layer and including some regions of 1st ML graphene. (a,b) show the same background subtracted 2D SPALEED scan taken at 193.8 eV with different labels. In (a) all Gr spots and SiC spots are labeled in red and green respectively. The SiC(01) spot is in the [1$\bar{2}$10] direction and the Gr(10) spot is in the [1$\bar{1}$00] direction. In (b) key satellite spots have been highlighted. The pink lines in (b) are rotated 15° from SiC{10} so symmetric sections of the 2D scan can be compared. Due to non-isotropic non-linearity the upper right and lower left segments have the clearest view of spots that are far from the specular. The spots are discussed in text. (c) shows 1D scans taken along the graphene direction at 100 eV, 140 eV, 180 eV, and 220 eV from bottom to top with offsets of 10^x for x = 0.0, 0.4, 0.7, and 1.4 respectively.

surrounding the SiC{10} spots. The next spot is at the Gr{5/13,0} location and is circled in light blue. This spot is referred to as the $5/13^{th}$ spot and is one of the best indicators for the structures present on the surface. Located next to the $5/13^{th}$ spot are the "$5/13^{th}$ wings" in orange. There is a 6x6 pattern around all G{10} spots with the "graphene bright pair" three times brighter than the other graphene 6x6 spots (three times brighter at 193.8 eV, there is an energy dependent component to this ratio) and circled in dark red. The two spots circled in blue at Gr{8/13,0} and Gr{10/13,0} were also monitored due to them being along the often scanned graphene direction. Figure 6.1(c) shows 1D scans taken along the graphene direction at 100 eV, 140 eV, 180 eV, and 220 eV from bottom to top. The $k_{||}$ axis of the 1D profiles were rescaled with a function to correct for typical SPALEED non-linear dispersion with the SiC{11} spots providing a substrate reference spot. The Gr peak lines up with 13 times the $6\sqrt{3}$ lattice ($a_{SiC}/a_{Gr} = 3.08/2.46 = 1.25$, $13a_{6\sqrt{3}} = 1.251$). Referring to the $6\sqrt{3}$ lattice as $1/13^{th}$ the Gr spot, there are SPALEED spots located at 3/13, 5/13, 8/13, 10/13 and 18/13. The graphene spot is at 13/13, and the SiC(11) spot is at 18/13. Spots at 3/13, 8/13, and 10/13 are visible at only certain energies due to their low initial intensity and modulation with energy.

Based on the SPALEED data we have collected we have made the schematic model shown in Figure 6.2. All of the spots shown in panels (c-f) correspond to spots observed in our 2D scans. Throughout Figure 6.2(a-f) the specular is an off-center pink dot and the 6x6 surrounding the specular is in orange. There is a background of the $6\sqrt{3}$ lattice points in grey with length $9.623\%BZ_{SiC}$ rotated 30° from the SiC direction. Figure 6.2(a) shows the graphene spots in red and SiC spots in green. Colored lines are included to help visualize the reciprocal lattice. The spots are labeled according to their surface unit cells with 60° between the SiC(10) and SiC(01) spots. Note that this schematic includes multiple Brillouin zones with the SiC(20) spot directly right of the SiC(10) spot. Figure 6.2(b) has removed the labels and lattice lines while adding in the 6x6 patterns seen around SiC in grey and around Graphene in black. Similar to Figure 6.1(b), pink lines have been added rotated 15° counter clockwise from the SiC{10} directions to help focus on the repeating pseudo 6-fold symmetry.

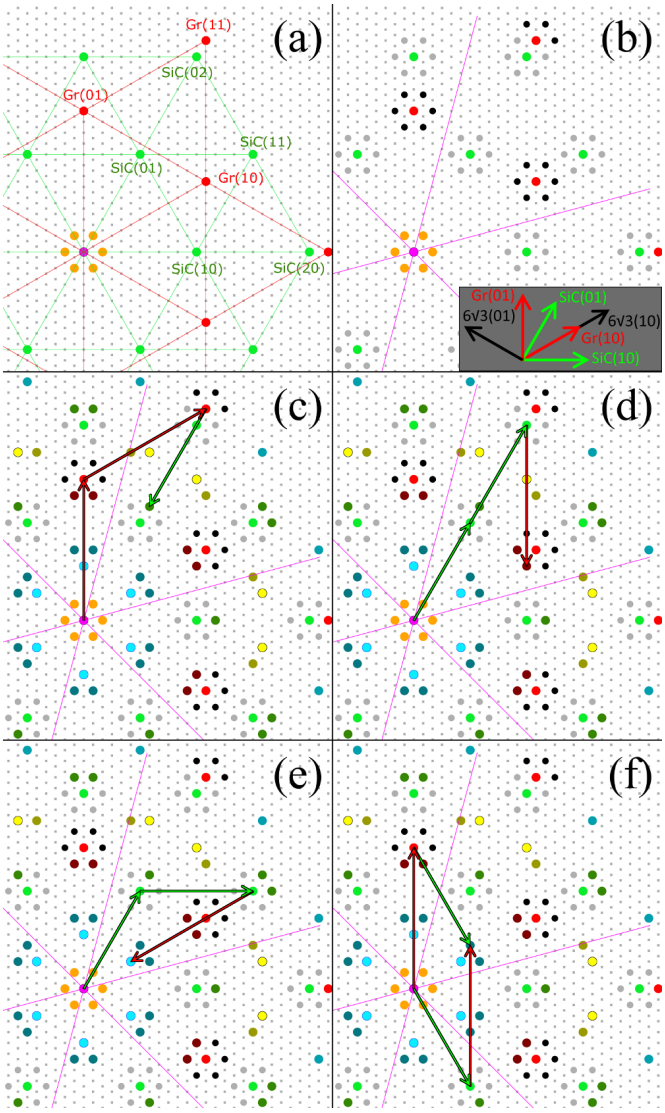

Figure 6.2 Model showing locations of diffraction spots fixed to a $6\sqrt{3}$ lattice. All models have a background of the $6\sqrt{3}$ spots in light grey with a length of 9.623%BZ_{SiC} rotated 30° from the SiC direction. In (a) the SiC spots are labeled in green and the graphene spots are labeled in red. Part (b) starts with the specular in pink and all SiC and graphene spots having a 6x6 pattern around them. Pink lines have been added in (b-f) similar to Figure 6.1(b) to show symmetry. The inset in (b) shows the directions of the lattices. In (c-f) a host of satellite spots have been added in various colors to help distinguish the symmetry and location. All of the colored spots added in (c-f) can be constructed through additions of the SiC and graphene lattice vectors, but four particular spots have the vector additions shown with SiC vectors as green arrows with length 100%BZ_{SiC} and graphene vectors as red arrows with length 125%BZ_{SiC}. Spots investigated are as follows: (c) SiC(7/6,0), (d) Graphene bright pair, (e) $5/13^{th}$, (f) $5/13^{th}$ wings.

Table 6.1 Summary of the spots observed in SPALEED with the Figure 6.2 panel that shows their location and their color in the Figure 6.2 model. The explicit basis vectors are listed for the surface lattices and the $6\sqrt{3}$ basis. For the $6\sqrt{3}$ basis, the contribution from each surface lattice in terms of the $6\sqrt{3}$ basis is listed with the total of the vectors in the final column. Each of these spots is visible in Figure 6.1(b).

Spot Name	Fig. 2 Panel	Fig. 2 Color	Surface Lattice Basis				6√3 Basis [6√3(10),6√3(01)]				
			Gr(10)	Gr(01)	SiC(10)	SiC(01)	Gr(10)	Gr(01)	SiC(10)	SiC(01)	Total
SiC{7/6,0}	2(c)	Dark Green	1	1	0	-1	[13,0]	[13,13]	[0,0]	[-12,-6]	[14,7]
Graphene Bright Pair	2(d)	Dark Red	0	-1	0	2	[0,0]	[-13,-13]	[0,0]	[24,12]	[11,-1]
5/13th	2(e)	Light Blue	-1	0	1	1	[-13,0]	[0,0]	[6,-6]	[12,6]	[5,0]
5/13th wings	2(f)	Dark Blue	0	1	1	-1	[0,0]	[13,13]	[6,-6]	[-12,-6]	[7,1]
SiC(11) Bright Pair	x	Dark Green	1	1	1	-1	[13,0]	[13,13]	[6,-6]	[-12,-6]	[20,1]
Yellow Spot	x	Yellow	1	0	-1	1	[13,0]	[0,0]	[-6,6]	[12,6]	[19,12]
Dark Yellow Spot	x	Dark Yellow	1	-1	-1	2	[13,0]	[-13,-13]	[-6,6]	[24,12]	[18,5]
Outer Dark Blue	x	Dark Blue	1	0	0	1	[13,0]	[0,0]	[0,0]	[12,6]	[25,6]
6x6	x	Gray/Black	1	1	0	-2	[13,0]	[13,13]	[0,0]	[-24,-12]	[2,1]

For Figure 6.2(c-f) we show lattice additions for the four bright spots from Figure 6.1(b) that are critical to the $6\sqrt{3}$ R30° pattern, but we want to emphasize that all spots shown are linear combinations of the SiC and Gr vectors of the form n_1SiC(10) + n_2SiC(01) + m_1Gr(10) + m_2Gr(01) = spot. For (c-f) graphene vectors with length 125%BZ_{SiC} are shown as red arrows while SiC vectors with length 100%BZ_{SiC} are shown as green arrows.

Table 6.1 shows explicit descriptions of each spot shown in Figure 6.2(c-f) and four spots outside the 1st Brillouin zone, including the one example of the required addition of vectors in both the surface lattice basis (using SiC or Gr) and the $6\sqrt{3}$ basis. Note that some of the spots are part of a symmetric pair. For the surface lattice basis, the SiC(10) direction is along the +x axis, and the SiC(01) direction is 60° counter-clockwise. The Gr(10) direction is 30° counter-clockwise from the SiC(10) direction and the Gr(01) is 60° from Gr(10). In the $6\sqrt{3}$ basis the $6\sqrt{3}$ lattice is rotated 30° counter clockwise from SiC(10) and has a length of 9.623%BZ_{SiC}. The $6\sqrt{3}$(01) direction is 120° counterclockwise from the $6\sqrt{3}$(10) direction, similar to a single plane of the hexagonal close packed crystal structure. These directions are summarized in the inset in Figure 6.2(b). We want to emphasize that every linear combination with low orders of n_i and m_j results in a clearly visible spot on the 2D SPALEED scan in Figure 6.1(b). However, the literature has not yet resolved why these particular spots are visible.

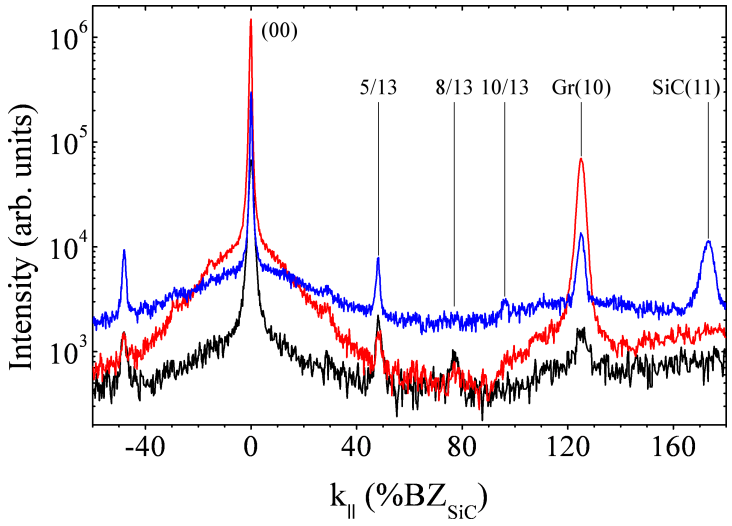

Figure 6.3 1D diffraction scans with SPALEED taken along [1$\bar{1}$00] (graphene direction). The black profile is from a buffer layer only sample taken at 62 eV. The red and blue profiles are taken from a buffer plus partial 1st sample (same as Figure 6.1) with red at 62 eV and blue at 200 eV. Spots are labeled with the Gr(10) spot at 13/13$^{\text{th}}$ and SiC(11) at 18/13$^{\text{th}}$. At 200 eV the beam probes ~4 layers.

Figure 6.3 shows 1D diffraction scans with SPALEED taken along [1$\bar{1}$00] (graphene direction) with corrections performed for the SPALEED non-linear distortion. The black profile is from a buffer layer only sample taken at 62 eV. The red and blue profiles are taken from a buffer plus partial 1$^{\text{st}}$ sample (same as Figure 6.1) with red at 62 eV and blue at 200 eV. In the buffer only sample (black) the 5/13$^{\text{th}}$ spot is more intense than the graphene spot. The buffer plus partial 1$^{\text{st}}$ layer graphene sample shows that the ratio of intensity is inverted when graphene is present on the sample. At 200 eV, which probes deeper layers on the surface, the 5/13$^{\text{th}}$ spot is on the same order of intensity as the Gr(10) spot and SiC(11) spot.

One of the key questions for this system is how to identify the condition or structure of the surface. The state of the graphene has been reported tracking the graphene spot[13], but this leaves out critical information concerning the state of the buffer layer. While direct comparisons of the intensities are not possible due to a lack of normalization, the persistent presence of the 5/13$^{\text{th}}$ spot and its larger intensity compared to other satellite spots throughout the buffer layer and graphene growth process mean it is the key spot to monitor. This information is essential to

identify the explicit growth widow the buffer layer enters the semiconducting phase[16] discovered recently.

6.4 Graphene's broad component in the diffraction pattern

Over the decades of LEED patterns developed for the graphene/buffer/SiC(0001) system there was a feature that due to the practice of showing a LEED image with a contrast range, was easy to overlook[1,6,9,13,17,18,22–25] and in some cases was difficult to spot without knowing what to look for. Even in SPALEED the effect is most noticeable near the specular–which is typically blocked by the electron gun in regular LEED–instead of surrounding the graphene spot that is visible in most of the earlier electron diffraction patterns.

With the SPALEED heavily relying on 1D profiles with a log scale a broad component surrounding the (00) specular and the Gr{10} spots is readily apparent in samples that contain graphene. The broad component has already been visible in Figure 6.1(c) and Figure 6.3. Depending on the status of the surface, the specular's broad component peak intensity is around 2% of the specular, but can contain over 50% of the integrated intensity of the specular when the specular is in-phase. The width of the specular broad component can be over 50%BZ_{SiC} corresponding to 2 lattice constants in real space. No such features have ever been seen on graphene so this is very puzzling. Plasmons are not the origin of this feature[25], and it is not visible to x-rays[27]. Additionally, this feature appears to be present in graphene on other surfaces[25]. This is the initial report of this feature, and we investigate the energy dependent behavior.

Figure 6.1(c) shows 1D scans at 100 eV to 220 eV for a buffer layer plus some 1^{st} ML graphene sample. These profiles show that the broad backgrounds around the specular and Gr spots have a strong energy dependence, with the broad backgrounds barely above the constant background at 220 eV (green). The black and red profiles in Figure 6.3 are from a buffer layer only sample and buffer plus some 1^{st} ML graphene sample respectively. Although they have not been calibrated for intensity, there is a clear change in the shape and relative ratios of the broad backgrounds surrounding the specular and graphene spot by comparing to the $5/13^{th}$ spot.

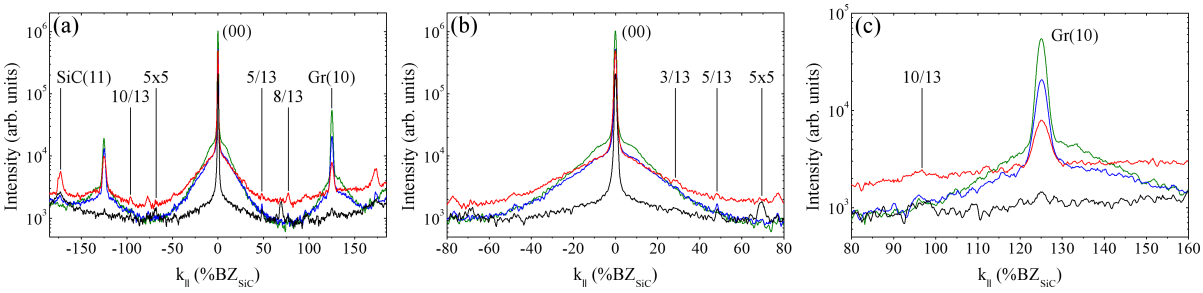

Figure 6.4 Examples of 1D scans along the $[1\bar{1}00]$ direction taken at 140/142 eV for various surfaces. The profiles come from samples with buffer layer (142 eV, black), buffer plus some ML graphene (142 eV, red), mostly 1 ML graphene (140 eV, blue), 1 ML graphene plus some 2 ML graphene (140 eV, green). The 2 eV difference makes a negligible difference in the profile. (a) shows the full profile, (b) zooms in on the specular's broad component, and (c) looks at the graphene spot. None of the profiles have had offsets applied. These profiles can be used to determine the exact condition of the surface and especially when the semiconducting buffer layer[16] recently discovered forms. *(Some data taken by H. Hattab.)*

1D scans taken along the $[1\bar{1}00]$ direction at energies of 140 eV or 142 eV were compared for surfaces at varying stages of buffer layer and graphene growth. Figure 6.4 shows profiles from a sample with pure buffer layer (142 eV, black), buffer plus some ML graphene (142 eV, red), mostly 1 ML graphene (140 eV, blue), and 1 ML graphene plus some 2 ML graphene (140 eV, green). Note that the 2 eV difference makes a negligible difference in the profile, but due to limited data in experimental runs the energy could not be matched exactly. Figure 6.4(a) shows the full profile, with Figure 6.4(b) zooming in on the specular and broad component, and Figure 6.4(c) examining the graphene spot. For these energies the $5/13^{\text{th}}$ is much weaker than other energies, and is barely visible in Figure 6.4(b). None of the profiles had offsets applied. While none of these profiles have been normalized for intensity or background, there are some distinct changes in the shape of the broad background. First, the buffer layer (black) has almost no broad component signal in Figure 6.4(b) and a very weak graphene spot in Figure 6.4(c). A sample with some ML graphene (red) shows a clear broad component around the specular and a clear graphene spot, but the broad component around the graphene spot is not clear. When the surface is mostly covered by ML graphene (blue) the broad component around the specular is still present, and a broad component around the graphene spot emerges. The addition of

some 2 ML graphene (green) appears to cause a change in shape of the broad component, with two shoulders appearing close to the specular around 10%BZ_{SiC}. At the graphene spot, it almost appears that the broad component is not centered on the Gr(10) spot.

To further investigate this broad background Reciprocal Space Maps (RSM) were created for the surface of 1 ML graphene plus some 2 ML graphene (green profile in Figure 6.4). A RSM is made by taking 1D scans of the same part of reciprocal space while changing the energy of the scan. These scans are then plotted with $k_{||}$ along the x-axis and energy on the y-axis with the intensity of the scan displayed by a color map. Figure 6.5(a) shows scans centered on the specular taken along the SiC direction. The 6x6 spots are visible at ~17%BZ_{SiC}. The major item of note from these scans is the specular and the broad background change intensity in phase with each other. Figure 6.5(b) shows the Gr($0\bar{1}$) spot with the scan along the [$1\bar{1}00$] direction (graphene direction). The maximums of intensity of the graphene spot are different than the specular, however the broad backgrounds around the graphene spot move in phase with the graphene spot, indicating the broad backgrounds around the graphene spot and specular have distinct energy profiles. It is key to note that as seen in lower left section of Figure 6.1(b), the graphene spot does have a broad background while the SiC spot lacks a broad background.

Typically when a diffraction spot has multiple components, these components have intensities that vary with electron energy and are related to the long range order and features on the surface. In particular, the narrow component of a spot can be compared to the total intensity of the narrow component and diffusely scattered electrons to understand the surface morphology, as reviewed in Horn-von Hoegen[26], Oura[28], and Figure 2.11 of this thesis. For vicinal surfaces the relative location of the spots shifts with energy. This can be eliminated as a possible source for the broad backgrounds due to their symmetry around their spot as energy changes. The typical G(S) analysis, where G is the ratio of the narrow component to total intensity and S is the phase of the electrons as described in equation 2.12, was completed for the sample with 1 ML graphene plus some 2 ML graphene. Figure 6.6(a) shows example fits for 1D scans centered on the specular and taken along the [$1\bar{2}10$] direction (SiC direction). The original data is in black, and the scan has been fitted with a constant background (red) and four Lorentzian 3-by-2 (L_{32}) functions corresponding to the narrow specular in blue (also referred to as (00)

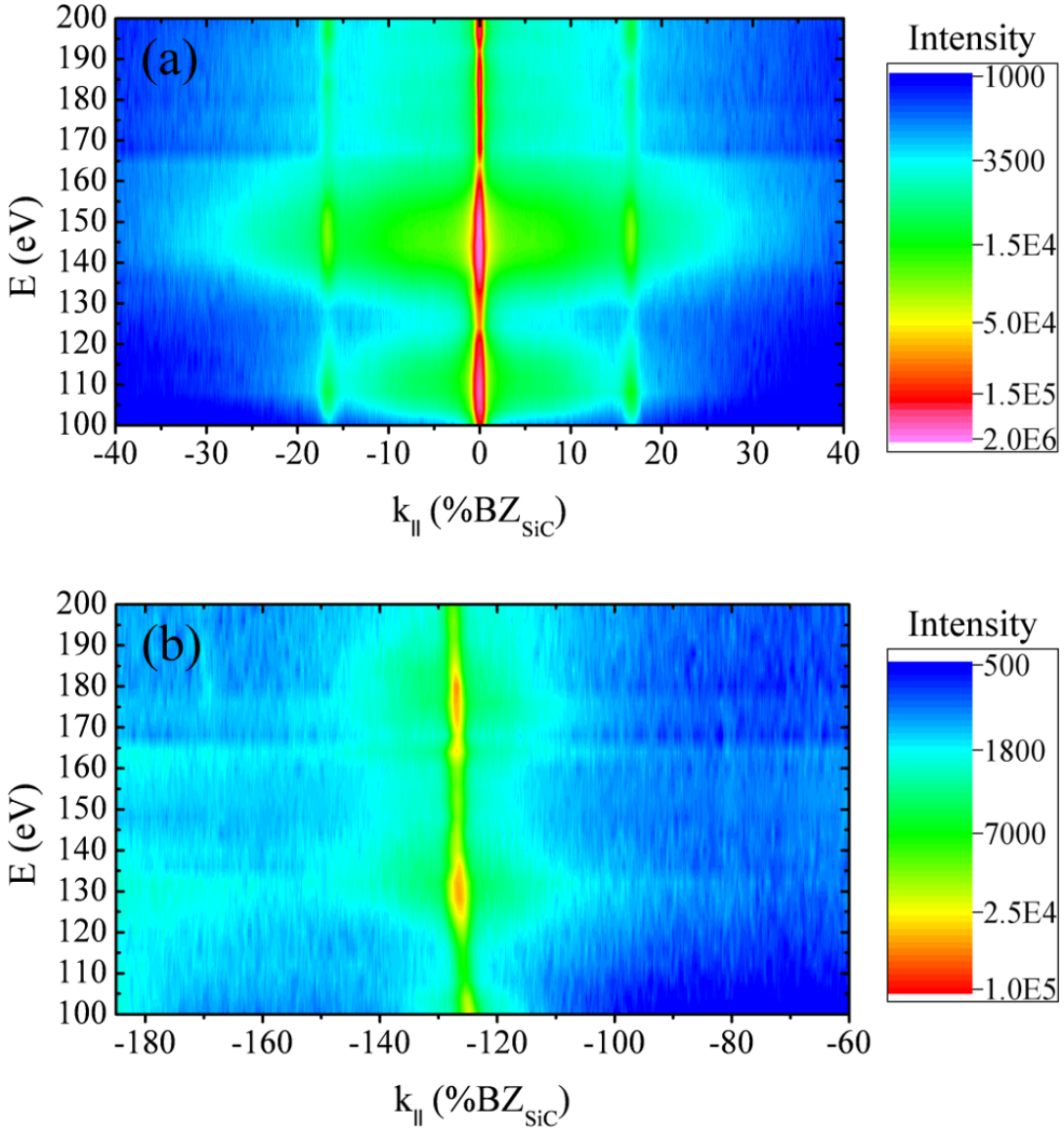

Figure 6.5 Reciprocal space maps constructed for the 1 ML graphene plus some 2 ML graphene system. (a) is along the $[1\bar{2}10]$ direction (SiC direction), (b) shows a graphene spot and is taken along the $[1\bar{1}00]$ direction (graphene direction). The rods show that the broad and narrow components intensity are correlated, in contrast from what expected based on the change of the scattering condition from constructive to destructive interference. *(Data taken by H. Hattab.)*

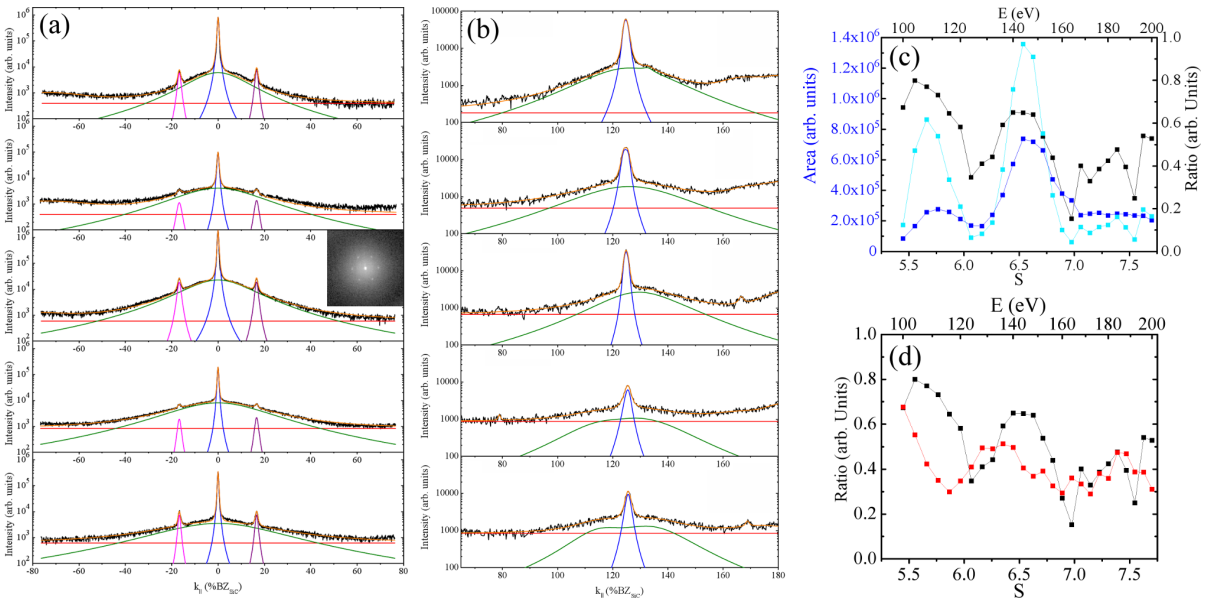

Figure 6.6 Analysis of the sample with 1 ML graphene plus some 2 ML graphene. Examples of 1D fits for the (a) specular and (b) graphene spot. (c) shows the G(S) ratio for the specular in black along with the area of the narrow specular in light blue and broad component in blue. (d) compares the G(S) ratio for the specular and the graphene spot. Both narrow and broad components are in phase as a function of scattering phase which rules out surface morphology (and variation of the diffraction interference condition from adjacent terraces) as the origin of the broad background. This broad background has only been seen on graphene and most likely related to its mesoscopic scale single layer uniformity. *(Data taken by H. Hattab.)*

specular), the broad specular in green, and the positive and negative SiC(1/6,0) spots (pink and purple) with the total fit in orange. The energies of the scans from top to bottom are 104 eV, 124 eV, 144 eV, 160 eV, and 200 eV. The 144 eV scan has an inset of a 2D diffraction pattern that is 100%BZ_{SiC} wide. 6.6(b) shows example fits for the graphene spot, with the scan along the $[1\bar{1}00]$ direction (graphene direction). The energies were the same as in (a). For the graphene spot multiple components were used to account more accurately for the full area of the diffuse intensity.

6.6(c) shows the areas of the fits from 6.6(a) with the area of the narrow specular in light blue and the area of the broad specular in blue. Similar to 6.5(a), the total intensity of these move in phase with each other. The phase S along the bottom x-axis is calculated using the

graphene step height with the original scan energies along the top axis. The G Ratio was calculated by dividing the area of the narrow specular by the sum of the narrow specular and broad specular. There are several unusual features resulting from this analysis. First, the G Ratio is in phase with the area of both the narrow component and broad/diffuse component. Typically the narrow component and broad/diffuse component are out of phase with each other. Second, the two local maximums in the G Ratio are at half integers. The only other height typical on the surface is SiC steps at 0.25 nm. The phase for this was also checked, and again the maximums did not line up with integers of the phase. In typical G(S) analysis the maximum of the G Ratio will always be at an integer number in the phase as seen in an example by Budde et al.[29] for Pb/Si(111). With this we conclude that the broad background is not originating from steps on the surface. 6.6(d) compares the G(S) for the specular in black and the graphene spot in red. Again, the graphene spot G(S) does not show any features typical of steps on the surface. The graphene ratio again is in phase with the area of both the graphene narrow and graphene broad (not shown). Finally, the G(S) of the graphene and specular are out of phase with each other, suggesting the broad component for each spot is independent of the other spots. It is still an open question as to the origin of the background which is only seen for graphene, but our quantitative study of the background is the first report for its correlation to the formation of perfect graphene.

6.5 Conclusions

The SiC(0001) system with buffer layer and 1st ML graphene has been investigated with SPALEED. The diffraction patterns show a wide variety of satellite spots with the literature debating the origin of these spots and the location of the atoms. The 5/13th spot has also been identified as a key spot to understand the status of the surface morphology. While studying the diffraction patterns a broad component surrounding the narrow specular and Gr{10} spots was observed to grow in parallel with graphene growth on the surface. The origin of this broad component is unknown, but through G(S) analysis steps on the surface have been eliminated as a possible source. This broad component also shows up in other graphene systems, and

we propose it is related to the 2D confinement of electrons in graphene, a proposal requiring further investigations.

References

[1] C. Berger, Z. Song, T. Li, X. Li, A. Y. Ogbazghi, R. Feng, Z. Dai, A. N. Marchenkov, E. H. Conrad, P. N. First, et al., The Journal of Physical Chemistry B **108**, 19912 (2004), URL http://dx.doi.org/10.1021/jp040650f. 6.2, 6.3, 6.4

[2] K. S. Novoselov, A. K. Geim, S. V. Morozov, D. Jiang, Y. Zhang, S. V. Dubonos, I. V. Grigorieva, and A. A. Firsov, Science **306**, 666 (2004), ISSN 0036-8075, URL http://science.sciencemag.org/content/306/5696/666. 6.2

[3] A. Obraztsov, E. Obraztsova, A. Tyurnina, and A. Zolotukhin, Carbon **45**, 2017 (2007), ISSN 0008-6223, URL http://www.sciencedirect.com/science/article/pii/S0008622307002965. 6.2

[4] A. Reina, X. Jia, J. Ho, D. Nezich, H. Son, V. Bulovic, M. S. Dresselhaus, and J. Kong, Nano Letters **9**, 30 (2009), URL http://dx.doi.org/10.1021/nl801827v.

[5] K. S. Kim, Y. Zhao, H. Jang, S. Y. Lee, J. M. Kim, K. S. Kim, J.-H. Ahn, P. Kim, J.-Y. Choi, and B. H. Hong, Nature **457**, 706 (2009), URL http://www.nature.com/nature/journal/v457/n7230/abs/nature07719.html. 6.2

[6] A. V. Bommel, J. Crombeen, and A. V. Tooren, Surface Science **48**, 463 (1975), ISSN 0039-6028, URL http://www.sciencedirect.com/science/article/pii/0039602875904197. 6.2, 6.4

[7] M. Hupalo, E. H. Conrad, and M. C. Tringides, Phys. Rev. B **80**, 041401 (2009), URL http://link.aps.org/doi/10.1103/PhysRevB.80.041401. 6.2

[8] F. Varchon, R. Feng, J. Hass, X. Li, B. N. Nguyen, C. Naud, P. Mallet, J.-Y. Veuillen, C. Berger, E. H. Conrad, et al., Phys. Rev. Lett. **99**, 126805 (2007), URL http://link.aps.org/doi/10.1103/PhysRevLett.99.126805. 6.2

[9] C. Riedl, C. Coletti, T. Iwasaki, A. A. Zakharov, and U. Starke, Phys. Rev. Lett. **103**, 246804 (2009), URL http://link.aps.org/doi/10.1103/PhysRevLett.103.246804. 6.2, 6.4

[10] J. D. Emery, B. Detlefs, H. J. Karmel, L. O. Nyakiti, D. K. Gaskill, M. C. Hersam, J. Zegenhagen, and M. J. Bedzyk, Phys. Rev. Lett. **111**, 215501 (2013), URL https://link.aps.org/doi/10.1103/PhysRevLett.111.215501. 6.2

[11] S. Goler, C. Coletti, V. Piazza, P. Pingue, F. Colangelo, V. Pellegrini, K. V. Emtsev, S. Forti, U. Starke, F. Beltram, et al., Carbon **51**, 249 (2013), ISSN 0008-6223, URL http://www.sciencedirect.com/science/article/pii/S0008622312007026. 6.2

[12] L. Vitali, C. Riedl, R. Ohmann, I. Brihuega, U. Starke, and K. Kern, Surface Science **602**, L127 (2008), ISSN 0039-6028, URL http://www.sciencedirect.com/science/article/pii/S0039602808006316. 6.2

[13] C. Riedl, U. Starke, J. Bernhardt, M. Franke, and K. Heinz, Phys. Rev. B **76**, 245406 (2007), URL https://link.aps.org/doi/10.1103/PhysRevB.76.245406. 6.2, 6.3, 6.3, 6.4

[14] W. Strupinski, K. Grodecki, P. Caban, P. Ciepielewski, I. Jozwik-Biala, and J. Baranowski, Carbon **81**, 63 (2015), ISSN 0008-6223, URL http://www.sciencedirect.com/science/article/pii/S0008622314008756. 6.2

[15] S. Kim, J. Ihm, H. J. Choi, and Y.-W. Son, Phys. Rev. Lett. **100**, 176802 (2008), URL https://link.aps.org/doi/10.1103/PhysRevLett.100.176802. 6.2

[16] M. Conrad, F. Wang, M. Nevius, K. Jinkins, A. Celis, M. Narayanan Nair, A. Taleb-Ibrahimi, A. Tejeda, Y. Garreau, A. Vlad, et al., Nano Letters **17**, 341 (2017), URL http://dx.doi.org/10.1021/acs.nanolett.6b04196. 6.2, 6.3, 6.3, 6.4

[17] K. V. Emtsev, F. Speck, T. Seyller, L. Ley, and J. D. Riley, Phys. Rev. B **77**, 155303 (2008), URL http://link.aps.org/doi/10.1103/PhysRevB.77.155303. 6.2, 6.4

[18] C. Riedl, C. Coletti, and U. Starke, Journal of Physics D: Applied Physics **43**, 374009 (2010), URL http://stacks.iop.org/0022-3727/43/i=37/a=374009. 6.2, 6.4

[19] W. A. de Heer, C. Berger, M. Ruan, M. Sprinkle, X. Li, Y. Hu, B. Zhang, J. Hankinson, and E. Conrad, Proceedings of the National Academy of Sciences **108**, 16900 (2011), URL http://www.pnas.org/content/108/41/16900.abstract. 6.2

[20] M. S. Nevius, M. Conrad, F. Wang, A. Celis, M. N. Nair, A. Taleb-Ibrahimi, A. Tejeda, and E. H. Conrad, Phys. Rev. Lett. **115**, 136802 (2015), URL http://link.aps.org/doi/10.1103/PhysRevLett.115.136802. 6.2

[21] S. Y. Zhou, G.-H. Gweon, A. Fedorov, P. First, W. De Heer, D.-H. Lee, F. Guinea, A. C. Neto, and A. Lanzara, Nature materials **6**, 770 (2007), URL http://www.nature.com/nmat/journal/v6/n10/abs/nmat2003.html. 6.2

[22] F. Owman and P. Mårtensson, Surface Science **369**, 126 (1996), ISSN 0039-6028, URL http://www.sciencedirect.com/science/article/pii/S0039602896009193. 6.2, 6.3, 6.4

[23] I. Forbeaux, J.-M. Themlin, and J.-M. Debever, Phys. Rev. B **58**, 16396 (1998), URL https://link.aps.org/doi/10.1103/PhysRevB.58.16396. 6.2

[24] T. Langer, H. Pfnür, H. W. Schumacher, and C. Tegenkamp, Applied Physics Letters **94**, 112106 (2009), URL http://dx.doi.org/10.1063/1.3100776. 6.2

[25] T. Langer, D. F. Förster, C. Busse, T. Michely, H. Pfnür, and C. Tegenkamp, New Journal of Physics **13**, 053006 (2011), URL http://stacks.iop.org/1367-2630/13/i=5/a=053006. 6.2, 6.4

[26] M. Horn-von Hoegen, Zeitschrift für Kristallographie **214**, 591 (1999). 6.2, 6.4

[27] W. A. de Heer, C. Berger, X. Wu, P. N. First, E. H. Conrad, X. Li, T. Li, M. Sprinkle, J. Hass, M. L. Sadowski, et al., Solid State Communications **143**, 92 (2007), ISSN 0038-1098, exploring grapheneRecent research advances, URL http://www.sciencedirect.com/science/article/pii/S0038109807002980. 6.4

[28] K. Oura, *Surf. Sci.: an introduction*, Advanced texts in physics (Springer, 2003), ISBN 9783540005452, URL http://books.google.com/books?id=HBFtQgAACAAJ. 6.4

[29] K. Budde, E. Abram, V. Yeh, and M. C. Tringides, Phys. Rev. B **61**, R10602 (2000), URL http://link.aps.org/doi/10.1103/PhysRevB.61.R10602. 6.4

CHAPTER 7. GROWTH OF FCC(111) DY MULTI-HEIGHT ISLANDS ON 6H-SIC(0001) GRAPHENE

M. T. Hershberger, M. Hupalo, P. A. Thiel, M. C. Tringides

A paper published in *Journal of Physics: Condensed Matter* **25**, 225005 (2013)

(Copyright Institute of Physics and IOP Publishing 2013.)

with an added section from *Carbon* **108**, 283 (2016)

and a paragraph with additional details added for this thesis chapter.

7.1 Abstract

Graphene based spintronic devices require an understanding of the growth of magnetic metals. Rare earth metals have large bulk magnetic moments so they are good candidates for such applications, and it is important to identify their growth mode. Dysprosium was deposited on epitaxial graphene, prepared by thermally annealing 6H-SiC(0001). The majority of the grown islands have triangular instead of hexagonal shapes. This is observed both for single layer islands nucleating at the top of incomplete islands and for fully completed multi-height islands. We analyze the island shape distribution and stacking sequence of successively grown islands to deduce that the Dy islands have fcc(111) structure, and that the triangular shapes result from asymmetric barriers to corner crossing.

7.2 Introduction

Graphene is a novel material studied extensively over the last 8 years[1–6]. Its unusual electronic structure holds the promise of future applications in many areas, especially for the new generation of ultrafast microelectronics. Its unique properties are related to its linear energy

dispersion with two Dirac cones touching at a single point, and its high electron mobility. Although these properties of clean graphene have been confirmed with many different techniques, open questions remain about the interaction of foreign atoms–especially metal atoms–with graphene. A strong interaction is necessary to ensure high quality metal contacts needed for device applications, but the interaction should not be strong enough to disturb the graphene electronic structure.

The interest in the growth of magnetic metals on graphene is motivated by more specific applications in spintronics. For example, graphene sandwiched between ferromagnetic layers can serve as a spin filter[7], while materials grown on graphene are predicted to have high magnetic anisotropy[8], or to be realizations of a novel Kondo effect[9]. Graphene itself may become magnetic[10], or may serve as a platform for high density arrays of magnetic islands for computer memory applications[11]. Electron correlations have been shown to modify the magnetic state of an adatom supported on graphene[12]. Doping with magnetic adatoms is an essential process to generate spin polarized electron current in graphene based devices.

Dysprosium (Dy), a rare earth metal, has been studied both theoretically and experimentally to determine its diffusion and adsorption energies on graphene[13]. Experimentally, scanning tunneling microscopy (STM) images were analyzed to measure the island density as a function of temperature T and coverage Θ. Density functional theory (DFT) was used to calculate the potential energy surface, and the nature of the Dy-C bond. These studies have shown that the Dy-C bond is strong and that Dy can have a large potential effect on the electronic structure of graphene.

Dy grows in an hcp bulk crystal structure. Submonolayer Dy films have been studied on W(110)[14]. There, it was shown that Dy can grow as islands with hexagonal shapes and an hcp crystal structure[15,16]. An earlier study using *in situ* resistivity and electron diffraction showed that Dy deposited on a glass substrate grows initially as an fcc crystal up to a thickness of 20 nm followed by a gradual structure change from fcc to hcp at higher thicknesses[17]. For a different rare earth, Eu, a new fcc-like phase was found after growth on Ta(110)[18] instead of the expected bcc(110) based on the Eu bulk structure.

The step heights of fcc(111) and hcp(0001) Dy are 0.289 nm and 0.283 nm, respectively. These values are so close that the two crystal structures cannot be easily distinguished on the basis of step or island heights. Similarly, the in-plane lattice constants for fcc(111) and hcp(0001) are $a_{111} = 0.354$ nm and $a_{0001} = 0.359$ nm respectively, so it would be difficult to distinguish the two 6-fold diffraction patterns with conventional low-energy electron diffraction.

In the current study, we use STM to identify the crystal structure of Dy islands on graphene, based upon the shapes of the Dy islands. The main conclusion from the current STM study will be that Dy on epitaxial graphene grows initially as fcc(111) islands. This is evident from the triangular shaped multi-height islands which form when the islands have fully completed layers suggesting thermodynamic reasons for the fcc crystal structure. When the islands are grown under different conditions (i.e. with stepwise coverage deposition) their top layers are incomplete, but still have triangular shapes which suggests that there must also be kinetic factors responsible for the triangular shapes.

Only Dy islands show these triangular shapes among the magnetic metals studied on graphene to date: Fe, Eu, and Gd[19]. The Dy growth on graphene is also special, because it relates to shapes of multi-height islands with faceted planes at their sides, rather than only to single layer islands nucleating on top of a bulk crystal as in Pt/Pt(111)[20], Co/Cu(111)[21], and Ir/Ir(111)[22]. It would be interesting to clarify the role of graphene since bulk-like hcp(0001) islands grow on W(110) or Mo(211)[23].

7.3 Experiment

The method of preparing graphene on 6H-SiC(0001) depends on how fast the annealing temperature of ~1500 K is reached and how long the crystal is kept at this temperature[24]. By controlling these two parameters, the fraction of single to bilayer graphene can also be controlled. The determination of the graphene layer thickness relies on two methods. (1) Domain height differences which can be expressed as a combination of an integer number of single step heights of graphene, 0.33 nm, and SiC, 0.25 nm. (2) The amplitude of the ($6\sqrt{3}$ x $6\sqrt{3}$) corrugation, with bilayer graphene having lower corrugation than single layer graphene for the same

tunneling voltage[24]. The samples used in the current experiments have 90% single and 10% bilayer domains. The average domain size is 200 nm.

Dy is deposited using a molecular beam source with the substrate at a temperature of ∼700 K[13] and with flux rates of 0.1-0.2 monolayers (ML)/min. The Dy source is degassed during the bakeout for several hours, so during deposition the pressure remains below 1.6 x 10^{-10} Torr. The number of ML of Dy is determined by finding the integrated island volume within a given area after correcting for the usual convolution tip effects. From the ratio of the integrated volume to the product of the island area selected and the Dy fcc step height, 0.289 nm, the Dy coverage is obtained in ML.

Dy grown on graphene at room temperature and flux rates of more than 0.5 ML/min produces irregular, kinetically driven small islands. In this study Dy is grown at elevated temperatures up to 700 K to improve island crystallinity. No coarsening is observed at 700 K on the time scale of ∼1 h, but the aspect ratio of the islands–the ratio of height to lateral size–increases. The majority of the STM images are taken at room temperature, so they reflect a frozen morphology produced at the higher deposition temperature.

7.4 Results

Figure 7.1 shows Dy deposited continuously on graphene at ∼660 K at three different coverages: 0.29, 0.94, and 1.36 ML. The corresponding island densities are 5.5 x 10^{-4} islands/nm^2; 1.5 x 10^{-3} islands/nm^2, and 1.1 x 10^{-3} islands/nm^2. The growth mode is three-dimensional (3D) and the driving force is the low ratio ($E_a/E_c = 0.5$) of the adsorption energy ($E_a = 1.47$ eV) of Dy on graphene, to the bulk Dy bulk cohesive energy ($E_c = 2.94$ eV) as discussed in[13]. This implies that the ratio of the rates of Dy adsorption on graphene and adsorption on a bulk-like Dy island is 10^{-11} at 700 K, thus favoring 3D growth. In the experiment, we observe islands ∼10 layers high even for small deposited amounts, as low as ∼2 ML. This 3D growth is a general feature for all the metals grown on graphene[11,13,19].

For the three Dy coverages, the average island heights are 6.9 ± 1.5 layers, 7.1 ± 1.2 layers, and 8.4 ± 1.7 layers. The average areas are 84 ± 69 nm^2; 95 ± 55 nm^2; 159 ± 112 nm^2 respectively. In continuous deposition experiments the islands grow with fully completed

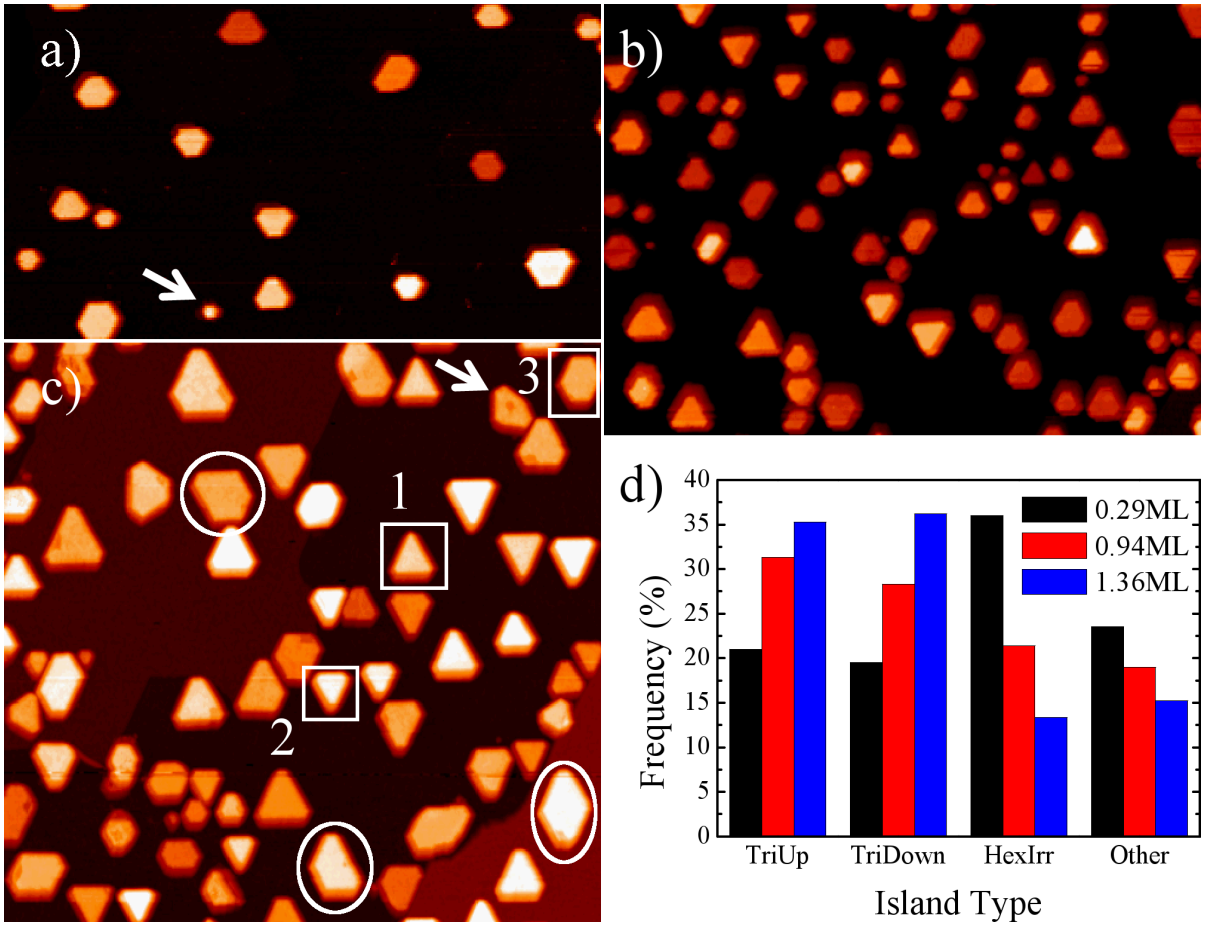

Figure 7.1 Dy islands grown on epitaxial graphene at 660 K after continuous deposition, with coverages of (a) 0.29 ML, (b) 0.94 ML, (c) 1.36 ML. The corresponding areas are 250 x 150 nm^2; 250 x 180 nm^2, and 250 x 240 nm^2. The majority of the islands have triangular shapes with equal number of islands pointing in opposite directions. These are multi-height islands with perfectly completed tops. (d) Island shape histogram with the frequency of the three main categories and the shapes that are difficult to classify. As the coverage increases the fraction of triangularly shaped islands increases.

layers and their sides are perfect low index planes. For hcp(0001) islands the six facet planes are equivalent with the $\{1\bar{1}01\}$ orientation. For fcc(111) islands the facet plane orientation alternates between the {111} and {100} orientations. The in-plane island orientation with respect to the graphene unit cell shows that the island sides are normal to the graphene (1x1) unit cell direction.

The shapes of the islands were classified into three main categories as seen in Figure 7.1(c). Categories 1 and 2 include triangular shaped islands named TriUp and TriDown depending on the direction they are pointing, and category 3 is the Irregular Hexagon (HexIrr). Although both Gd and Dy have hcp bulk structure and Gd forms exclusively hexagonally symmetric islands on graphene after annealing to 1000 K[19], Dy shows predominantly triangular island shapes.

Categories 1 and 2 also include 'almost triangular' shaped islands. Examples of these 'almost triangles' are circled in Figure 7.1(c). They are rhombic shapes indicating merging triangular islands and truncated islands with one or two corners missing. Diamond shaped islands were counted both in the TriUp and TriDown categories. Islands that did not fit into the three categories were labeled 'Other'. This included the few islands that did not have six symmetric sides like the island with an arrow in Figure 7.1(c), and islands that were too small to distinguish between hexagonal and triangular shapes like the island with an arrow in Figure 7.1(a).

Figure 7.1(d) compares the relative frequency of the different types of islands. With increasing Θ the relative number of triangular islands increases. This suggests that the triangular islands start as hexagonal, and as they grow they change into triangular ones.

Next we study the evolution of island shapes with Θ in stepwise deposition experiments, i.e., Dy is deposited in three smaller doses, with the first coverage being 0.03 ML. This defines the initial island density, and is especially influential because of the tendency of the Dy adatoms to move to higher layers once they approach an island already nucleated. (As noted, the adsorption energy E_a for Dy on graphene is very low.) After this, 0.50 and 1.02 ML total coverages are deposited. The initial island density is 1.5 x 10^{-4} islands/nm^2, and it then increases to 3.9 x

10^{-4} islands/nm^2 and 3.3 x 10^{-4} islands/nm^2. The density for 1.02 ML of Figure 7.2(b) is 4.5 times lower than the island density of Figure 7.1(b) at $\Theta = 0.94$ ML.

Growth during continuous deposition (Figure 7.1) is very different from growth during stepwise deposition (Figure 7.2). Instead of growing 3D islands with the top layer complete, approximately 60% of the islands in Figure 7.2(a) have multiple incomplete layers exposed at the top. In Figure 7.2(a) the average size of the islands with completed tops (similar to the ones in Figure 7.1) is 145 $\pm$ 92 nm^2 while the layer islands with incomplete tops have an average size of 265 $\pm$ 151 nm^2. In Figure 7.2(b) 70% of the islands have incomplete top layers with an average base area of 584 $\pm$ 252 nm^2 while the islands with completed top layers have an average area of 352 $\pm$ 242 nm^2. The larger projected area of the islands with incomplete tops versus islands with completed tops shows that they are more effective in capturing adatoms. Since the diffusing adatoms aggregate to the larger islands, this results in a smaller number of new islands nucleating and accounts for the lower island density when compared to the continuous deposition experiments of Figure 7.1. At the same time more atoms are necessary to cover the larger area of a given layer, which accounts for the incomplete stacked layers. The 1D line scan shown in Figure 7.2(b) and displayed in Figure 7.2(c) is used to measure the island height from the height increments, marked at the plateau, of the exposed edges of the incomplete top layers.

7.5 Discussion

As already discussed the completed multi-height triangular islands of Figure 7.1 suggest that the grown Dy islands are fcc(111) because the side planes must be inequivalent, so three of the side planes become extinct[25]. The results of the stepwise deposition experiments with incomplete island layers shown in Figure 7.2 suggest that growth of these islands is also kinetically limited and that the islands do not attain their equilibrium shapes under the stepwise deposition conditions. The very small, initial 0.03 ML deposition makes the island density lower than that in Figure 7.1, even at comparable coverage, because the islands formed at this early stage provide sites to which the atoms deposited at the next two doses diffuse and aggregate[26]. Dy has relatively high mobility on graphene at 700 K.

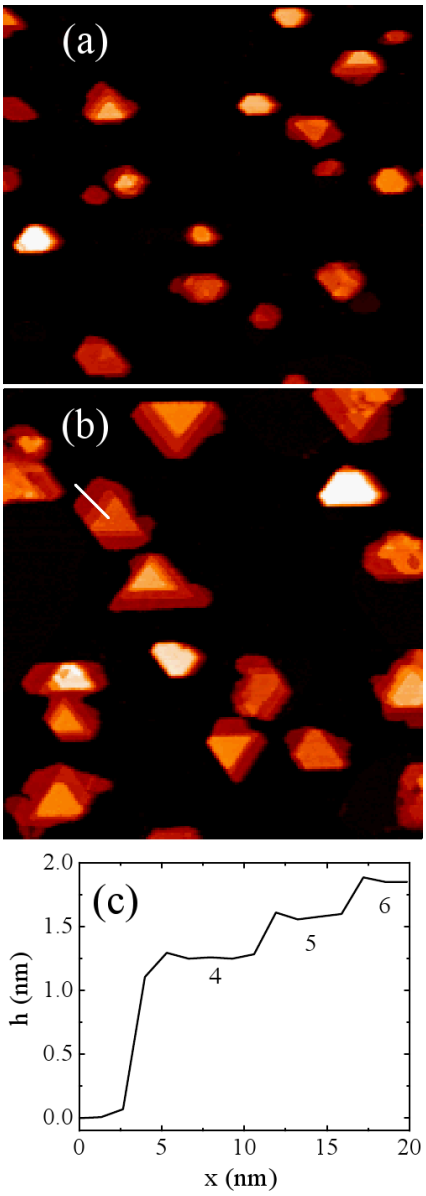

Figure 7.2 Dy deposition on graphene in stepwise deposition experiments following an initial 0.03 ML seeding deposition, for total coverages of (a) 0.50 ML and (b) 1.02 ML at 670 K. Images areas are (a) 185 x 170 nm^2 and (b) 185 x 200 nm^2. The island density is lower and the base of the islands is larger when compared to the density and base of the islands of Figure 7.1. The initial seeding deposition determines the nucleation sites and accounts for the larger capture zone of the islands formed, which results in islands with incomplete top layers. In cases where a sequence of stacked triangular shaped islands is seen the islands point to the same direction, which shows that the islands are fcc(111). (c) 1D scan showing the heights of the exposed layers, the number showing the layer height.

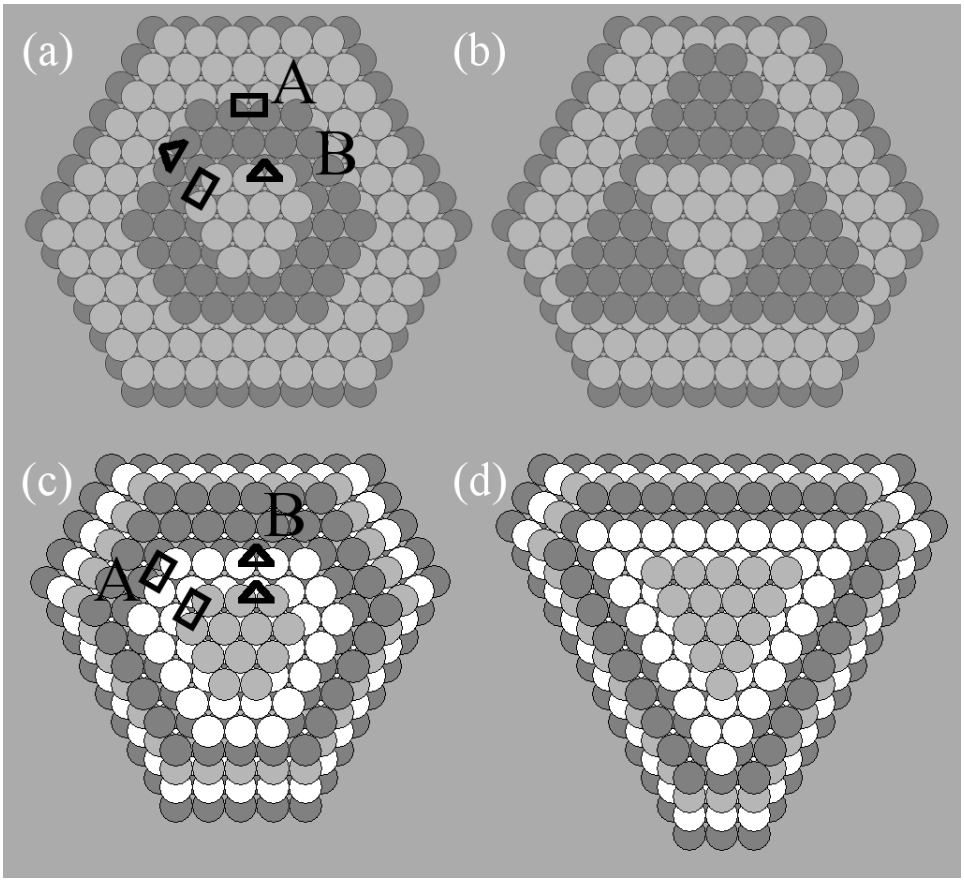

Figure 7.3 Models of incomplete island nucleation on the top layers. The edges of the single layer islands have two types of steps–A and B–distinguished by the different microfacets: black rectangles for A steps and black triangles for B steps. (a) and (b) show the case of hcp(0001) crystal growth with the triangular island direction in successive layers alternating. Fcc(111) triangular islands shown in (c) and (d) point in the same direction at all layers.

The Dy islands form predominantly because of uphill atom flux to higher layers, caused by the lower adsorption energy E_a of metals on graphene, with a smaller contribution from atoms directly deposited on top. Since the incoming Dy atoms from the surrounding area have the tendency to move uphill, the lower incomplete layers of the islands of Figure 7.2 do not receive enough atoms to fill the layers completely up to their edges before new layers form on top.

Figure 7.3 shows a schematic of the stacking of hcp(0001) layers in (a,b) and fcc(111) layers in (c,d). There are two types of edges, and their atomic arrangement is represented by the different microfacets, denoted as black rectangles (called A edges) and as black triangles

(called B edges). The A edge for fcc(111) islands with fully complete layers develops into an fcc(100) plane, while the B edge develops into an fcc(111) plane. For a single layer nucleating on top of an fcc(111) island the two step types will keep their direction unchanged as more layers are built: the A edges will be in the same directions and the B edges will be at 60°. On the other hand, for hcp(0001) multi-height islands the six facet planes are equivalent $\{1\bar{1}01\}$. For single layer islands nucleating at the top of an hcp(0001) island, the same type of edges (A- and B-type) are present as for fcc(111) islands. Figure 7.3(a) shows that an edge in a given direction of a newly nucleated hcp(0001) island will alternate between A-type and B-type as successive layers are deposited, which implies that for triangular shaped hcp(0001) islands (because one of the inequivalent step edges is favored), the direction they are pointing would alternate with each layer.

In systems studied in the literature which show almost perfect triangular island shapes similar to ours, Monte Carlo simulations[27,28] have shown that anisotropy in corner crossing determines the extreme triangular shapes. There are two other candidate mechanisms–anisotropy in edge sticking and anisotropy in edge diffusion–but when these and corner crossing are both present corner crossing is often the dominant process that controls the island shape. More specifically, in simulations using barriers relevant to the Al/Al(111) system calculated with density functional theory it was found that the barriers for atoms to cross the island corner clockwise versus counterclockwise differ by 0.17 eV at 160 K, and perfect triangular shapes result. For the Co/Cu(111) system, the combined effect of differences in edge diffusion and a corner crossing barrier of 0.31 eV at 300 K[28] also results in perfect triangular shapes. The two simulations have an anisotropic corner crossing ratio of $\sim 10^5$ for the atoms moving from one island edge around the corner to the adjacent edge. It was argued that the net effect is for the corner to serve as a reflecting wall for the approaching atoms from the direction with the higher barrier, thus making the atom population on the incoming step higher, resulting in this step growing faster and at the end being eliminated. Similar barriers as those found in[28] can be applicable to the growth of the Dy triangular nano-islands, since despite the higher growth temperature of 700 K, using the barriers of[27,28] the ratio between the two rates to cross a corner in the two opposite directions will still be high, 1.4 x 10^2.

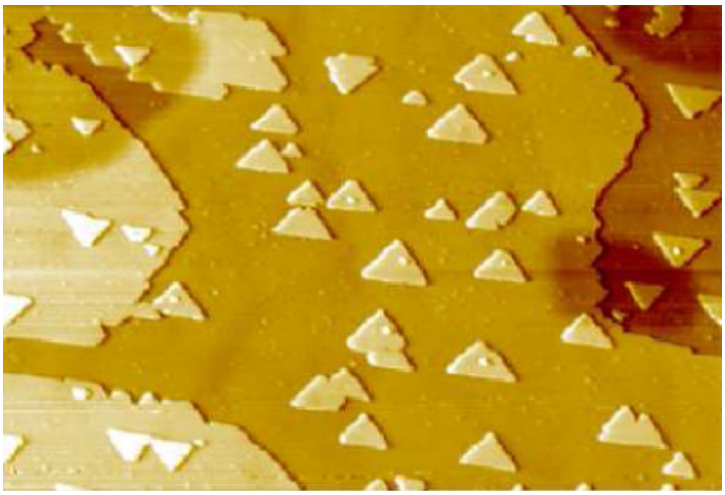

Figure 7.4 Mg(0001) 15 ML film (grown on W(110)) after deposition of additional 0.1 ML of Mg at 135 K with 0.017 ML/s flux rate. Image size is 250 x 170 nm^2. The triangularly shaped single layer Mg islands, caused by extreme corner crossing anisotropy, alternate in direction with increasing layer height, but within each terrace they point along the same direction with essentially ∼100% frequency, as expected for hcp(0001) islands.

As seen in Figure 7.1 and Figure 7.2 the number of islands pointing in opposite directions are essentially the same and the islands keep this preferred direction as their height increases. This is expected for fcc(111) islands since there are two possible stackings: ABCABC and ACBACB. Both stackings should have the same probability. Dy on graphene is a heteroepitaxial system and both types of stackings nucleate initially with equal probability, because the graphene substrate structure is not correlated to the growing metal island structure.

In contrast, the homoepitaxial growth of Mg on Mg(0001) films grown on W(110) seen in Figure 7.4 also results in perfect single layer triangular Mg islands nucleating instead of hexagonal islands as expected from the Mg bulk hcp structure. However, the newly nucleated Mg(0001) islands alternate in the direction they point to with each new layer, in agreement with the schematics of Figure 7.3(a,b)[23]. Their shape is also a result of extreme corner crossing anisotropy. For hcp(0001) islands, only one stacking is possible and each terrace should have triangular shaped islands pointing 100% in either up or down direction. Terraces differing by one layer should also have 100% of the islands reversed by 180° from the orientation in the

previous layer. This is exactly what is observed for homoepitaxial Mg/Mg(0001) growth in Figure 7.4.

7.6 Island and graphene alignment

The following paragraph and Figure 7.5 is derived from work published in *Carbon* **108**, 283 (2016)[29]

With the Dy islands confirmed as fcc, the STM was used to determine the relative orientation of the Dy islands with the graphene lattice in Figure 7.5. Figure 7.5(a) shows a section of Figure 7.1(c). Figure 7.5(b) zooms in on the island with a square around it in Figure 7.5(a), then Figure 7.5(c) zooms in on the edge of the island in Figure 7.5(b). Figure 7.5(c) has been differentiated so the holes of the graphene appear as bright dots and the edge of the island is pure black. With an fcc crystal the lowest energy plane is expected to be a close packed direction. Figure 7.5(c) shows the close packed direction is oriented 90° from the direction of graphene lattice, which by symmetry is equivalent to 30° from the graphene direction, or the Dy is parallel to the SiC lattice in the $\{1\bar{2}10\}$ direction. The model in Figure 7.5(d) shows the proposed relative orientation of the island with the graphene lattice. The results from the STM are in agreement with diffraction studies of the Dy/Gr/SiC system[29].

7.7 Charge transfer role in hexagonal system phase changes

The following paragraph is additional information added for this thesis chapter.

There has been wide variety of studies of hexagonal systems investigating the transition between various stacking orders. The general premise is there are layers of close-packed atoms with three possible sites–A, B, and C–and faulting due to dislocated planes can cause phase transitions. The hexagonal close-packed structure follows the pattern AB,AB... and the face centered cubic structure along the {111} direction follows ABC,ABC... with various other stacking possibilities existing. The transitions between these structures have traditionally been studied under high pressures and high temperatures. In particular, noble gases have been studied experimentally and theoretically[30–32]. Both the Ar[30] and Xe[31] transitions invoke the

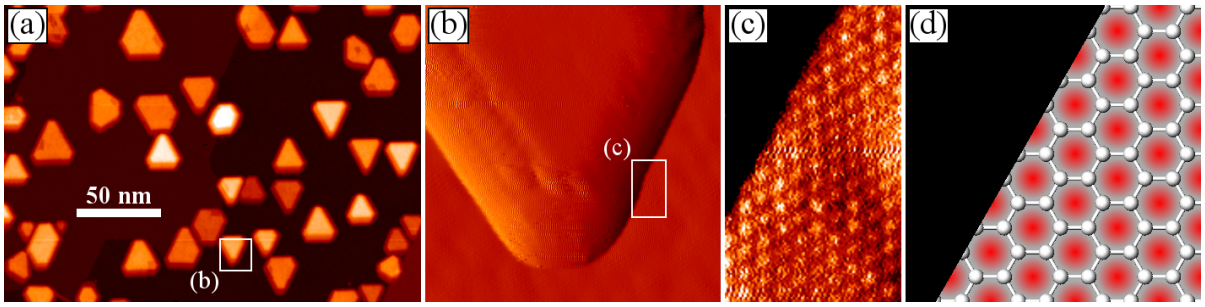

Figure 7.5 Series of STM images showing the relative orientation of the Dy islands compared to the graphene lattice. (b) is an island from (a), (c) zooms in on the edge of the island in (b). (c) has been differentiated so the centers of the graphene rings appear as bright dots. The black part of (c) is the edge of the island. (d) shows a schematic with the edge of a Dy island as black, the carbon atoms and bonds for graphene in white, and the centers of the graphene holes as red dots. (a) 247 x 175 nm^2 (b) 18.3 x 18.3 nm^2 (c) 2.1 x 3.5 nm^2

hybridization between the *sp* and *d* bands as the source for the transition between hcp and fcc. An extensive review article covering multiple systems at high temperature and pressure notes that from several studies of bulk Rare Earth metals that the transition between hcp, Sm-type, dhcp, fcc, and dfcc is due to electron transfer in the valence shells[33]. Charge transfer calculations have been carried out for numerous other metals on graphene[34], and calculations for single Dy atoms absorbed on a 4 x 4 graphene supercell suggest a charge transfer of $0.76e^-$ per Dy atom[13]. With this context one possible explanation for the initial Dy fcc growth is charge transfer with the graphene, although the charge transfer effect would be localized at the graphene-substrate interface. The results that the crystal structure transitioned from fcc to hcp as the film increased to multi-layer thickness[17] could be explained by thicker films screening the number of electrons transferred for thicker layers, allowing the typical bulk structure to resume.

7.8 Conclusions

It has been reported in the literature that several epitaxially grown metal/metal systems exhibit islands that do not have the hexagonal shapes expected from the six-fold symmetry of the bulk metal, but instead they have either asymmetric hexagonal shapes or, in a few cases,

perfect triangular shapes. The majority of these experiments involve single or bilayer islands nucleating on top of a macroscopic single crystal surface or on top of very large islands[35]. The Dy/graphene system distinguishes itself from both of these categories with multi-height triangularly shaped islands that have the fcc(111) rather than hcp(0001) crystal structure. Single layer triangular islands observed on incomplete layers on Dy islands grown in stepwise deposition experiments suggest that in addition to the thermodynamic reasons, kinetic ones must also be responsible for the island triangular shapes. The kinetic reasons most likely are related to a corner crossing barrier anisotropy. It would be interesting to investigate experimentally and theoretically the magnetic moment and magnetic domain distribution in these fcc(111) Dy islands to compare them to the corresponding properties of normal hcp(0001) Dy islands.

7.9 Acknowledgements

This work was supported by the Office of Science, Basic Energy Sciences, Materials Sciences and Engineering Division of the US Department of Energy (USDOE), under Contract No. DE-AC02-07CH11358 with the US Department of Energy.

References

[1] C. Berger, Z. Song, T. Li, X. Li, A. Y. Ogbazghi, R. Feng, Z. Dai, A. N. Marchenkov, E. H. Conrad, P. N. First, et al., The Journal of Physical Chemistry B **108**, 19912 (2004), URL http://dx.doi.org/10.1021/jp040650f. 7.2

[2] K. S. Novoselov, A. K. Geim, S. V. Morozov, D. Jiang, Y. Zhang, S. V. Dubonos, I. V. Grigorieva, and A. A. Firsov, Science **306**, 666 (2004), ISSN 0036-8075, URL http://science.sciencemag.org/content/306/5696/666.

[3] A. H. Castro Neto, F. Guinea, N. M. R. Peres, K. S. Novoselov, and A. K. Geim, Rev. Mod. Phys. **81**, 109 (2009), URL http://link.aps.org/doi/10.1103/RevModPhys.81.109.

[4] D. L. Miller, K. D. Kubista, G. M. Rutter, M. Ruan, W. A. De Heer, M. Kindermann, P. N. First, and J. A. Stroscio, Nature Physics **6**, 811 (2010), URL http://www.nature.com/nphys/journal/v6/n10/abs/nphys1736.html.

[5] J. Wintterlin and M.-L. Bocquet, Surface Science **603**, 1841 (2009), ISSN 0039-6028, URL http://www.sciencedirect.com/science/article/pii/S003960280900079X.

[6] H. Hattab, A. T. N'Diaye, D. Wall, C. Klein, G. Jnawali, J. Coraux, C. Busse, R. van Gastel, B. Poelsema, T. Michely, et al., Nano Letters **12**, 678 (2012), URL http://dx.doi.org/10.1021/nl203530t. 7.2

[7] V. M. Karpan, G. Giovannetti, P. A. Khomyakov, M. Talanana, A. A. Starikov, M. Zwierzycki, J. van den Brink, G. Brocks, and P. J. Kelly, Phys. Rev. Lett. **99**, 176602 (2007), URL http://link.aps.org/doi/10.1103/PhysRevLett.99.176602. 7.2

[8] C. Vo-Van, Z. Kassir-Bodon, H. Yang, J. Coraux, J. Vogel, S. Pizzini, P. Bayle-Guillemaud, M. Chshiev, L. Ranno, V. Guisset, et al., New Journal of Physics **12**, 103040 (2010), URL http://stacks.iop.org/1367-2630/12/i=10/a=103040. 7.2

[9] B. Uchoa, T. G. Rappoport, and A. H. Castro Neto, Phys. Rev. Lett. **106**, 016801 (2011), URL http://link.aps.org/doi/10.1103/PhysRevLett.106.016801. 7.2

[10] H. Sevinçli, M. Topsakal, E. Durgun, and S. Ciraci, Phys. Rev. B **77**, 195434 (2008), URL http://link.aps.org/doi/10.1103/PhysRevB.77.195434. 7.2

[11] S. M. Binz, M. Hupalo, X. Liu, C. Z. Wang, W.-C. Lu, P. A. Thiel, K. M. Ho, E. H. Conrad, and M. C. Tringides, Phys. Rev. Lett. **109**, 026103 (2012), URL http://link.aps.org/doi/10.1103/PhysRevLett.109.026103. 7.2, 7.4

[12] A. N. Rudenko, F. J. Keil, M. I. Katsnelson, and A. I. Lichtenstein, Phys. Rev. B **86**, 075422 (2012), URL http://link.aps.org/doi/10.1103/PhysRevB.86.075422. 7.2

[13] M. Hupalo, X. Liu, C.-Z. Wang, W.-C. Lu, Y.-X. Yao, K.-M. Ho, and M. C. Tringides, Advanced Materials **23**, 2082 (2011), URL http://onlinelibrary.wiley.com/doi/10.1002/adma.201100412/full. 7.2, 7.3, 7.4, 7.7

[14] J. Kołaczkiewicz and E. Bauer, Surface Science **175**, 487 (1986), ISSN 0039-6028, URL http://www.sciencedirect.com/science/article/pii/0039602886900087. 7.2

[15] H. Li, D. Tian, J. Quinn, Y. S. Li, S. C. Wu, and F. Jona, Phys. Rev. B **45**, 3853 (1992), URL http://link.aps.org/doi/10.1103/PhysRevB.45.3853. 7.2

[16] S. Krause, L. Berbil-Bautista, T. Hänke, F. Vonau, M. Bode, and R. Wiesendanger, EPL (Europhysics Letters) **76**, 637 (2006), URL http://stacks.iop.org/0295-5075/76/i=4/a=637. 7.2

[17] V. Kaul, B. Bist, and O. Srivastava, Thin Solid Films **30**, 65 (1975), ISSN 0040-6090, URL http://www.sciencedirect.com/science/article/pii/0040609075903053. 7.2, 7.7

[18] C. G. Olson, X. Wu, Z.-L. Chen, and D. W. Lynch, Phys. Rev. Lett. **74**, 992 (1995), URL http://link.aps.org/doi/10.1103/PhysRevLett.74.992. 7.2

[19] M. Hupalo, S. Binz, and M. C. Tringides, Journal of Physics: Condensed Matter **23**, 045005 (2011), URL http://stacks.iop.org/0953-8984/23/i=4/a=045005. 7.2, 7.4, 7.4

[20] T. Michely, M. Hohage, M. Bott, and G. Comsa, Phys. Rev. Lett. **70**, 3943 (1993), URL http://link.aps.org/doi/10.1103/PhysRevLett.70.3943. 7.2

[21] J. E. Prieto, J. de la Figuera, and R. Miranda, Phys. Rev. B **62**, 2126 (2000), URL http://link.aps.org/doi/10.1103/PhysRevB.62.2126. 7.2

[22] C. Busse, C. Polop, M. Müller, K. Albe, U. Linke, and T. Michely, Phys. Rev. Lett. **91**, 056103 (2003), URL http://link.aps.org/doi/10.1103/PhysRevLett.91.056103. 7.2

[23] M. Hupalo (2013), unpublished. 7.2, 7.5

[24] M. Hupalo, E. H. Conrad, and M. C. Tringides, Phys. Rev. B **80**, 041401 (2009), URL http://link.aps.org/doi/10.1103/PhysRevB.80.041401. 7.3

[25] H. Bonzel, D. Yu, and M. Scheffler, Applied Physics A **87**, 391 (2007), ISSN 1432-0630, URL http://dx.doi.org/10.1007/s00339-007-3951-7. 7.5

[26] G. Rosenfeld, R. Servaty, C. Teichert, B. Poelsema, and G. Comsa, Phys. Rev. Lett. **71**, 895 (1993), URL http://link.aps.org/doi/10.1103/PhysRevLett.71.895. 7.5

[27] S. Ovesson, A. Bogicevic, and B. I. Lundqvist, Phys. Rev. Lett. **83**, 2608 (1999), URL http://link.aps.org/doi/10.1103/PhysRevLett.83.2608. 7.5

[28] N. N. Negulyaev, V. S. Stepanyuk, P. Bruno, L. Diekhöner, P. Wahl, and K. Kern, Phys. Rev. B **77**, 125437 (2008), URL http://link.aps.org/doi/10.1103/PhysRevB.77.125437. 7.5

[29] D. McDougall, H. Hattab, M. Hershberger, M. Hupalo, M. H. von Hoegen, P. Thiel, and M. Tringides, Carbon **108**, 283 (2016), ISSN 0008-6223, URL http://www.sciencedirect.com/science/article/pii/S0008622316305383. 7.6

[30] D. Errandonea, R. Boehler, S. Japel, M. Mezouar, and L. R. Benedetti, Phys. Rev. B **73**, 092106 (2006), URL http://link.aps.org/doi/10.1103/PhysRevB.73.092106. 7.7

[31] H. Cynn, C. S. Yoo, B. Baer, V. Iota-Herbei, A. K. McMahan, M. Nicol, and S. Carlson, Phys. Rev. Lett. **86**, 4552 (2001), URL http://link.aps.org/doi/10.1103/PhysRevLett.86.4552. 7.7

[32] B. van de Waal, G. Torchet, and M.-F. de Feraudy, Chemical Physics Letters **331**, 57 (2000), ISSN 0009-2614, URL http://www.sciencedirect.com/science/article/pii/S0009261400010502. 7.7

[33] D. Errandonea, Journal of Physics and Chemistry of Solids **67**, 2017 (2006), ISSN 0022-3697, URL http://www.sciencedirect.com/science/article/pii/S0022369706002903. 7.7

[34] K. T. Chan, J. B. Neaton, and M. L. Cohen, Phys. Rev. B **77**, 235430 (2008), URL http://link.aps.org/doi/10.1103/PhysRevB.77.235430. 7.7

[35] J. Evans, P. Thiel, and M. Bartelt, Surface Science Reports **61**, 1 (2006), ISSN 0167-5729, URL http://www.sciencedirect.com/science/article/pii/S0167572906000021. 7.8

CHAPTER 8. CONCLUSIONS

Our world is becoming interconnected through electronics. Everything from toasters to cars to entire cities are set to be part of the Internet of Things in the coming decade. This is in part made possible by the steady advance of Moore's Law allowing the miniaturization of computer chips. At the heart of the advances required for miniaturization is the understanding of the fundamental processes at surfaces: nucleation and diffusion.

The first focus of this thesis was the non-classical nucleation and diffusion observed in the Pb/Si(111)-7x7 system. There have been decades of previous research on the amorphous wetting layer and the islands in this system, but this thesis is first first study of the transition from wetting layer growth to island growth. Our experiment revealed a novel type of nucleation that was not expected classically. The islands formed at a critical coverage with size distributions that deviated from classical predictions. Individual islands had strong preferences to grow in particular directions with large anisotropies in the number of atoms joining the island from particular sides and correlations in growth direction for neighboring islands. The size of the islands did not scale with their Voronoi area, in part due to the islands also collecting material from the amorphous wetting layer. Multiple generations of islands could form when island density is classically expected to reach a steady state with the mass balance requiring material to be transported collectively (i.e. not as a stochastic random walk). These results continue the trend of unexpected results from the Pb/Si(111)-7x7 system.

The second focus of this thesis was the graphene grown epitaxially on SiC(0001) system. This has particular promise for future graphene use in industry due to SiC being a familiar semiconductor. However, the phase diagram and the locations of atoms at the interface between the SiC substrate and the carbon rich overlayers that can develop into graphene are still debated. With SPALEED we studied the diffraction pattern at various surface conditions.

We noted that there are moiré spots critical to understanding the status of the buffer layer, and observed a mysterious broad background that is not related to long range features on the surface. We propose this broad background might be related to 2D electron confinement. Metal depositions on top of graphene showed thin film Dy crystal structure deviated from the expected bulk structure, with the next step to characterize how this crystal structure change affects magnetic phases. The buffer layer research has laid the groundwork for understanding the initial graphene/SiC surface and the metal deposition experiments have looked at the metal-graphene interaction so current and future group studies of intercalation can be properly analyzed.

Although the particular results of this thesis may not be used by industry to design a product for market for years, the Department of Energy funding for this project provides an expansion of the scientific knowledge base for atomistic processes at surfaces, which is a critical step for future technology development to be streamlined towards an end product goal. In the past 50 years there have been great strides in miniaturizing electronics, but we are still not yet at the bottom. The hope and goal of this thesis is to make a small contribution allowing continued circuit miniaturization.